THÈSE

Pour obtenir le grade de

DOCTEUR DE L'UNIVERSITÉ GRENOBLE ALPES

Spécialité : MBS - Modèles, méthodes et algorithmes en biologie, santé et environnement

Arrêté ministériel : 25 mai 2016

Présentée par

Elaheh ELYASI

Thèse dirigée par **Yohan PAYAN**, Université Grenoble Alpes
et codirigée par **Antoine PERRIER**, APHP

préparée au sein du **Laboratoire Techniques de L'Ingénierie Médicale et de la Complexité - Informatique, Mathématiques et Applications.**
dans **l'École Doctorale Ingénierie pour la Santé la Cognition et l'Environnement**

Modélisation biomécanique du genou pour la chirurgie assistée par ordinateur

Biomechanical modeling of the knee joint for computer assisted medical interventions

Thèse soutenue publiquement le **12 avril 2021**,
devant le jury composé de :

Monsieur Yohan PAYAN
DIRECTEUR DE RECHERCHE, CNRS Délégation ALPES, Directeur de thèse
Monsieur William R. TAYLOR
PROFESSEUR, Institute for Biomechanics, ETH Zurich, Rapporteur
Monsieur Yoann LAFON
MAITRE DE CONFERENCE, Claude Bernard University Lyon 1, Rapporteur
Monsieur Ian STAVNESS
PROFESSEUR ASSOCIE, University of Saskatchewan, Department of Computer Science, Examinateur
Madame Jocelyne TROCCAZ
DIRECTEUR DE RECHERCHE, CNRS Délégation Alpes, Examinatrice

Dedicated to my beloved Taha, and to my mother Mahnaz

who is the strongest woman I know.

Summary

Biomechanical models of the lower limb are generated with various objectives such as investigating joint mechanics, understanding different pathologies, and assisting surgical interventions. Musculoskeletal (MS) models with multibody approaches provide the opportunity to use the kinematic and kinetic data obtained from a subject during an activity to estimate muscle forces and joint contact forces. However, such models are not sufficient to directly investigate the local mechanics of the joint. In this context, Finite Element (FE) models are used to help with the estimation of local joint mechanics and tissue response.

The combination of FE and MS models can be used to go from kinematic and kinetic data of a subject during an activity all the way to the tissue response. Progress in this sense has been made through multiscale modelling workflows where MS models are usually generated in one platform and then the corresponding results are exported to a FE modelling package. However, such a process could be challenging, restrictive, and face compatibility issues. Thus, generating a model that combines the multibody and FE techniques in the same platform could act as the required foundation to open new perspectives for inverse and forward simulations.

Hence, the first goal of this thesis was to use the Artisynth open-source modelling platform to build combined FE-multibody models of the lower limb and to demonstrate various modelling

possibilities. The objective of this thesis is not limited to model generation indeed. The purpose is to use the generated models for applications that can lead to contributions in medical or biomechanical fields. Therefore, we focused on the complications of the high tibial osteotomy (HTO) that is an orthopedic surgery performed on patients with a lower limb deformity. The generated models were used to broaden our understanding of open-wedge HTO complications and to enhance the design of the numerical simulations used for assisting such surgery. Followed by that, we used the combined model for a simulation of gait and attempted to test the consistency of joint modelling between inverse multibody MS models and forward-based models in presence of deformable FE components.

To cover the various objectives envisioned for this project, the manuscript is structured in six main parts. The first part is an introduction to the topic from biomechanical and medical perspectives. In the second part, a systematic review of the literature was conducted on surgical complications of open-wedge HTO to find the areas where we can contribute to the medical and biomechanical studies on the topic.

In the third part, a complete dataset of a healthy subject was created gathering information such as joint, muscle, articular, and connective tissue geometries. In addition, the dataset contained gait analysis and imaging data of the subject that can be used for running or assessing various simulations. This dataset can be used for the generation of models with various complexity levels ranging from MS models with muscle-tendon (MT) parts to FE models of the muscles and the joints.

In the fourth part, a passive deep knee simulation was designed to demonstrate and evaluate various modelling possibilities. A sensitivity analysis was performed on the MT parameters and

the use of FE muscle models versus MT parts was investigated for the quadriceps muscle group. The simulation results were compared against the MRI data collected from our subject at various flexion angles.

In the fifth part, models were designed to study the complications of open-wedge HTO to answer two questions. The first question concerned the tibiofemoral joint and addressed the role of the medial collateral ligament in the models used to predict contact force and stress distribution in the tibiofemoral joint after wedge opening. The second question concerned the consequences of wedge opening on the patellofemoral joint to see if the position of the patella is impacted.

In the last part, we have stepped further through a collaborative work towards the application of our combined FE-multibody model with MT parts for gait simulation. This part presents a developing work that is being conducted to evaluate the consistency of joint modelling in the inverse multibody MS models with the forward-based models having deformable joints.

Acknowledgments

Throughout the writing of this dissertation, I have received a great deal of support and assistance. This research has been financially supported by the *Fondation pour la Recherche Médicale* as part of the FRM DIC20161236448 project.

First and foremost, I would like to express my sincere gratitude to my supervisor Dr. Yohan Payan and my co-supervisor Dr. Antoine Perrier, for their continuous support, patience, motivation, and immense knowledge. This research would have not been possible without their insightful feedback.

Beside my supervisors, incredibly special gratitude goes to. Prof. Dr. William Taylor and Dr. Yoann Lafon for devoting their time to review my dissertation and encouraging me to bring my work to a higher level. My appreciation also goes to the rest of my thesis committee, Dr. Ian Stavness and Dr. Jocelyne Troccaz for kindly accepting the responsibility to examine my doctoral research.

I would like to extend my gratitude to the invited members of my thesis committee Dr. Raphaël Dumas and Dr. Pierre-Yves ROHAN. I had the opportunity to collaborate with Dr. Raphaël Dumas during the final year of my PhD journey and benefit from his deep knowledge, prompt inspirations

and scientific assistance to broaden the scope of my research. Indeed, a great thank you to Dr. Pierre-Yves ROHAN and Dr. Jacque OHAYON who followed my research throughout these years and provided their thoughtful suggestions.

I owe a deep sense of gratitude to Dr. John Lloyd and Prof. Sidney Fels who kindly welcomed me during my two months' research visit at the Department of Electrical and Computer Engineering of the University of British Columbia. I am especially grateful to Dr. John Lloyd for his undoubted effort and valuable scientific and technical assistance, and for dedicating many hours to support me while using the ArtiSynth platform.

These acknowledgments would not be complete without mentioning my colleagues Marie-Line Pissonnier, Mathieu Bailet, and Guillaume Cavalie, for their assistance and all my other colleagues at the TIMC-IMAG laboratory. It was a great pleasure working with them all and I appreciate their help throughout my academic journey.

My deepest appreciation belongs to my family, especially my parents and sister for their support, patience, and understanding for these years that I spent apart from them, without which I would not have been able to start this doctorate.

Last but not least, a very special thanks to my husband Taha, who kindly helped me through my ups and downs with his sympathetic ear and kept me motivated every day even when the Covid-19 pandemic made life challenging for all of us.

Table of contents

List of figures

List of tables

1

Introduction

The lower extremity consists of some of the most complex joints and largest muscles of the body. These joints and muscles have the responsibility of supporting much of the human weight and handle an extraordinary variety of movements such as walking, climbing, and running while keeping our body stable. These movements are produced through a combination of muscle forces that are optimally chosen by the central nervous system to rotate the joints and interact with the environment while keeping our balance. It is still a challenge to understand how each of these movements is produced and make a precise prediction of the muscle forces and joint forces as well as soft tissue deformations during an activity. Meanwhile, various scientific fields such as medicine, sport, and safety are interested in this response. Musculoskeletal (MS) simulations using tools such as multibody and Finite Element (FE) modelling aim to find these answers. Given that the joints in the lower extremity are very prone to injury, and with the existence of many MS or joint disorders in the lower limb, the use of MS simulations seems very promising in personalized

healthcare in the near future for prevention and treatment programs. However, there are still many challenges to overcome.

1.1 Musculoskeletal models

MS models provide the means to use the kinematic and kinetic data obtained from a subject during an activity to estimate muscle forces and joint contact forces. These models use a mathematical description of joints and bones with a representation of muscle anatomy and physiology that can be as simple as a 2D muscle-tendon actuator or as complex as a 3D FE muscle model with active properties.

The body segments are normally represented by rigid bodies that hold each segment's information such as their mass, inertia, and dimensions. The connection between joints is modeled either using mechanical joints having multiple degrees of freedom or through modelling the full contact between bone surfaces or articular surfaces while restricting their relative motion with connective tissues (such as ligaments that can be a 2D or 3D representation based on the modelling technique and objective). Muscle-tendon units are attached to a minimum of two bones as they need to cross at least one joint.

In the simplest case, while using 2D muscle-tendon units, the line of action of each unit is formed by connecting its two bone attachment points. For some muscles, the line of action can be represented more realistically when passing through via-points or being able to wrap around surfaces. In cases where the attachment site of a muscle is large, its mechanical effect is produced through defining multiple muscle-tendon units. The line of action defined for each muscle along with the geometry of the joint it is crossing will define its effective moment arm around that joint.

MS simulations can be generated taking multibody or FE modelling approaches. Each of these modelling techniques indeed has strengths and limitations and is used based on the application desired for the simulation.

MS modelling with multibody technique is very commonly used for solving inverse dynamics and muscle recruitment problems with a low computational cost [1,2]. In these cases, the position and orientation of body segments, which are usually measured with motion capture systems, are used along with the data obtained from force platforms to compute the joint moments required to reproduce the measured movement with the model [2]. Since multiple muscles cross each of the joints, the muscular redundancy problem gets solved using different optimization methods to predict the individual muscle-tendon forces that have produced this net moment in each joint [3–6]. Multibody MS models have been used over the past decades for a variety of activities such as walking, jumping, and cycling [7–10]. Several modelling software packages have also been released over the more recent years such as SIMM [11], AnyBody Modeling System™ [12], and OpenSim [13] that have offered validated MS models to be widely used for different applications including studying musculoskeletal disorders [14–16] or orthopedic surgeries [17–20].

However, the multibody approach is not sufficient to directly investigate the mechanics of the joint at the tissue level. In this context, **Finite Element (FE) models** are used to help with the estimation of local joint mechanics and tissue response. Over the past years, the FE method has been used for developing complex and detailed knee joint models for a variety of applications at the joint level such as orthopedics, injury, and predicting tissue responses [21–27]. More realistic and complex material models have also been developed and tested for the articular and connective tissues using the FE method [28–35]. Meanwhile, the number of studies that have used the FE

modelling technique for musculoskeletal simulations are limited potentially because of the high computational cost and time-consuming model preparation process.

MS modelling using the FE method has the possibility to represent the muscles with 3D FE components. This can be of interest in particular applications such as injury mechanisms or when stress/strain distribution in the muscle is of interest [36–38]. Using the 3D representation of the muscles provides the opportunity to model them in interaction with an environment of other muscles, connective tissue, and bones and not as isolated units that only transmit axial forces to bones via tendons. The surrounding tissues in the muscle's environment can transfer transversal forces to the muscle tissue. These transversal forces have been shown to result in decreasing muscle force production [39]. Given that the lower limb consists of some of the largest skeletal muscles of the body, the aforementioned effect could be important in its muscular architecture. Meanwhile, the high computational cost of MS FE models with 3D muscles is still a major barrier for using them for further applications and especially for dynamic simulations.

In the meantime, the use of the FE modelling technique for MS systems that include detailed deformable models of the joint but represent muscles with 2D muscle-tendon units has been explored [40–42]. The development of these models is motivated firstly because they can predict local tissue loading that is required in pathological cases such as studies on osteoarthritis or ligament injury. The second motivation is that the inclusion of joint-level deformability was found to be substantially impacting muscle parameters (such as their moment arm and length) and thus the estimation of muscle forces [43]. As a result, attempts were made to use concurrent simulations that estimate muscle forces with joint level FE models having subject-specific tissues in a single platform [44–46]. However, the computational cost is significantly increased in these models due to optimization-based strategies; thus, the joint model needs to have limited complexity. To

overcome this issue, conventional proportional-integral-derivative (PID) controllers are being used very recently. Such controllers minimize the error between a kinematic measure in the model and a target profile, to tune the model input (for instance the muscle force) proportional to the measured error parameters [41,47]. This strategy is an alternative to the optimization-based approaches when using deformable detailed joint models to avoid the even higher computational cost in the FE models. However, it is not widely used yet and requires a complete change of modelling strategy from what is conventionally used for estimating muscle forces.

1.2 Combined FE-Multibody models

Another methodology used for going from kinematic and kinetic data of a subject during an activity all the way to the tissue response is the combination of FE and multibody approaches. As previously mentioned, this is needed specifically for answering clinical questions related to osteoarthritis, joint replacement, osteotomy, ligament reconstruction, and so on. Such a combination is indeed required for the simultaneous examination of muscle forces and tissue behavior during movement.

The *state-of-the-art* multiscale modelling workflows use multibody and FE approaches in series. In these workflows, the MS models are generated in a multibody modelling platform and are used to solve the inverse dynamics followed by muscle recruitment problems (with or without electromyography (EMG) assistance). The advantage is that this can be done more rapidly with simplified muscle and joint representations. Then the corresponding results are exported to a FE modelling package and are applied as boundary conditions of a model at the organ or joint level to compute tissue deformation. Such a sequential approach has been used in several applications ranging from bone adaptation [48] and knee implant contact mechanics [49] to the prediction of

ligament and contact forces in the native knee [50] or various other studies with clinical and technical evaluating aims [51–54].

However, there are some challenges and limitations in such a sequential process. First, a sequential workflow works as a one-way where the tissue deformation and parameters of the joint level FE model cannot influence the computation performed to estimate the muscle forces. This means that the contribution of the tissue deformation on muscle forces has been assumed to be negligible. However, the inclusion of joint-level deformability has been shown to substantially impact the estimation of muscle forces [43]. As mentioned in the previous section, the generation of MS models in FE platforms has been used to solve this issue, but they have the drawback of higher computational cost not only for solving the model itself but also for solving the muscle recruitment problem. Thus, the ultimate goal would be to solve this issue without shifting to a fully FE modelling platform and facing its corresponding limitations.

Secondly, the joint models used for the multibody step of the sequential approaches are normally very simplified joints (such as the use of a hinge mechanism for the knee) that are inconsistent with the FE deformable joint models in presence of connective tissues and contact in the articulation [55]. The impact of this inconsistency can be avoided by using quasi-static FE simulations where the primary kinematics of the joint are prescribed to the model while seeking the secondary kinematics [53]. However, the influence of this inconsistency is still unknown on a forward dynamic simulation where the primary kinematics is not imposed. Furthermore, it is not clear if using more advanced knee mechanisms in the MS models of sequential workflows will help with acquiring better results with the forward simulation.

In light of this information, the combination of multibody and FE modelling techniques in a single platform seems to be a good solution to the aforementioned challenges of MS modelling. In

this sense, having a modular combined model where it is possible to use 3D FE muscles or 2D muscle-tendon units and deformable or simplified joint models all in the same platform would be able to open new perspectives in the world of MS modelling. One of our aims in the current study is to move towards this type of model. In the upcoming section, a short introduction to the Artisynth modelling platform is therefore provided. This platform has indeed the potential to provide such possibilities in MS modelling.

1.3 Modelling platform

ArtiSynth is an-open source 3D modelling platform that allows combining the FE method with multibody modelling techniques while supporting contact and constraints. It is mostly targeted at biomechanical and biomedical applications [56] (www.artisynth.org). The platform is Java-based and with a variety of implemented modelling components such as rigid bodies, finite elements having linear or nonlinear materials, muscle-tendon units, and bilateral and unilateral constraints including contact and various joints. Furthermore, it offers the possibility to define 3D FE muscles with active properties or multipoint muscles (passing through via-points) and new methodologies to enable wrapping around arbitrary surfaces [57] or embedded meshes [58]. Meanwhile, it is important to mention that this developing platform has not been specifically designed for gait simulation. Therefore, building such simulations would require some groundwork for instance at the level of segment frame definition and kinematic extraction, muscle-tendon models, or muscle moment arm computation.

The Artisynth modelling system paves the road for the generation of a combined FE-multibody model of the lower limb in a single platform without compromising on the model design at any of the muscular or joint levels. Therefore, the first objective of this study is formed. Explicitly, our first aim is to form a dataset and to generate a modular model of the lower limb where different

components such as joints or muscles can be represented by more complex versions such as 3D FE muscles and deformable joints or by 2D muscle-tendon (MT) parts and simplified joint models. The interchangeable components can be chosen based on the application. As a result, the second objective of this manuscript is to test these models in medical and biomechanical applications. To do so, we use the generated models to study the complications of the high tibial osteotomy (HTO) that is an orthopedic surgery performed on patients with a lower limb deformity. The following sections provide an introduction to this HTO application.

1.4 Application to high tibial osteotomy

The presence of severe deformity in the lower limb can raise problems such as pain, dysfunction, and even disability. Among the possible deformations of the long bones of the lower limb (consisting of tibia and femur), there is the deformity of the tibia in the frontal plane that results in deviating the mechanical tibiofemoral axis of the lower limb from its normal situation. This type of deformation presents itself in the form of varus and valgus angular deformity in the limb as demonstrated in Figure 1-1, which is adapted from Paley [59].

Various surgical procedures have been developed to correct this deformity, relieve the pain, and prevent secondary osteoarthritis such as open or closed wedge high tibial osteotomy with different techniques [60–64]. The ultimate objective of these interventions is to restore the lower limb alignment since this deformity can result in putting excessive pressure on one of the tibiofemoral compartments and cause osteoarthritis damaging that compartment. Performing this surgery can shift weight off of the damaged side of the knee and stop or inhibit the progression of osteoarthritis that could result in requiring a total knee arthroplasty [65]. Moreover, this surgery saves the joint’s original cartilaginous surfaces and corrects the fundamental mechanical problem of the knee. It is therefore best indicated for young and active people [66].

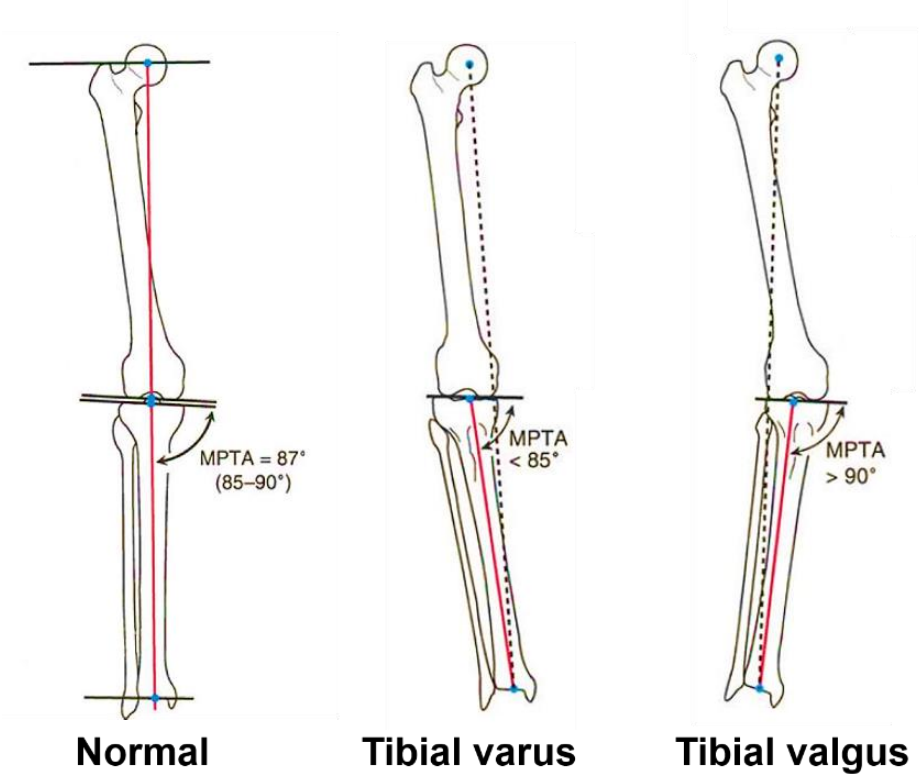

Figure 1-1, Demonstration of the lower limb mechanical axis (right leg) in a normal situation (red line in the left image) and in presence of tibial varus or valgus (dotted line in the right images). MPTA is the medial proximal tibial angle whose range is indicated [59].

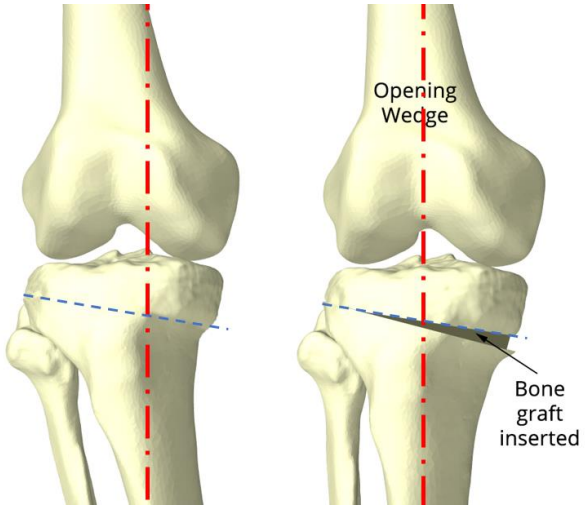

Figure 1-2, OWHTO to correct varus knee malalignment.

This manuscript is particularly interested in a technique called **medial open-wedge high tibial osteotomy (OWHTO)** that involves an oblique osteotomy from the medial side starting just above the level of the tibial tubercle as depicted in Figure 1-2. The survival rate of OWHTO is reported to be between 88.9 and 97 % at 5 years [67–69] and 74–89 % at 10 years [68,70]. However, the success rate seems to be strongly affected by the quality of the correction. The surgery suffers from complications such as alteration in the height of the patella, donor site morbidity (if an autograft is used), loss of correction due to unstable fixation, Medial Collateral Ligament (MCL) tightness, and increased posterior tibial slope while also being associated with high nonunion rates and delayed consolidation [61,62], [71].

Among the aforementioned consequences and complications, some of them are particularly interesting for the current study. These complications are patellar descent, MCL tightness, and increased posterior tibial slope. We have made the assumption that these complications are related to either planning or execution of the surgical plans and in some cases could have been avoided by a better choice of the opening wedge angles or benefitting from more recent techniques and methods such as the use of biplanar osteotomy, computer-aided approach or patient-specific guides [72–76]. Additionally, two of these complications (MCL tightness and patellar descent) can be correlated to the soft tissues surrounding the joint. The most proper way to justify this conclusion is by taking a look at the anatomy of the knee joint in terms of the muscles and ligaments inserted in the proximal part of the tibia (Figure 1-3) and their insertion sites relative to the OWHTO cut as depicted in (Figure 1-4).

As demonstrated in Figure 1-4, the patellar tendon is inserted underneath the osteotomy cut. Knowing that the patellar tendon is attached to the patella and that the patella itself is attached to four muscles being the Rectus Femoris, the Vastus Medialis, Vastus Lateralis, and Vastus

Intermedius (Figure 1-3), it is clear that all these four muscles are also affected by the HTO wedge opening and could be causing the patellar descent. Similarly, for the superficial layer of the MCL if we consider it to be attached underneath the HTO cut, then opening a wedge might result in excessive tension in it.

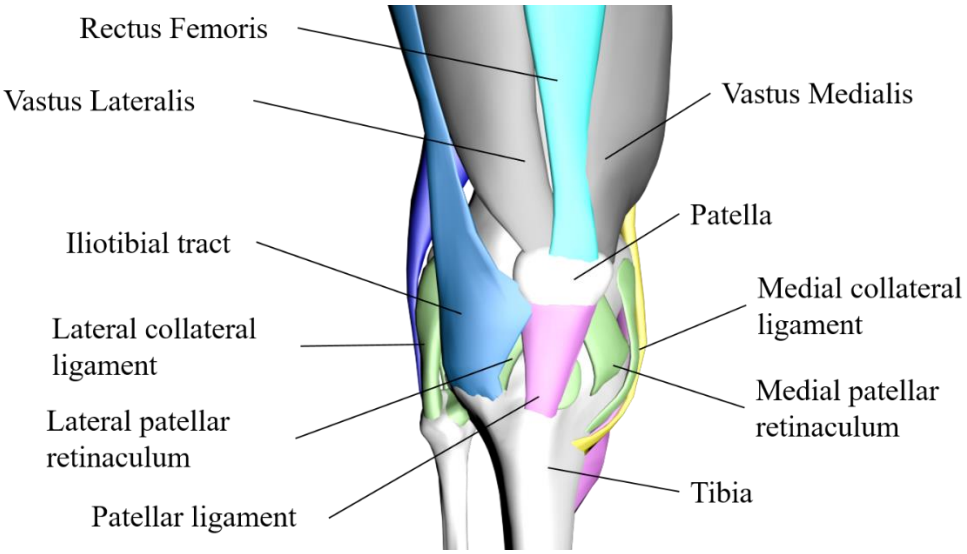

Figure 1-3, A frontal view of the knee joint in presence of selected muscles and ligaments.

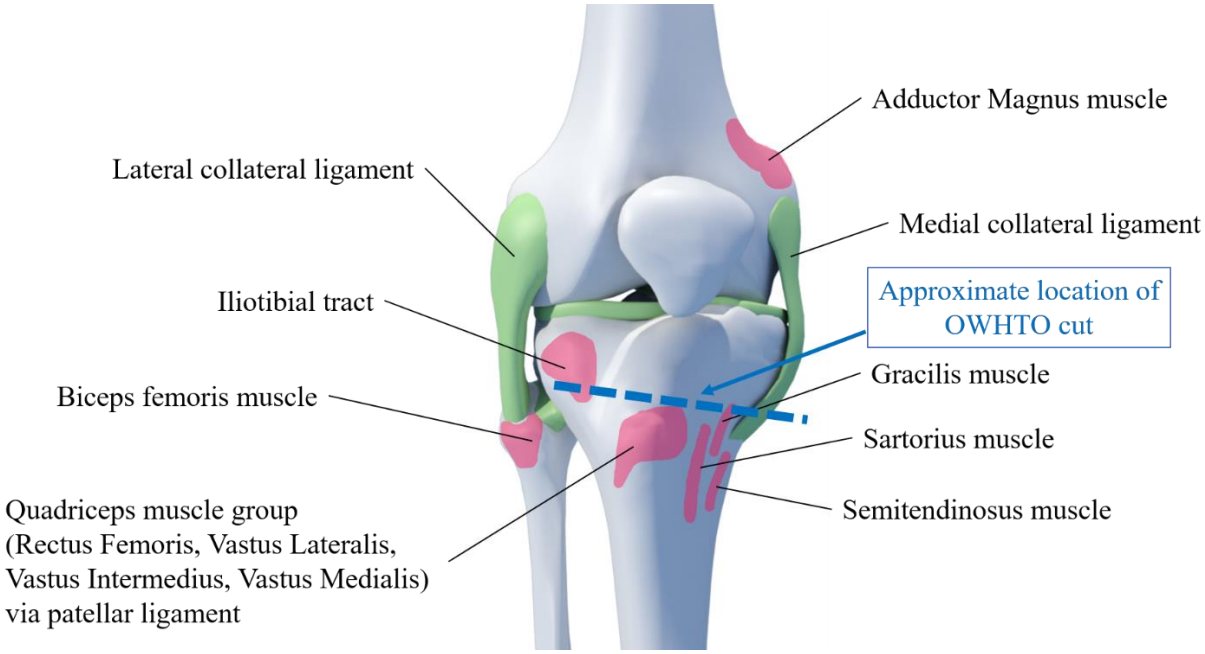

Figure 1-4, The anatomical insertion sites of the muscles around the knee.

In this sense, the capabilities of biomechanical simulations in problem isolation and parametric studies can be beneficial to better understand these complications and to recreate them in numerical models that could be used to assist surgical planning in the future. Of course, the validity of our assumptions requires to be evaluated by taking a closer look at the medical literature. As a result, a systematic review was conducted on the topic and is presented in the next chapter that will help us to spot the parts where biomechanical simulations can contribute.

1.5 Aim and outline of the thesis

The first goal of this thesis is to use the Artisynth open-source modelling platform to build a modular combined FE-multibody model of the lower limb in order to demonstrate and test various modelling possibilities on a subject. At a second step, the model is applied to OWHTO surgery with the aim to broaden our understanding of its complications in a way that results in both clinical and biomechanical contributions. Subsequently, we used the generated FE-multibody model for a simulation of gait and made an attempt to test the consistency of joint modelling between inverse multibody MS models and forward-based deformable models. The manuscript is designed as follows:

Chapter 2 will present a systematic review of the medical and biomechanical literature that is conducted on specific surgical complications of HTO. In this chapter, a brighter view of the common planning steps of HTO surgery is first provided. Secondly, the complications of the surgery are analyzed from the clinical literature to evaluate their validity and importance, which helps to find the medical questions that we can focus on. Finally, the biomechanical studies on HTO related to the principles or complications of the surgery are discussed to find the areas where we can contribute to the design of biomechanical studies.

In **Chapter 3**, a complete dataset of a healthy subject is created that contains joint, muscle, articular and connective tissue geometries. Additionally, specifications of the gait analysis performed on the subject are provided that will be used in the following chapters for a simulation of human gait. Furthermore, imaging data at different flexion angles has been collected and is reported here that can be used for evaluating a passive flexion simulation. The component geometries obtained from various images are superimposed to share the same coordinate frame. As a result, this can be used for the generation of models with various complexity levels ranging from MS models with muscle-tendon (MT) parts to FE models of the muscles and the joint with the components being interchangeable.

In **Chapter 4**, a passive deep knee simulation using the MRI sets at different knee flexion angles has been designed. This simulation is first motivated to demonstrate and to compare various modelling possibilities that can be provided thanks to the generated dataset of chapter 3. The second aim is to use the MRI data at different flexion angles to evaluate the models with various levels of complexity before taking the models into practice for application-based studies in the upcoming chapters. Thus, the passive deep flexion simulation is used to perform a sensitivity analysis on the estimated muscle-tendon parameters of the quadriceps muscle group and the results are compared with a simulation in presence of 3D FE muscle models. In addition, a mesh embedding technique is used on the 3D FE muscle components to get tested as a potential method to reduce the computational cost of the FE model.

Chapter 5 is dedicated to studying the complications of HTO. In this chapter, we plan to answer two main questions. The first one is related to the tibiofemoral joint. A detailed FE model of the tibiofemoral joint was generated to analyze if accounting for the tightness or release of superficial MCL after wedge opening can noticeably impact the contact force and stress distribution at a time

frame during level walking. The second question concerns the consequence of the surgery on the patellofemoral joint. For this, the MS model with 3D FE muscles that was evaluated in chapter 4 is used as a base. The objective is to see if such a surgery can impact the position of the patella and the passive force of the quadriceps muscles group.

Subsequently, in **Chapter 6**, collaborative work is conducted to use the generated combined FE-multibody model with MT parts for a simulation of gait. This is an initial step of a developing study to evaluate the consistency of joint modelling in the inverse multibody MS models with the forward-based models with deformable and detailed joints. For this, the model of our subject was exported to another platform and turned into a multibody model to solve the muscle recruitment problem. Then, the corresponding results are imported to the combined model in Artisynth and are used to run a forward combined FE-multibody simulation.

Finally, **Chapter 7** presents a general conclusion on the contributions made by the models generated in this Ph.D. thesis.

2

A systematic review on the complications of open-wedge high tibial osteotomy from clinical and biomechanical perspectives

Open-Wedge High Tibial Osteotomy (OWHTO) plays a significant role in the conservative treatment of medial knee osteoarthritis in young and active patients with a varus deformity [77–79]. The purpose of this surgery is to transfer the excessive axial loads applied on the medial compartment of the knee to the lateral compartment. This can be achieved by performing an oblique osteotomy on the medial side of the proximal tibia that results in moving the mechanical axis of the lower limb to pass through the lateral tibiofemoral compartment rather than the medial compartment [80,81].

The main difficulty of this surgery is to find the correct modification of limb alignment that significantly reduces the pressure and contact area of the medial compartment without increasing these values in the lateral compartment or creating laxity. The amount of the required correction is traditionally defined based on the position where the Weight-bearing Axis (WBA) crosses the tibial plateau. The correction amount is considered to be in the recommended zone if the WBA

passes through 65%-70% of the tibial width measured from the medial side although this range has been recently modified to be from 62% to 66% [82,83]. Another general suggestion regarding the correction amount that is widely applied is a valgus overcorrection between 3° and 6° on frontal projected X-ray [84].

However, the aforementioned protocols do not seem to be the optimum solution for all the patients because the success rates of HTO are not consistent with the long-term survival rates. *D'Entremont et al*. performed a study using a Magnetic Resonance Imaging (MRI) based method on opening-wedge HTO and found that this surgery changes both tibiofemoral and patellofemoral kinematics in a manner that cannot be assessed using conventional radiology [85]. Various studies have reported a deterioration in the outcomes of HTO after longer follow-ups [86,87]. These sub-optimal outcomes can definitely be connected to inaccurate choices of correction angle by looking at the follow-up studies. For instance, it has been shown that after a 10 to 13-year follow-up of 93 HTOs, 68 were under-corrected and five were overcorrected [81]. The unsolved question of re-alignment has resulted in performing multiple studies taking various approaches including clinical studies [88,89] and clinical or cadaveric biomechanical studies [90,91]. However, there is still a high lack of consensus on the ideal alignment after HTO and some study results even seem to be contradictory.

From a biomechanical perspective, the exact size and shape of the wedge opened on the tibia during the osteotomy process defines the amount of alteration made on the lower limb alignment in both the sagittal and the coronal views. Considering the fact that this surgery is mostly performed on patients with a varus deformity, the highest alteration is indeed present in the coronal plane. This is why the traditional planning methods define the required correction angle based on

the coronal view [82,83,92]. However, not considering the changes in the sagittal plane during the planning step can lead to complications such as alteration of the Posterior Tibial Slope (PTS) [93].

In addition to that, the geometry of the opened wedge can be directly related to the change of tension inside the soft tissues whose insertion site has been altered during HTO. This is also the case for the alteration in the position of the patella. The symptoms of such an effect can be seen in reported complications of OWHTO such as MCL tightness [94] and patellar height decrease. While the aforementioned complications can be foreseen from a biomechanical point of view, their validity may be still a place of debate among different clinical and cadaveric studies with contradictory results.

As a result, the objective of the current chapter is to perform a systematic review to take a closer look at the surgical complications of OWHTO and to investigate the validity of the complications that can be correlated with the shape and dimensions of the opened wedge. In this context, the medical literature is considered as a starting point, but at the discussion level, a biomechanical perspective is also added to assist the interpretation of the results. Finally, model-based biomechanical studies targeting the planning of HTO are also addressed to find out their current state and find the areas where we can contribute to the design of biomechanical studies.

2.1 Searching methods

The systematic literature review was performed through PubMed and Science Direct. The related papers to our study theme were approached using three different search categories: (1) searching for studies addressing sub-optimal outcomes and complications of HTO and OWHTO in general. (2) Searching for the key terms related to some particular complications of HTO that were of our interest. The latter included terms such as “posterior slope alteration”, “patellar height”, “patellar tracking”, “patella baja”, “Medial Collateral Ligament (MCL) tightness”,

"superficial MCL release", "tibiofemoral contact pressure" and the variations of these terms. (3) Searching targeted at the musculoskeletal multibody and Finite Element (FE) biomechanical studies conducted in relevance to assisting HTO. Following the initial search steps, the titles of all the search outcomes were monitored and only peer-reviewed studies related to HTO or OWHTO were collected. A language filter has also been used to only include articles written in English. Following the first search step, a second search for relevant articles was performed within the references cited in the selected articles.

The titles and abstracts of the screened articles were analyzed by two review authors (E. Elyasi and G. Cavalie). References were imported into the bibliographic management software and all duplicates were removed. Then, the full texts of the selected articles were read. The last bibliographic search on PubMed was done on November 20, 2019. The search strategy was developed following the different items of the PRESS-2015 (Peer Review of Electronic Research Strategies). Regarding the inclusion and exclusion criteria, all the articles reporting the biomechanical changes induced by OWHTO were included. In addition, articles on the biomechanical modelling of OWHTO using multibody dynamics and FE methods were included. All articles on lateral closing high tibial osteotomies, varus osteotomies, double osteotomies, osteotomies performed to treat knee laxities, plate design, and positioning, and the articles related to other complications of HTO that were not in the interest of the current chapter were excluded.

2.2 Data extraction and quality assessment

The qualitative and quantitative data of the screened articles were extracted. They include the title of the study, the authors, the year of publication, and the design of the study. Then, the main results concerning tibiofemoral pressures according to the MCL status, changes in tibial slope,

changes in patellar height and/or patellar tracking, and biomechanical simulations were categorized in independent tables.

To evaluate the methodological quality of the studies, the validated QUACS scale was used for cadaver studies and the STROBE scale was used for clinical studies. The QUACS scale has 13 items. A score of 1 was given when the item was present and 0 when the item was missing. Therefore, a total score of between 0 and 13 points was obtained. Then, a quality score ranging from 0 to 3 depending on the total score obtained was assigned. The quality score of 0 corresponded to a QUACS score between 0% and 25% of the maximum score. 1 for a QUACS score between 25 and 50% of the maximum score, 2 for a QUACS score between 50 and 75% of the maximum score, and finally 3 for a QUACS score between 75 and 100% of the maximum score. The STROBE scale was treated in the same manner, being composed of 22 items and the quality of the studies was scored in the same way as for the QUACS scale ranging from 0 to 3.

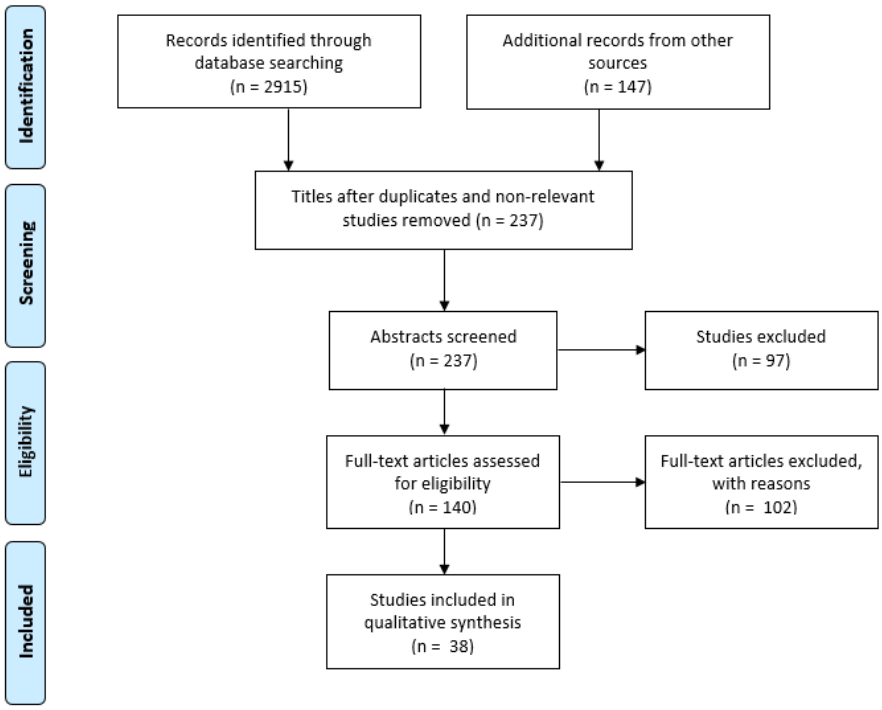

Figure 2-1. PRISMA flow diagram of the search and selection process and the effect of the application of inclusion/exclusion criteria.

2.3 Results

A total of 38 studies met the inclusion criteria for the systematic review. The PRISMA statement flowchart depicted in Figure 2-1 shows the number of search results (a total of 3062 articles) and the number of articles that were included or excluded [95]. The 38 included articles were then divided into the defined categories based on their topics and provided results. The defined categories, as well as the number of articles included in each category, are as follows: MCL release (6 articles), posterior tibial slope (14 articles), patellar position (12 articles), and biomechanical simulations (6 articles) with the possibility of having repeated articles in categories.

2.3.1 MCL release

Six articles studying the effect of MCL release on tibiofemoral contact and valgus laxity (Table 2-1) were included. As presented in the table, the alteration in the contact pressure and contact area in the medial and lateral knee compartments are reported after osteotomy. These results are categorized based on the level of MCL release and the amount of alignment correction during HTO. In addition, the change in valgus laxity has been reported by three studies. The quality of the studies (QUACS or STROBE scores) has also been assessed based on the nature of the study and reported.

2.3.2 Tibial slope

Fourteen articles were included in the tibial slope category and the corresponding results are provided in Table 2-2. The osteotomy techniques used in these studies vary between conventional (monoplanar) osteotomy (with and without navigation) and biplanar osteotomy. In addition to the posterior tibial slope before and after surgery, the difference of this variable is provided to simplify comparisons between studies. The statistically significant results are marked in red (Table 2-2).

*Table 2-1, Modifications of joint pressures, contact areas according to the state of the medial collateral ligament. sMCL: superficial MCL, MJO: Medial Joint Opening, *In red: statistically significant data*

Authors (year)	Study	No. knees	sMCL release state	Correction amount	Medial contact pressure change from intact state	Medial contact area change from intact state (mm2)	Lateral contact pressure change from intact state	Lateral contact area change from intact state (mm2)	Valgus laxity	Comments / highlights	QUACS Scale	STROBE
Pape et al. (2006) [96]	Cadaveric	20	complete release	0°	—	—	—	—	↑ 38% MJO	No HTO performed, the release of sMCL should be kept to a minimum to decrease potential late valgus instability especially in patients with small wedge sizes and preexisting medial laxity	11/13 = 3	—
			anterior bundles release						↑ 39% MJO			
Seo et al. (2016) [97]	Clinical	54	complete release	Fujisawa point	—	—	—	—	↑ 0.2 mm MJO intra-operative	Medial laxity induced by complete sMCL release can be recovered by opening the osteotomy site.	—	18/22 = 3
Van Egmond et al. (2017) [98]	Cadaveric	7	no release	10°	↑ 0.17 *	↑132.9 *	↓ 0.02 *	↓ 47.0	↓ 0.1°	release of sMCL helps reducing medial cartilage pressure but significantly increases valgus laxity. Considerable relaxation of MCL over time.	9/13= 2	—
			complete release		0.0 *	↑ 9.6 *	↑ 0.01 *	↑ 7.7	↑ 7.9°			
Seitz et al. (2018) [94]	Cadaveric	6	no release	5°	↑ 0.11	↑ 9	↓ 0.14	↓ 35	—	For the extended knee, biplanar osteotomy, medial contact pressure decreased most when with 10° correction and releasing MCL	9/13= 2	—
				10°	↑ 0.14	↑ 43	↓ 0.25	↓ 85				
			complete release	0°	↓ 0.03	↓ 79	↓ 0.24	↓ 97				
				5°	↓ 0.05	↓ 63	↓ 0.11	↓ 35				
				10°	↑ 0.01	↓ 125	↓ 0.14	↓ 52				
Agneskirchner et al. (2007) [99]	Cadaveric	6	no release	9 mm	↑ 0.68 *	↑ 78.4	↓ 0.3 *	↓ 91.7	—	Biplanar osteotomy, Under 1000N load passing from 62% valgus position. The effect of loading axes has also been studied for the intact knee. High medial pressure maintains despite shifting the loading axis into valgus, decompression happens only after complete release of MCL distal fibers.	9/13= 2	—
			50% release		↑ 0.24 *	↑ 29.7	↓ 0.24 *	↓ 35.2				
			complete release		↓ 0.04 *	↓ 15.0	↓ 0.08 *	↓ 47.7				
Suero et al. (2015) [100]	Cadaveric	7	complete release	5°	↑ 3% *	↑ 9%	↑ 33%	↑ 11%	—	Under 550 N axial load. We have only reported the percentage of alterations in the contact pressure and contact area. The reason for this was that the reported values were not consistent with the other studies although the units were the same.	11/13 = 3	—
				10°	↓ 23%	↓ 21%	↑ 84%	0%				
				15°	↓ 64%	↓ 46%	↑ 141%	↓ 2%				

*Table 2-2: Modifications of the tibial slope. HKA: standing hip–knee–ankle, OW: Open-Wedge, CW: Closed-Wedge, *In red: statistically significant data*

Authors (year)	Study type	Osteotomy technique		No. knees	Correction amount	PTS pre-HTO	PTS post-HTO	PTS difference	QUACS	STROBE
Martineau et al. (2010) [101]	Cadaveric	OW		6	5 mm	8°	12.1°	↑ 4.1° *	7/13 = 2	
					10 mm		16.3°	↑ 8.3° *		
Ozel et al. (2017) [102]	Clinical	OW		39	Mean HKA 183.7°	8°	15°	↑ 7° *		14/22 = 2
Sterett et al. (2009) [103]	Clinical	OW		82	—	12.5°	16.5°	↑4° *		18/22 = 3
Lee et al. (2014) [104]	Clinical	OW	With navigation	40	Fujisawa point	10.5°	11.5°	↑1°		17/22 = 3
			Without navigation	40		8.7°	8.2°	↓0.5°		
Nerhus et al. (2017) [105]	Clinical	OW (CW studied but not reported here)		70 total	HKA 186°	7°	8°	↑1° *		17/22 = 3
Noyes et al. (2006) [80]	Clinical	OW		55	—	9°	10°	↑1°		15/22 = 2
Elmali et al. (2013) [106]	Clinical	OW	Monoplanar osteotomy	56	HKA 186.4	10.1°	11.7°	↑1.6° *		15/22 = 2
			Biplanar osteotomy	32	HKA 185.4	9.9°	10.7°	↑0.8° *		
Birmingham al. (2009) [107]	Clinical	OW		126	HKA 180°	5.15°	6.37°	↑1.22° *		15/22 = 2
Chang et al. (2017) [108]	Clinical	OW	With navigation	41	WBA passing 64.3%	11.7°	12.2°	↑0.5°		19/22 = 3
			Without navigation	66	WBA passing 57.3%	12.1°	13.1°	↑1°		
Na et al. (2018) [109]	Clinical	OW		71	HKA: 182.6° (varus>4°)	10.6° (varus>4°)	10.9° (varus> 4°)	↑0.3° (varus>4 °)		18/22 = 2
					HKA: 184.2° (varus <4°)	10.0° (varus<4°)	10.7° (varus< 4°)	↑0.7° (varus<4 °)		
Van Egmond et al. (2016) [110]	Cadaveric	OW (CW studied but not reported here)		25 OW	HKA: 184.3° (open)	—	16.2° (open)	↑1.6°	9/13 = 2	
Nha et al. (2016) [111]	Clinical meta-analysis	OW (CW studied but not reported here)		—	—	—	—	↑2° *		
Yan et al. (2016) [112]	Literature review	OW	With navigation	1608	—	navigated HTO produces significantly less change in PTS compared to conventional methods.				
			Without navigation	608						
Wu et al. (2017) [113]	Comprehensive meta-analysis	OW & CW		663 OW 581 CW	—	open-wedge HTO showed greater PTS angle compared to closed-wedge, ↑1.31° *				

2.3.3 Patellar position

Twelve studies were selected for the category of patellar position (Table 2-3). The reported outputs of the selected studies are divided into patellar height, lateral patellar tilt, and patellar shift. Considering that various methods were used to assess the patellar height in the selected studies, five different indices were chosen to compare the alteration in the patellar height after HTO. These indices include Insall-Salvati, modified Insall-Salvati, Caton-Deschamps, Blackburne-Peel, and Modified Blumensaat as defined in the literature [114,115]. The results of the quality assessment of the selected papers (STROBE scores) are also presented in Table 2-3.

2.3.4 Biomechanical simulations

Among the selected articles in the current review, a total of six articles have chosen a biomechanical simulation approach with generic or subject-specific modelling (Table 2-4). These articles were mainly focused on testing the effect of the alignment principle on tibiofemoral contact balancing or estimating the optimum alignment based on subject-specific models. One article had studied the effect of MCL slackness and MCL release on the biomechanical outcomes. The objectives, findings, and various validation methods of these studies are presented in Table 2-4.

2.4 Discussion

2.4.1 MCL release and its correlation with tibiofemoral contact pressure

The MCL is composed of two bundles. The superficial bundle, which is distally attached to the medial aspect of the proximal part of the tibia, and the deep bundle that is attached to the joint capsule. In order to perform OWHTO, the medial proximal part of the tibia needs to be exposed. As a result, to properly expose this region and based on the condition of MCL in each patient, various strategies might be taken by the surgeons with respect to the MCL: preservation, selective

release of the superficial bundle, or a complete release of the superficial bundle. This of course raises concern about the effect of MCL release on valgus stability and also leads to questioning the correct approach to take with respect to MCL and its effect on the tibiofemoral contact pressures. As provided in Table 2-1, various studies show that performing an OWHTO without any release of the MCL results in an increase of the MCL strain, an increase in the contact area and pressures on the medial tibiofemoral compartment, and a decrease in these parameters on the lateral compartment [94,98,99]. This condition which is in contrast with the objective of performing OWHTO can even be deteriorated by increasing the size of the opened wedge. The results of the cadaveric study performed by *Seitz et al*. show that a 5° and 10° wedge opening in the tibia respectively increase the medial contact pressure up to 0.11 and 0.14 MPa with respect to the pressure before surgery [94].

Generally, the release of the superficial bundle results in a decrease in the contact area and pressures on the medial compartment and in an increase in these parameters on the lateral compartment [94,98,99]. For instance, for a 10° opening during osteotomy, there is a significant decrease in the medial tibiofemoral pressure after completely releasing superficial MCL in comparison to the unreleased state [94,98]. This decrease is reported to be 0.13 MPa by *Seitz et al*. [94] and 0.17 MPa by *Van Egmond et al*. [98]. In the same category, *Agneskirchner et al.* reports an average decrease of 0.44 MPa and 0.64 MPa respectively by 50% MCL release and complete MCL release, with respect to unreleased MCL when the mechanical axis passed through the Fujisawa point (62% of the tibial plateau width when measured from the medial side) [99]. Although it is important to bear in mind that the actual goal is to reduce the medial contact pressure and contact surface with respect to the intact knee, which is not achieved by 50% MCL release as the respective 0.24 MPa and 29.7 mm^2 increases in these values imply [99].

*Table 2-3: Patellar position modifications during OWHTO. NS: Not Significant, *In red: statistically significant data, mBP: modified Blackburne-Peel ratio, OW: Open-Wedge, Clin.: clinical study, Mono.: monoplanar, Bi.: Biplanar, Postop.: postoperative.*

Authors (year)	Study type	Osteotomy technique		No. knees	Correction amount	Patellar height					Lateral tilt	Shift (mm)	STROBE
						Insall-Salvati	Modified Insall-Salvati	Caton-Deschamps	Blackburne-Peel	Modified Blumensaat			
Longino et al. (2013) [116]	Clin.	OW	Bi.	29	HKA: 180.8°	—	—	↓0.09*	↓0.10*	—	—	—	19/22 = 3
			Mono.	29	HKA: 179.9°	NS	NS	↓0.19*	↓0.23*	—	—	—	
Hanada et al. (2014) [115]	Clin.	OW (CW not reported here)		10	WBA passing 62.5%	↑0.308 * (Postop.) ↑0.238 (NS) (after 1 year)	—	—	—	↓ 0.094 * (Postop.) ↓0.153 * (after 1 year)	—	—	13/22 = 2
Tanaka et al. (2018) [117]	Clin.	Bi. OW		52	HKA: 181.3°	—	—	↓0.16*	—	—	—	—	14/22 = 2
Park et al. (2017) [114]	Clin.	OW	Bi.	33	HKA: 180.3°	↓0.01	↑0.01	↓0.04*	↓0.03*	—	↓1.40°*	↓0.01	16/22 = 2
			Mono.	30	HKA: 180.8°	↓0.05*	↓0.08*	↓0.10*	↓0.09*		↓2.00°*	↓0.01	
Fan et al. (2012) [118]	Clin.	OW		9	HKA: 183.9°	↑0.07	—	—	↓0.19*	—	—	—	10/22 = 1
Bito et al. (2010) [119]	Clin.	OW		49	—	—	—	—	mBP ↓0.2*	—	↓2.2°*	NS	11/22 = 2
Song et al. (2012) [63]	Clin.	OW (CW not reported)		50	—	—	—	—	↓0.10*	—	↑0.6°	↑0.4	9/22 = 1
Lee et al. (2016) [120]	Clin.	OW		46	HKA: 181.4°	—	—	—	↓0.1*	—	↓1.8°*	NS	11/22 = 2
D'Entremont et al. (2014) [85]	Clin.	OW		14	—	—	—		—	—	↓2.20°*	↑0.9*	17/22 = 3
Birmingham et al. (2009) [121]	Clin.	OW		126	HKA: 180°	NS	—	—	↓0.05*	—	—	—	15/22 = 2
Elmali et al. (2013) [106]	Clin.	OW	Bi.	32	HKA: 185.4°	NS	—	—	NS	—	—	—	15/22 = 2
			Mono.	56	HKA: 186.4°	↓0.07*	—	—	↓0.07*	—	—	—	
Noyes et al. (2006) [80]	Clin.	OW		55	—	—	—	—	↓0.09	—	—	—	15/22 = 2

Table 2-4: PTS: Biomechanical studies on the OWHTO alignment and related surgical complications. Posterior Tibial Slope, CW: Closed-wedge, OW: Open-Wedge

Authors (year)	Simulation technique	Osteotomy technique	Ligament modelling	Loading condition	Objective	Outcomes	Validation method
Zheng at al. (2017) [125]	FE	OW	3D FE	Subject-specific loading data at 5% of the gait cycle obtained from gait analysis	Introducing a subject-specific modelling procedure to see the biomechanical effects of HTO alignment on cartilage stress distribution.	Providing a platform for non-invasive, patient-specific pre-operative planning of the osteotomy	Maximum contact pressure was compared to literature under similar axial loading [122,123]
Trad et al. (2018) [126]	FE	CW	Axial	Axial load in standing position	Effect of varying the HTO correction angle on the stress distribution in two knee compartments. Finding optimal correction angle to achieve a balanced loading between compartments.	Achieving a balanced stress distribution in two compartments and desired alignment under a valgus hypercorrection of 4.5 degrees Study findings agree well with clinical data and recommendations found in the literature [94]	Compared against experimental and numerical results from the literature.
Martay et al. (2017) [127]	FE	OW	Axial	Loading and alignment calculated from motion analysis data at the point of maximum load in the walking cycle	How different WBA re-alignments affected load distribution in the knee, to find the optimal post-surgical re-alignment.	Proposing a new target for WBA correction being 55% tibial width (1.7°–1.9° valgus),	Validated their model creation method using porcine specimens. Compared their HTO related results to a published human cadaveric study [24].
Purevsuren et al. (2019) [128]	Multibody dynamics	OW	Axial	Axial load in standing position	Effects of 1) MCL laxity, 2) loading axis correction, 3) different types of MCL release, on the medial-lateral contact force distribution after OWHTO. Determining the necessary MCL release strategy for balanced load distribution	MCL slackness affected load distribution of knee after HTO. Anterior and middle bundle release shown to be the optimal surgical method to balance contact distribution in simulated standing position. Only anterior bundle release is recommended for knees with a large amount of MCL slackness. No effect observed by changing the simulated axis correction.	Compared estimated medial and lateral contact distribution after HTO with previous cadaveric studies [99,124].
Mootanah et al. (2014) [24]	FE	none	3D FE (Tuned to minimize kinematic difference from cadaver specimen)	Axial load + varus and valgus bending moments (0 to 15 Nm) applied about the knee joint center to simulate different malalignment degrees	Predicting knee joint contact forces and pressures for different degrees of malalignment.	Generated knee model could give an accurate prediction of normalized intra-articular pressure and forces for different loading conditions. The model could be further developed for subject-specific surgical planning.	Cadaveric study performed having matching boundary and loading conditions.
Kuriyama et al. (2019) [129]	Dynamic musculo-skeletal modelling	OW	Axial	gait and squat	Determining the ideal coronal alignment under dynamic conditions	Approved the validity of classical target alignment. Over-correction should be avoided. Increased PTS caused excessive ACL tightness due to femoral posterior positioning with respect to tibia. PTS increase resulted in LCL tightness and PCL	Comparing the kinematics of the native knee model with the in vivo kinematics obtained from a healthy volunteer.

As concerns the lateral compartment, the general idea of increasing the contact pressure and contact surface by further releasing the MCL seems to be relevant in many cases. On the other hand, the results provided by *Seitz et al*. [94] and *Agneskirchner et al*. [99] show that the pressure and area of contact after OWHTO has decreased in the lateral compartment regardless of the MCL release. These results are in contrast with the results of *Van Egmond et al.* and *Suero et al.* who are reporting an increase in these values [98,100].

As previously mentioned, MCL release could have a negative impact of increasing the valgus laxity that could clinically induce a feeling of instability for the patient. Concerning laxity of the knee during valgus stress, there is less consensus on the outcomes. The study performed by *Pape et al*. suggests that releasing the MCL increases the valgus laxity and thus it should be kept to a minimum to decrease the potential of late valgus instability [96]. However, it is worth mentioning that the alignment of the cadaver knees has not been altered in this study and the conclusion has been made without performing any HTOs. This finding is supported by the study of *Van Egmond et al*. that showed a laxity increase of nearly 8° after a complete release of the superficial MCL [98]. On the contrary, the clinical study of *Seo et al*. [97] reveals that the increase of the medial joint opening (MJO) because of complete release of superficial MCL was totally recovered after opening the wedge during medial osteotomy. There was no significant difference between the pre-operative and post-operative MJO values at 3, 6, and 12 months after surgery.

Most authors seem to have a consensus that releasing the superficial bundle of the MCL during OWHTO helps with better achieving the goals of the surgery. Indeed, when no release is performed, the opening of the gap of the osteotomy causes a significant increase in the MCL strain [94] and therefore medial tibiofemoral pressures, whereas, when the release is performed, the medial tibiofemoral pressures drops significantly. From the authors' perspective, in order to

facilitate the process of making a conclusion from the clinical and cadaveric studies, it is very important to decompose the different factors that are playing a role in the MCL tension. Before surgery, the MCL of each patient has a particular pre-existing tension in it; this tension is of course reduced by partially releasing the MCL bundles while performing OWHTO. On the other hand, if we consider that the osteotomy cut is performed superior to the insertion of the superficial MCL, opening the wedge results in re-tensioning the MCL relative to the size of the opened wedge. Consequently, the final tension remaining in the MCL after OWHTO is affected by the amount of release, the size of the opened wedge, and also the pre-existing tension in it before surgery. So, from a biomechanical perspective and with the above assumptions, if the patient has a pre-operative lax MCL and if the surgeon partially detaches the MCL to open a small wedge on the tibia, it is expected that the MCL ends up being lax. It is therefore recommended in that case to avoid MCL release as suggested by *Pape et al*. [96]. On the other end, if the MCL is not lax pre-operatively and if the size of the opened wedge on the tibia is large, the MCL would end up being tight and further MCL release is required to reduce the medial pressure.

2.4.2 Tibial slope modification

The traditional planning methods for OWHTO rely on the coronal view imaging data to define the required correction angle [82,92]. This is while as described by *Noyes et al*., the hinge axis of the wedge that is opened in the tibia is not necessarily perpendicular to the coronal plane which means that the tibial slope in the sagittal plane can be modified during OWHTO [130]. This can cause a change in the kinematics as well as in the stability of the knee. The normal range for the posterior tibial slope is 7° to 10° [131]. An increased posterior tibial slope induces an anterior translation of the tibia with respect to the femur as reported by *Giffin et al*. [132]. Based on our observations, there is a lack of consensus on whether or not an increased posterior slope can

increase the anterior cruciate ligament (ACL) strain and cause a higher risk of rupture and chronic anterior knee laxity. The *in situ* study of *Shelburne et al*. has shown that for a 5° increase in the posterior tibial slope, the ACL strain is increased by 26% [17]. On the other hand, *Giffin et al*. [132] and *Martineau et al*. [101] have not observed a significant change in the cruciate ligament forces or strains under the loading conditions of their cadaveric studies.

There are recommendations in the literature that enable the surgeon to maintain the tibial slope that is in the normal range or to correct it during OWHTO. This includes the use of the 3-triangle method proposed by *Noyes et al*. [130] or the tables provided in the study of Hernigou [81]. In addition, other authors have proposed mathematical formulas to achieve a targeted tibial posterior slope [133] or to avoid changing the posterior tibial slope while performing an osteotomy [134]. Other than the recommendations for the conventional OWHTO, the use of other surgical methods such as the Biplanar osteotomy has been shown to significantly help with the conservation of the tibial slope as reported by *Elmali et al*. [106]. Indeed, the use of patient-specific 3D printed guides can also help in this context to conserve or modify the tibial slope so that it lies in the normal range.

As the review provided in Table 2-2 shows, among the 14 selected studies related to the alteration of the posterior tibial slope, eight studies found statistically significant results and most of them (n=7) show that performing OWHTO can lead to a significant increase in posterior tibial slope. Increases are variable among studies. The meta-analysis performed by *Nha et al*. found an average of 2° increase after pooling the data of 27 studies with various measurement methods [111]. As this alteration is relatively small, they concluded it may have little effect on the biomechanics of the cruciate ligaments. Higher increase rates were reported by other studies such as the study performed by *Ozel et al*. [102], who reported a 7° increase in the posterior tibial slope

after OWHTO. This 7° increase is a major modification because it increases the tibial slope up to twice its initial value but the authors have found no correlation between the postoperative Lysholm knee scores and the increase in the posterior tibial slope angle. From the authors' view, this can imply that the clinical outcome scores might not be completely capable of representing the alterations in the radiographic outcomes such as the posterior slope. This idea is supported by the literature review conducted by *Yan et al*. [112] to compare the outcomes of navigated HTO and conventional HTO. Despite the significant improvement in the radiographic outcomes using navigated HTO, they have indeed observed that these improvements have not yet been reflected in clinical outcome scores.

2.4.3 Patellar position modifications

From the biomechanical perspective, it is expectable that mono-planar OWHTO causes a decrease in patellar height by distalization of the anterior tibial tuberosity which is the insertion of the patellar tendon. This argument has been put to test in 11 out of 12 studies reviewed in this research, through monitoring the patellar height alteration after OWHTO (Table 2-3). Among the various indices used to assess patellar height, the Blackburne-Peel has been the most popular and been used by 9 out of 12 studies. The reported Blackburne-Peel ratio has decreased in all these studies with 8 of them reporting statistically significant data, thus proving the patellar height decrease after conventional OWHTO. However, this type of consensus is lacking about the Insall-Salvati and modified Insall-Salvati indices. Among the seven studies reporting the Insall-Salvati ratio, only three of them have monitored a statistically significant alteration with two of them reporting a decrease and one of them reporting an increase in this ratio for a conventional OWHTO. This lack of consensus, as mentioned by *Hanada et al*. [115], seems to be related to the fact that the Insall-Salvati ratio shows the length of the patellar tendon and not necessarily represent the

patellar height against the femur. The Blackburne-Peal ratio evaluates the patellar height, but in the context of HTO studies its eligibility can be questioned because it is dependent on the posterior tibial slope which is itself a variable in HTO. As a result, other indices such as Caton-Deschamps and Modified Blumensaat could be more eligible. Caton-Deschamps ratio has been used by three studies that have all reported a significant decrease in patellar height after OWHTO. Modified Blumensaat has been proposed by *Hanada et al*. and they have shown a significant decrease in the patellar height after OWHTO [115].

Regarding the modification of the patellar tilt, four studies have shown significant alterations in the patellar tilt with three of them showing significant decreases in lateral patellar tilt between 1.8° and 2.2° [114,119,135] and one of them reporting a significant increase of medial patellar tilt of 2.2° using an MRI based method [85]. With regards to patellar shift, only *D'Entremont et al*. found a significant increase of 0.94 mm ($p < 0.001$) compared to the pre-operative situation using an MRI-based method [85]. Performing biplanar osteotomies could reduce patellar height alteration by keeping the tibial tuberosity connected to the proximal fragment. The comparison of OWHTO groups with or without biplanar osteotomy shows interesting results. *Longino et al*. [116] showed a significant difference between the two groups with a decrease of 0.09 of the patellar height in the bi-planar osteotomy group against 0.19 in the mono-planar group for the Caton-Deschamps index. *Park et al*. [114] also found a significantly smaller decrease in modified Blackburne-Peel and Caton-Deschamps for the bi-planar versus mono-planar group.

2.4.4 Biomechanical studies

The amount of alignment correction is closely correlated to the pressure distribution in the two compartments of the knee. This arises another research line with the objective of seeking the optimal correction angle through monitoring the stress distribution of the cartilage using FE and

multibody modelling techniques. *Zheng et al*. have proposed a subject-specific modelling procedure to identify the alignment that balances the compressive and shear stresses of the cartilage [125]. Similar studies have been also performed for closed-wedge high tibial osteotomy such as the study of *Trad et al*. [126]. A preliminary FE study performed by *Martay et al*. makes a general conclusion and proposes that the safe zone for WBA of the lower limb can be between 50% and 60% of the mediolateral tibial width (0° varus-valgus to 2.6°–2.8° valgus) [127]. This range is lower than the recently refined 62% to 66% correction range on the basis of the traditionally used correction range of *Fujisawa et al*. [83].

However, in order to consider the findings of the aforementioned studies to be valid and applicable in the medical field, there are various points that require further investigation. The high importance of the soft tissues in maintaining the correction angle in HTO seems to be almost neglected by ignoring the alteration in ligament tensions after the realignment of the knee and by not considering the preexisting laxities that could be present in the ligaments. This is true both in models that are using simplified axial ligaments [126,127] or in more advanced studies where the 3D FE representative of the ligaments are present [125]. On the contrary, the results of the multibody study performed by *Purevsuren et al*. show that pre-existing laxity in MCL has an effect on the contact distribution after HTO [128].

Simulating the HTO surgery through applying varus/valgus bending moments in some of the aforementioned studies (like the one from *Mootanah et al*. [24]) seems not to be sufficient for concluding about the correction angle. In this case, the only applied effect is indeed the change of direction of the weight-bearing axis and not the alteration in the soft tissues. In addition, performing studies that take into account the dynamic aspect of knee function at various flexion angles seems to be required in order to better investigate the unsatisfactory results of HTO. Thirdly,

the validation of the model and, as part of it, the adjustment of the material properties, are considered as required steps in patient-specific studies designed to obtain the proper alignment to be used [24]. However, this issue has been undervalued in many of the performed studies with this motivation. As a result, although there is a high potential in using FE studies to assist in redefining the correction angles both in general and patient-specific cases, the existing models with that objective tend to oversimplify the problem. However, these simplified studies with their biomechanical point of view can also play an important role in better distinguishing the involving factors in HTO outcomes and thus better designing the clinical and cadaveric studies.

2.5 Conclusion

The systematic review performed in the current study highlights the existence of a correlation between the opened wedge during HTO and surgical complications such as increased posterior tibial slope, patellar height decrease, and MCL tightness. Thus, in order to be able to come to a better consensus on the alignment principles and surgical techniques of HTO, the role of parameters such as the pre-operative soft tissue condition, tibial slope, and limb alignment should get distinguished. The ability of biomechanical simulations in isolating the involved parameters can play an important role in this process. However, this point has not been under the spotlight. As a result, it seems necessary to address the soft tissue aspect of HTO through biomechanical simulations. Specifically, further insight is required about the role of MCL in achieving tibiofemoral contact balance. Additionally, the correlation between patellar tracking and the opened wedge as well as its impact on muscular forces shall be further investigated.

In the upcoming chapter, we are going to start the procedure towards the generation of a modular combined FE-multibody model of the lower limb that can be used for further analyzing the aforementioned issues about high tibial osteotomy.

3

Forming a dataset for a modular lower limb model

In the current chapter, the necessary imaging data has been collected from a healthy subject to form a dataset to be used for various FE-multibody models to be generated in the upcoming chapters. This dataset will contain the geometry of the joints, muscles, articular and connective tissue present in the lower limb. Imaging data at different flexion angles has also been recorded that will be used for collecting patellofemoral and tibiofemoral kinematic data points that can be used for model evaluation or as passive knee flexion simulation input. Gait analysis is performed on the same subject and the session specifications are presented here.

3.1 Subject information and image acquisition

A healthy subject (male, 40 years old, 94 kg, 1.73 m) was a volunteer for participating in the experimental data collection that was part of a pilot study approved by an ethical committee (MammoBio MAP-VS pilot study, IRMaGe platform, Univ. Grenoble Alpes). He gave his informed consent to the experimental procedure as required by the Helsinki declaration (1964) and

the local Ethics Committee. The subject underwent a total of 5 sessions of non-weight-bearing Magnetic Resonance Imaging (MRI) using a clinical MRI system (Achieva 3.0T dStream Philips Healthcare) and one session of computed tomography (CT) scan.

The CT scan of the full lower extremity was done with the subject lying in the supine position and in a low energy procedure to limit the risks associated with exposure. The slices had sagittal and coronal intervals of 0.43 mm and an axial interval of 0.8 mm. The corresponding resolution for the right leg was 512×512×1266 pixels. This scan was taken to capture precisely the surfaces of the full bones that will be used as a reference for registering the bones acquired from different MRI sets.

The first MRI session was performed with the objective of obtaining the full geometry of the lower limb muscles. As a result, images were obtained at pelvic, thigh, knee, and shank levels while the subject was lying still in the supine position (Figure 3-1). To acquire the images in a reasonable amount of time, the axial interval was set to be 6.99 mm, and the sagittal and coronal intervals were 0.97 mm.

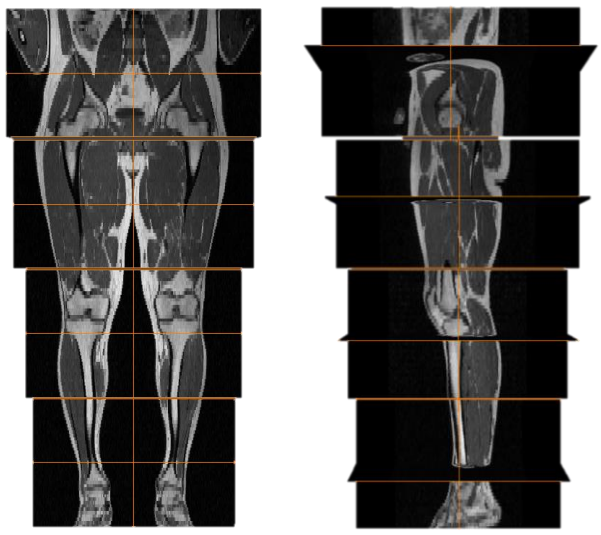

Figure 3-1, The MRI of the lower extremity from frontal and sagittal views

The second MRI was obtained from the subject's right knee with the objective of capturing the articulation, the connective tissues, muscle insertions, and tendons more precisely (Figure 3-2). The image resolution was 512×208×512 pixels taken at 0.31×0.7×0.31 intervals respectively in the axial, sagittal, and coronal views. The subject was lying in the supine position with an approximate 25° knee flexion. The third to fifth sessions of MRI were conducted with the objective of model validation with passive deep knee flexion and are explained in section 3.3.

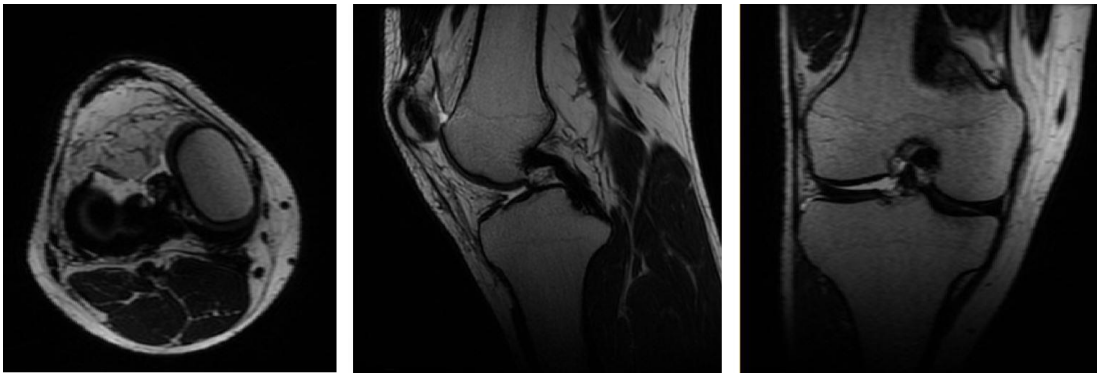

Figure 3-2, The high-resolution MRI of the right knee from axial, sagittal, and coronal views.

3.2 Geometry reconstruction

Manual segmentation was performed in Amira 6.5.0 in order to prepare the model geometry as well as the surfaces required during the other steps of the study such as model validation and registration. The CT scan was used to segment the full surface of the lower limb bones in the extended position. This included the sacrum, bones of the pelvis, femur, patella, tibia, fibula, and the bones of the foot. The first objective of this segmentation was that the generated surfaces of the femur and tibia will be used to register the bones segmented from different MRI sets. This will be used in the process of moving the segmented bony and soft tissues to the same frame and combining the information obtained from different images to build the models. The second

objective of this segmentation procedure was to define the bony landmarks required for the definition of the lower limb segment and joint frames.

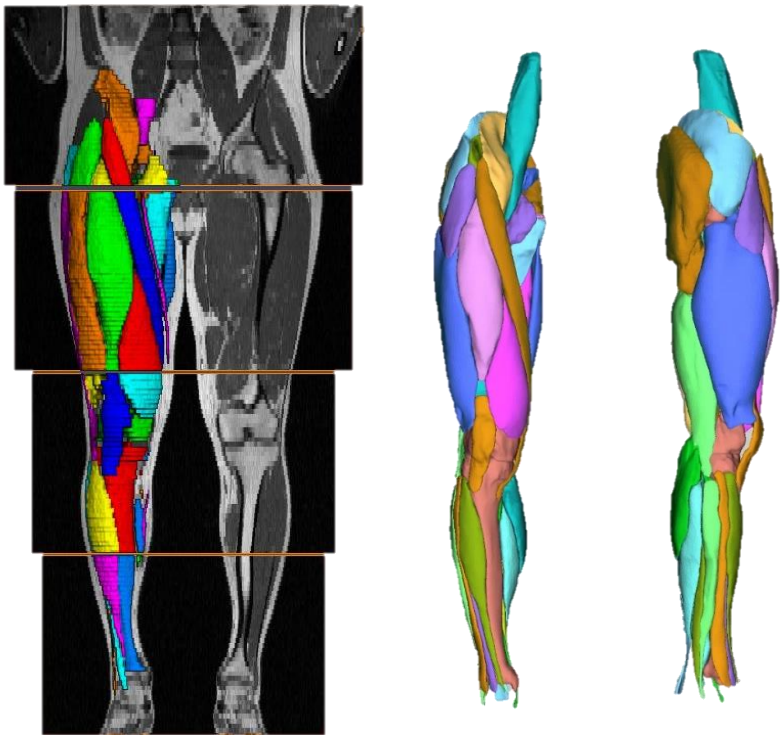

Figure 3-3, The segmented lower extremity muscles from MRI, the colors in the left-hand side image are chosen randomly and each muscle may be represented by multiple colors at different image levels. The final muscle surfaces are shown in the middle and right images from frontal and sagittal views.

The MRI of the lower extremity was segmented to reconstruct the surface of the lower limb muscles at the thigh and shank levels as depicted in Figure 3-3. This segmentation was performed to form a complete dataset of the subject's muscle geometries and pursued several objectives: firstly, to extract the geometry of the muscles to be used for FE model generation. Secondly, to obtain the muscle volumes, muscle-tendon attachment sites, and muscle line of actions to be used in the musculoskeletal models. The segmented muscle surfaces are listed in Table 3-1.

Table 3-1: The list of the segmented muscle-tendon parts from lower extremity MRI. The detailed 3D geometry of all the muscles has been obtained.

1. Semitendinosus	14. Biceps Femoris Long Head	27. Adductor Longus
2. Gracilis	15. Biceps Femoris Short Head	28. Adductor Brevis
3. Semimembranosus	16. Peroneus Longus	29. Quadriceps Tendon
4. Sartorius	17. Peroneus Brevis	30. Peroneus Tertius
5. Rectus Femoris	18. Extensor Digitorum Longus of Foot	31. Gluteus Medius
6. Vastus Lateralis	19. Tibialis Anterior	32. Gluteus Maximus
7. Vastus Intermedius	20. Extensor Hallucis Longus	33. Gluteus Minimus
8. Popliteus	21. Tibialis Posterior	34. Pectineus
9. Adductor Magnus	22. Flexor Digitorum Longus of Foot	35. Illiacus
10. Vastus Medialis	23. Flexor Hallucis Longus	36. Psoas
11. Achilles Tendon	24. Tensor Fasciae Latae	37. Quadratus Femoris
12. Plantaris	25. Gastrocnemius Medial Head	38. Gemellus
13. Soleus	26. Gastrocnemius Lateral Head	39. Piriformis

The same process of manual segmentation was done on the high-resolution MRI taken from the knee at 25° flexion with the objective of obtaining a more precise geometry of the joint and the articular tissues (femoral, patellar, and tibial cartilages and menisci), as well as ligaments (collateral, cruciate, patellar ligament and patellar retinacula) and tendons (Figure 3-4). In addition, the muscle parts captured within the field of view of the image were segmented. This completes the dataset of the muscle geometries and can be used for combining the segmented tendon surfaces with the muscle surfaces acquired from the lower extremity MRI.

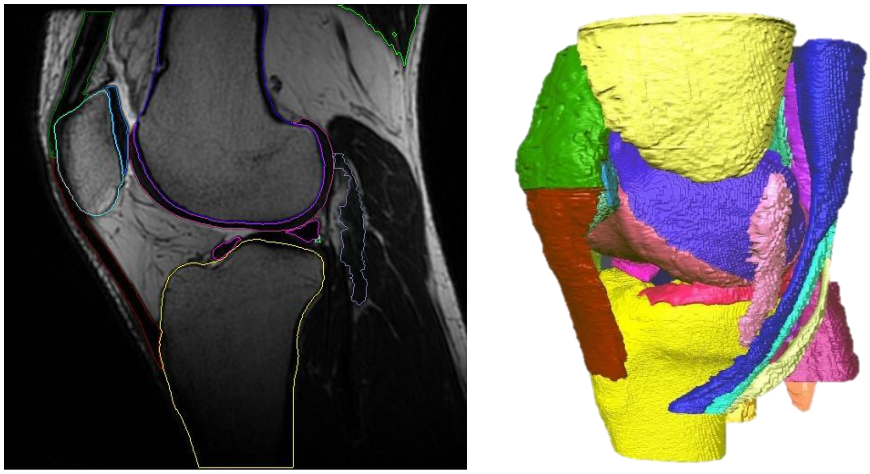

Figure 3-4, Left: Segmentation process on the knee high-resolution MRI, Right: Segmented surfaces of the joint articulation, ligaments, tendons, and muscle insertions.

Followed by the segmentation of the knee MRI at 25° flexion, the geometry dataset was completed. This dataset is used at various steps throughout the study and enables us to generate a FE model of the knee and muscles, as well as musculoskeletal models of the lower extremity with various levels of complexity.

3.3 Data acquisition for passive deep knee flexion simulation

As the next step in the workflow of this chapter, the third to fifth MRI sessions were conducted. The objective of these acquisitions was to obtain the required data for simulating passive deep knee flexion as well as model validation and material parameter optimization. For this purpose, the subject was lying in the left lateral recumbent position and positioned his knee at three different flexion angles for each acquisition. The MRI of the right knee was captured having 0.5 mm intervals in all planes and a resolution of 480×320×480 pixels in the axial, sagittal and coronal views.

The three different knee positions during the third to fifth MRIs are depicted from the sagittal view in Figure 3-5. The knee was at 55.6°, 99.6° and 137.5° flexed respectively during the first to the third MRI. The ankle was in a neutral position while taking the MRIs. However, due to the limited bore width of the MRI machine, the subject needed to flex his hip slightly (about 10°) in the MRI of the 99.6° flexed knee. The hip was not flexed during capturing the other two MRIs.

Figure 3-5, The sagittal view of the right knee MRI at three different flexion angles

It is important to be mentioned that choosing MRI as the imaging modality in this step was due to the implicit goal of completing a dataset to be used by further studies at the laboratory focused on the meniscus deformation at high degrees of knee flexion. The segmented bones are depicted in Figure 3-6.

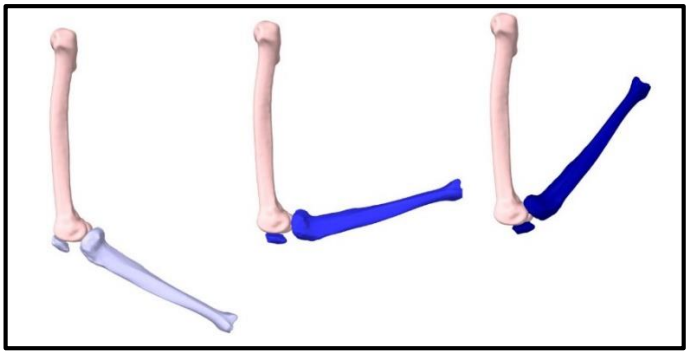

Figure 3-6, The bone surfaces segmented from the three flexed MRIs.

3.4 Gait analysis

Gait analysis was performed on the same subject from which we obtained the imaging data. The analysis was conducted in collaboration with Raphaël Dumas at the CHU Lyon-Sud gait laboratory. The room was equipped with a motion analysis system and one floor-mounted force-platform in order to simultaneously measure the kinematics and the kinetics of the subject during gait (Figure 3-7). The motion analysis system was a passive optoelectronic system made up of eight Prime13 cameras (Optitrack, NaturalPoint, OR, USA) for evaluating the trajectories of different body segments, their movements, angles, and variations with time during motion of the subject. Each camera consisted of a pulsed projector made up of LEDs attached around the camera lens. During the analysis, the incident rays produced by the LEDs were reflected by the retro-reflective markers in the same direction. In the middle of the walking lane, a platform AMTI® force (dimensions 0.5m x 0.4m, Advanced Mechanical Technology, Inc., Watertown, MA, US) was positioned. This experimental device allowed us to analyze the distribution of forces acting on the plantar surfaces of the subject's feet. Data from the plantar force was recorded at a frequency of 200 Hz.

The subject was equipped with 42 retro-reflective markers fixed to the recognized anatomical landmarks with double-sided tapes, according to the multi-segmental 3D models of the lower limb [136,137]. In the first step, the subject was asked to walk barefoot, in a 10m walking lane from the same start position at a self-selected speed. After the subject becomes familiar with the walking lane, data acquisition begins and stops as soon as the subject has completed approximately ten walking cycles. Five valid gait cycles are recorded. For a gait cycle to be valid, it must meet the following criteria: a walking speed within the walking lane, a regular stride length, and no visual adjustment of the gait pattern during contact with the force-platform [146]. After the quantified

performance of the walk, the markers were removed from the anatomical landmarks. As a result, the instantaneous positions of markers located on the skin surface obtained using stereo photogrammetry were measured based on optoelectronic sensors and external forces were measured using the force-platform [147].

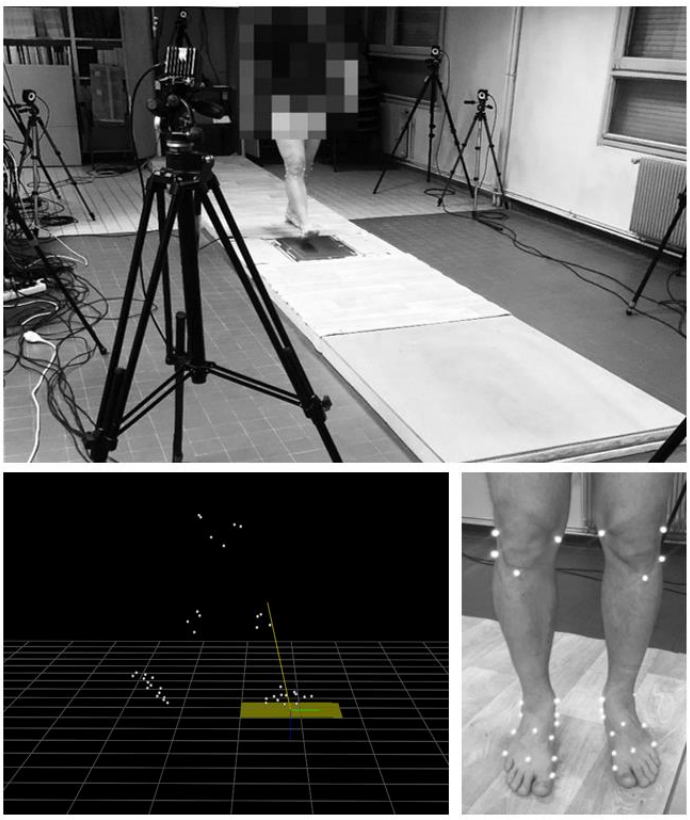

Figure 3-7, Top: the motion analysis system and force-platform mounted in the middle of the 10m walking lane. Bottom right: placement of retro-reflective markers. Bottom left: motion capture and force-platform data presented in c3d format.

3.5 Forming the dataset

As previously mentioned, these images were taken as a part of the workflow for the completion of a dataset to be used for modular model generation. For this goal, the segmented surface of the femur from CT scan was used as a reference to transform all the different geometrical parts (including bones, muscles, connective and articular tissues) obtained from different MR images to

the same coordinate frame. In order to do this, the transformation matrix between the surfaces of the femur that were manually segmented in all CT and MRI images was estimated. This step was conducted by performing a manual 3-point registration process for acquiring a close initial estimation which was followed by an automatic global rigid registration process. The transformation matrices found between the femur surfaces were applied to all the other segmented parts in the corresponding image that resulted in bringing all surfaces to the same coordinate frame. A sample of this data is depicted in Figure 3-8. This process makes it possible to combine the data attained from various images and to design and generate multiple models. Additionally, from this data, we have extracted data points on bone positions that can be used for model validation in the following chapters.

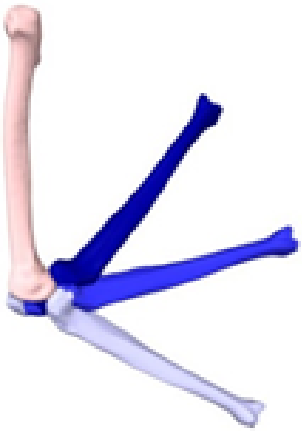

Figure 3-8, The bone positions after the step of registering the femur surfaces to transform the segmented surfaces to the CT scan coordinate frame.

4

Combined FE-multibody modelling of passive deep knee flexion, investigating different modelling techniques, and sensitivity analysis

The dataset created from the subject throughout the previous chapter contains valuable information about the geometry of the joints and muscles as well as articular and connective tissues that can be used for generating models with different levels of complexity. In this sense, an implicit aim of this chapter is to demonstrate various modelling possibilities that we can have using the Artisynth platform and this dataset. The explicit aim of this chapter is to evaluate these different modelling possibilities (through comparing with MRI-based data points) and decide on the design of the patellofemoral model to be used for application on HTO in chapter 5.

The findings of the review presented in chapter 2 demonstrated that the trajectory of the patella could alter after OWHTO. In this regard, questions about patellar trajectory were posed that we plan to seek their answers in chapter 5. Meanwhile, modelling the patellofemoral joint is a complex question as its motion is impacted by the variety of soft tissues attached to it and by contacts with

the femoral surface. As a result, before starting to move forward in that direction we will first need to find out which modelling strategy to use and validate our model predictions. In light of the aforementioned aims, a passive deep knee simulation was designed.

This chapter is structured into four main sections. In section 4.1 we explain the design of the passive flexion simulation in general and how the patellofemoral kinematics is extracted. Subsequently, in section 4.2, an MS model of the quadriceps muscle group represented by MT units is generated and a brief sensitivity analysis is done on the MT and patellar ligament parameters to see what parameters have the highest impact on the results. In section 4.3, the MS model of quadriceps muscles is generated with a 3D FE representation of muscles and the predicted patellofemoral kinematics are compared to the model with MT units. Finally, in section 4.4, new techniques to reduce the computational cost of FE models of the quadriceps muscle group are tested. In all the sections, the patellofemoral kinematic results are compared against the MRI-based data points to account for the validity of their predictions.

4.1 Designing a passive deep knee flexion simulation

The passive deep knee flexion simulation acts as a starting point in the framework of our study. This simulation can be used for demonstrating different modelling possibilities as well as finding the most suitable model for the HTO related study on the patellofemoral joint. The outputs of this simulation can be directly compared to the patellar position at different flexion angles acquired from MRI.

The idea is to impose the motion of the tibiofemoral joint based on the MRI segmented bones at the highest level of flexion and then to take the patellofemoral joint kinematics as the output of the simulation. This output can be directly compared to the MRI data points and help us to evaluate our modelling choices.

4.1.1 Simulation setup

A schematic view of the setup used for the simulation of passive deep knee flexion is depicted in Figure 4-1. As demonstrated, the bone positions at 25° knee flexion (the first MRI position) are used to define the initial position of the model. The pelvic bones and femur are fixed in their initial position. The foot bone and the fibula are constrained to the tibia and considered as a single segment. The patella is free to move in all its six Degrees of Freedom (DOFs) and its motion will be in response to the forces transmitted to it through the muscles and tendons, as well as contact forces.

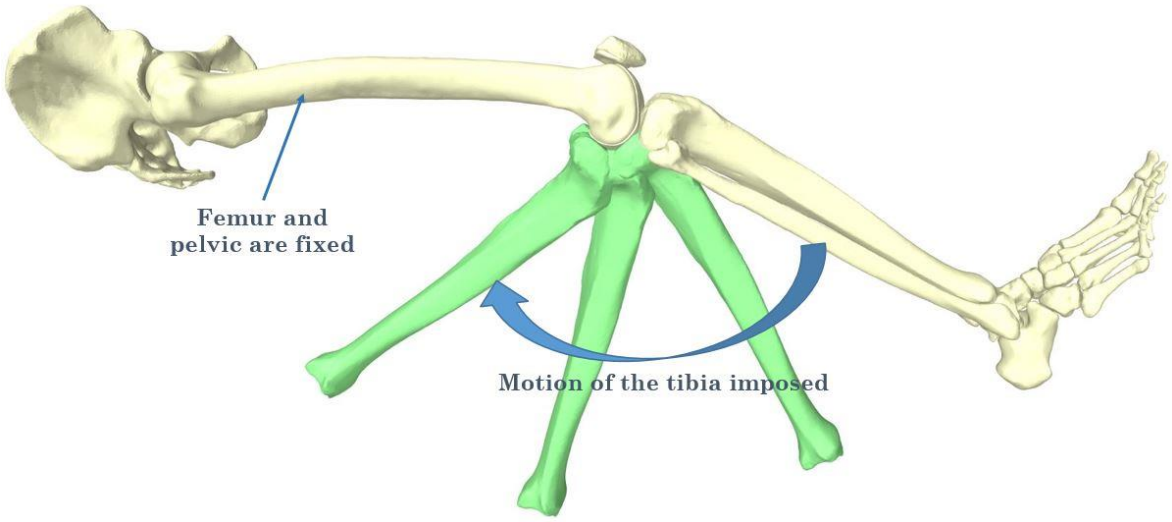

Figure 4-1, Schematic view of the passive deep knee simulation setup. The position of the combined shank and foot segment is controlled through the transformation matrix obtained from MRI at different knee flexion angles. The thigh and pelvic segments are non-dynamic. The patella is free to move in response to forces transmitted to it through the soft tissues and contacts with the femur.

Contacts are defined between the patellar cartilage and the femoral cartilage. The gravity is neglected and inertial parameters of the segments are not considered as they will not have any impact on the simulation of passive flexion. The reason for this assumption is that the femur and

pelvic segments are considered non-dynamic and the motion of the combined shank and foot segments is imposed through a pre-calculated transformation matrix at each time increment. This setup will be used as the basis of the simulations conducted in this chapter.

4.1.2 Segment frames and patellofemoral kinematics

Defining the local coordinate frames for the shank, patella, and thigh segments were required to impose the motion of the shank and to extract the kinematics of the patella. The bony landmarks and knee Joint Coordinate System (JCS) are defined based on the ISB standard defined for the tibiofemoral joint by *Grood et al*. [138]. The exact same definition of the JCS is used for the patellofemoral joint through replacing the tibial local frame with the patellar frame that is defined to be parallel to the femoral frame at full extension as demonstrated in Figure 4-2.

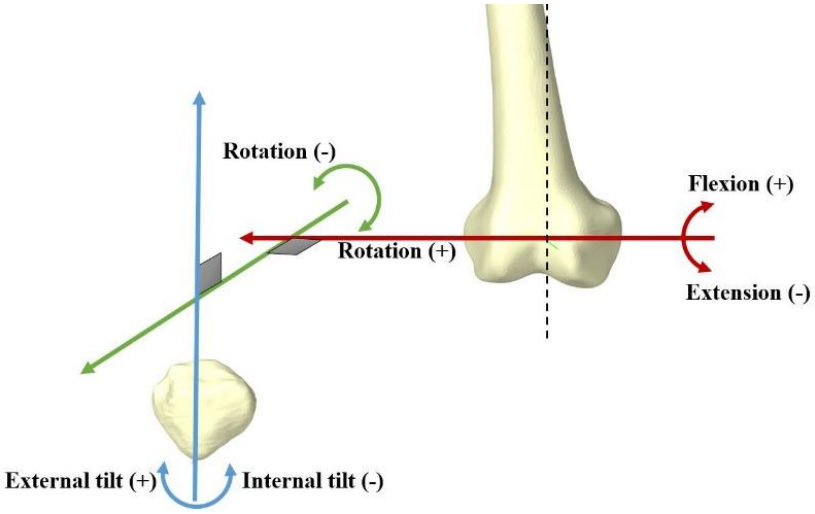

Figure 4-2, Description of the patellofemoral JCS: lateral translation or shift is the motion of the patella along the fixed femoral axis (red), anterior translation is along the floating axis (green) and the proximal translation is along the patellar fixed axes (blue).

For the calculation of the translations, the origins of the femur and shank local frames were both defined to be placed midpoint between the medial and lateral femoral epicondyles at neutral position (considered to be the bone positions while taking the CT scan). For the patellar segment,

the origin was defined to be located on the most distal point of the patella bone. As the patellofemoral kinematics was observed in response to the passive flexion of the tibia, the tibiofemoral flexion angle was defined as the independent variable and all the 6 DOFs of the patella were considered to be dependent on it.

4.2 MS model of the quadriceps muscle group using MT units

In this section, a model of the quadriceps muscle group represented by MT units is generated and used for a sensitivity analysis. For this purpose, the muscles and ligaments that are attached to the patella are modeled but the other connective tissues and muscles are excluded. The segmented geometry of the patellar ligament, medial and lateral patellar retinacula were used to define the insertion, number, and direction of the bundles required to represent each of these ligaments. The medial and lateral patellar retinacula was modeled as it can affect the patellofemoral joint and the force magnitude in the patellar ligament [139]. Each ligament bundle was modeled with a discrete number of strands. The strands had a non-linear stiffening spring behavior at low strains and had a linear stiffness at higher strains [140]. The force at each strand was formulated as follows:

$$f = \begin{cases} 0 & \varepsilon < 0 \\ \frac{1}{4} K_1 \, \varepsilon^2 / \varepsilon_1 & 0 \le \varepsilon \le 2\varepsilon_1 \\ K_1(\varepsilon - \varepsilon_1) & \varepsilon > 2\varepsilon_1 \end{cases} \qquad \text{Equation 4-1}$$

In this equation, f is the tensile force of the strand, K_1 is the stiffness, ε_1 is the strain limit set to 0.03, and ε is the strain in the strand. This choice will be conserved for all our future models as it has been shown that the use of elastic spring elements for ligaments provides acceptable results in the knee models [30]. The stiffness and reference strain (strain in the ligament when the joint is fully extended) in each bundle were adapted from the literature and in case more than one spring was proposed per bundle, the stiffness was divided between the springs as their respective tensions

act in parallel [141,142]. The patellar ligament was represented with a total of seven bundles consisting of three bundles for the central region and two bundles for each of the medial and lateral regions based on the results of the cadaveric study of *Yanke et al*. [143]. Five bundles were defined to represent the medial and lateral patellar retinacula with the respective total stiffness of 31 N/mm^2 and 97 N/mm^2 taken from the literature [144,145] while a 0.01 reference strain was assumed for them.

The muscle and tendon parts in the created subject dataset were used to define the line of action, attachment points, and via-points of the Vastus Lateralis (VL), Vastus Medialis (VM), Vastus Intermedius (VI), and Rectus Femoris (RF) muscles. The MT parts were defined as depicted in Figure 4-3. Wrapping around the femur surface was activated for these muscles using the novel method proposed by *Lloyd et al*. and implemented in Artisynth for computing wrapping paths across arbitrary surfaces [57].

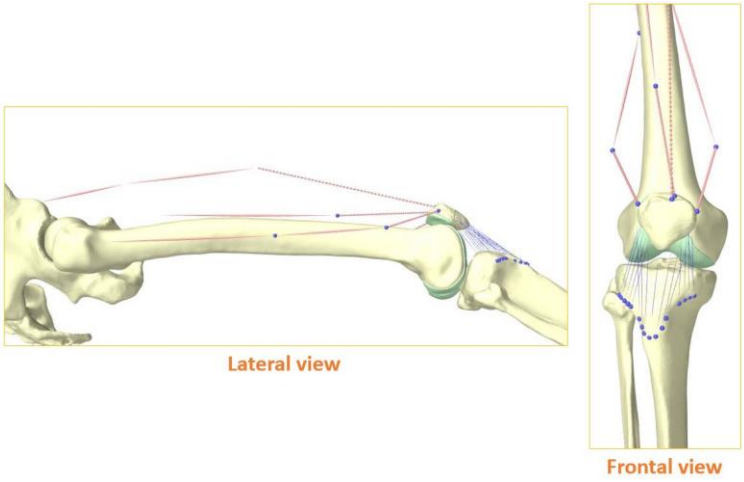

Figure 4-3, The model used for performing the sensitivity analysis on the parameters of the quadriceps muscles and patellar ligament

4.2.1 Muscle-tendon model

To model the MT parts for the quadriceps muscles, the 3-element Hill-type muscle model was used assuming rigid tendons. Such an assumption is made for simplicity reasons. To introduce the corresponding muscle force equation and parameters, let's start with the extended version of the Hill-type MT model which was proposed by Zajac [146]. For this model as shown in Figure 4-4 (adapted from [146,147]), muscle fibers are assumed to be straight and parallel, to have an equal length, and to be coplanar. The muscle fibers are attached to the tendon part at a pennation angle (α). When the muscle contracts and shortens, it is assumed that the distance h remains constant through an increased pennation angle.

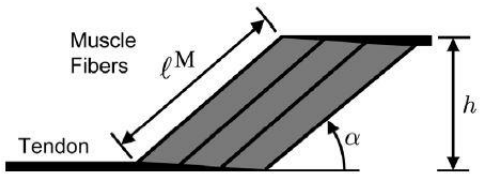

Figure 4-4 Geometric representation of muscle fibers and tendon simplified for being used in the MT model (figure adapted from [147]*).*

Based on this muscle geometry we can define a muscle-tendon unit (l^{MT}) represented by an active contractile element CE that is put in parallel with a passive element PE (responsible for the passive stiffness of connective tissue) and these elements are in series with the tendon T (Figure 4-5). This tendon is usually modeled as a nonlinear spring. However, in the case of our study, we have assumed the tendon part to be rigid for simplicity and have replaced it with an inextensible cable having the length (l^T) as depicted in Figure 4-5.

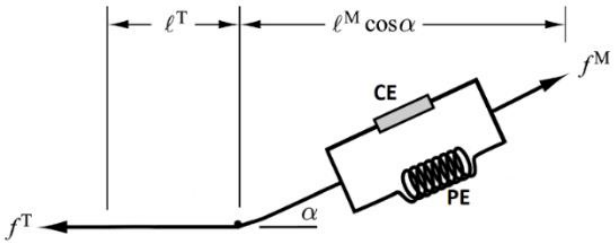

Figure 4-5 Schematic representation of the rigid-tendon Hill-type muscle-tendon element.

With this simplification, the muscle length (l^M) is determined with the following equations based on the literature [147].

$$l^{MT} = l^T + l^M \cos\alpha \qquad \textit{Equation 4-2}$$

As the height of the parallelogram h is constant (Figure 4-4), using the optimal muscle length and pennation angle we can have:

$$h = l^M \sin\alpha = l_0^M \sin\alpha_0 \qquad \textit{Equation 4-3}$$

we know that the force in the muscle part (f^M) and the tendon part (f^T) are equal to the force in the unit (f^{MT}) and solving for the muscle force will give:

$$f^{M*} = f_0^M\left(a\, f^l(\tilde{l}^M) f^v(\tilde{v}^M) + f^{PE}(\tilde{l}^M) + \beta\tilde{v}^M\right)\cos\alpha \qquad \textit{Equation 4-4}$$

f^l and f^v are the active-force–length and force-velocity curves, respectively. The f^l peaks at the optimal fiber length l_o^M. As further explained by *Millard et al.* [147], $\tilde{v}^M$ and $\tilde{l}^M$ are muscle part velocity and length normalized by their optimal values. The f^{PE} is the passive force length curves, f_0^M is the maximal isometric muscle force, and a is the muscle activation that ranges from 0 to 1. β is a damping factor. Since a muscle can generate only tensile force, its force is constrained to remain positive:

$$f^M = \begin{cases} f^{M*} & if \quad f^{M*} > 0 \\ 0 & otherwise \end{cases} \qquad \textit{Equation 4-5}$$

In our model we have also assumed that the velocity of the muscle does not play a crucial role other than damping which thus simplified the equation as follows:

$$f^{M*} = f_0^M\left(a\, f^l(\tilde{l}^M) + f^{PE}(\tilde{l}^M) + \beta\tilde{v}^M\right) cos\,\alpha \qquad \textit{Equation 4-6}$$

For the mentioned curves we have fitted 1D cubic Hermite splines to the active and passive muscle force-length curves from Millard 2012 [147].

4.2.2 Sensitivity analysis of patellar ligament and quadriceps MT parameters

In this section, the passive flexion setup is used to test the sensitivity of the patellofemoral kinematics to the MT parameters and stiffness of the patellar ligament to see uncertainty in which parameters have the largest effect on the outcomes. Four parameters were studied in this sensitivity analysis as concerns the quadriceps muscles, namely the optimal muscle fiber lengths (l_o^M), the pennation angles (α), the physiological cross-sectional areas (PCSA) as well as the tendon length. The nominal values for these parameters were estimated using the means explained in the literature [148]. The maximum isometric force for each muscle was calculated by multiplying the measured PCSA by a specific tension of 61 N/cm2 [148]. It is important to mention that the repeatability of some of the measured values was relatively low. This highlights the need for performing a sensitivity analysis to enhance parameter estimation in future studies with similar models. The nominal values estimated for the four MT parameters are presented in Table 4-1. For the sensitivity analysis, each MT parameter of each of the four muscles was perturbed according to the average anatomical variability calculated by *Ward et al*. [149]. The values for PCSA, tendon length, and optimal fiber length were perturbed by ±10% and ±20% of their initial nominal value. The pennation angle was perturbed by ±10% of its initial value.

Regarding the sensitivity analysis of the patellar ligament, the stiffness and reference strain used for each bundle were studied as parameters. It has been shown in the literature that the

variability of the ligament stiffness can be as high as 30% of the mean in controlled experimental studies [150,151]. As a result, to be in the safe zone, it was decided to perturb the stiffness values used for each bundle of the patellar ligament to ±10%, ±20%, and ±30% of the nominal values. Perturbations were independently assigned for each bundle, but the same parameter variation was prescribed to all strands within a bundle. The nominal bundle stiffness values were adapted from the literature [143]. The total stiffness of the central region (composed of three bundles) was set to $278\ N/mm^2$. The total stiffness of medial and lateral regions (each composed of two bundles) were set to $201\ N/mm^2$ and $173\ N/mm^2$ respectively. The nominal reference strain was assumed to be 0.02 for all the bundles of the patellar ligament at full extension. As the knee position in the model is corresponding a 25° knee flexion, we accounted for the ligament strain alteration from full extension. To analyze the sensitivity of the kinematic results to the reference strain at full extension, the reference strain was perturbed to 0.0 and 0.04 values.

Table 4-1: Initial estimated values for the Quadriceps MT parameters. These values are used as the nominal values in the sensitivity analysis

Muscle	PCSA (cm2)	Tendon length (m)	Optimal fiber length (m)	Pennation angle (°)
RF	31	0.23	0.1287	14
VL	37	0.07	0.2	10.7
VM	32	0.1	0.17	13.7
VI	39	0.13	0.108	7.5

The sensitivity of the model was measured by defining a custom-made Sensitivity Index (SI) inspired by the study of *Carbone et al.* [152] but modified to meet the needs of our study. This sensitivity index (SI) can quantify the effect of perturbation of each parameter on each DOF of the patella.

$$SI_i = \frac{\int_0^T \left| X_i^{new}(t) - X_i^{nominal}(t) \right| dt}{\int_0^T |X_i^{nominal}(t)| dt} . 100\%, \quad i = DOF \qquad \textit{Equation 4-7}$$

The SI is computed for each perturbation. t is the simulation time step that ends at $t = T$ and is equivalent to the completion of the deep knee flexion simulation. X_i^{new} is the kinematics result for each DOF denoted with i (three translations and three rotations of the patella) that is attained as after perturbation of the MT or ligament parameter and $X_i^{nominal}$ denotes the same value for the simulation using the nominal parameter values.

To facilitate the process of concluding from the results, an Overall Sensitivity Index (*OSI*) is introduced. The OSI is the sum of the fraction defined in Equation 4-7 calculated over the 6 DOFs (denoted with i) and provided in Equation 4-8. This index quantifies the effect that perturbing a parameter by a given percentage can have on the overall kinematics predicted by the model.

$$OSI = \sum_{i=DOF} \mathrm{SI_i} \qquad \text{Equation 4-8}$$

Besides, the mean OSI computed for all perturbation amounts of one MT parameter of each MT part is also reported to summarize the sensitivity results and decide on the MT parameters that have the highest impact on the results.

4.2.3 Sensitivity analysis results

The predicted patellofemoral kinematics with the model having nominal parameters as well as the alteration in predicted kinematics in response to different parameter perturbations can be observed in Figure 4-6 to Figure 4-9. Sensitivity of the patellofemoral kinematics in its all 6 DOFs presented large variability to the perturbation of each MT parameter of each quadriceps MT part. For each perturbation, the SI was computed for each degree of freedom, and the OSI was calculated to summarize the impact on the overall kinematic outcome as presented in Table 4-2.

The mean of the OSI was computed over the different perturbation levels of the parameter and is reported in Table 4-3 to facilitate concluding about the overall impact of each parameter on each

muscle. As presented in Table 4-3 the optimal length followed by the tendon length of the Vastus Lateralis and Vastus Medialis muscles had the highest mean OSI values. As a result, these four parameters have the highest impact on the predicted patellofemoral kinematic.

Table 4-2: Complete sensitivity results for the MT parameter perturbation for the quadriceps muscle group. The SI (%) is reported for each DOF of the patella and prioritized in red. The OSI (%) as a result of each perturbation is prioritized in green.

Muscle	MT parameter	PCSA				Optimal fiber length				Pennation angle		Tendon length			
	Perturbation level / DOF	+20%	+10%	-10%	-20%	+20%	+10%	-10%	-20%	+10%	-10%	+20%	+10%	-10%	-20%
Rectus femoris	Lateral SI	1.3	0.9	0.9	1.4	2.6	1.9	2.2	3.7	0.5	0.5	2.8	1.9	2.2	3.2
	Anterior SI	0.2	0.1	0.1	0.2	0.5	0.4	0.4	0.8	0.1	0.1	0.5	0.3	0.3	0.6
	Proximal SI	0.6	0.4	0.4	1.3	2.1	1.6	2.0	4.0	0.2	0.2	2.2	1.7	1.6	3.3
	Flexion SI	0.6	0.3	0.3	0.8	1.9	1.4	1.4	2.5	0.1	0.1	2.2	1.3	1.1	2.0
	Rotation SI	5.8	4.2	4.1	6.1	11.0	8.5	9.9	16.1	2.3	2.3	11.8	7.7	9.3	13.5
	Tilt SI	4.8	3.7	3.5	5.6	8.1	7.6	8.3	13.7	1.9	1.7	8.9	7.4	7.3	11.7
	OSI (Sum DOFs)	13.3	9.7	9.3	15.4	26.2	21.3	24.2	40.8	5.1	4.8	28.4	20.3	21.7	34.3
Vastus medialis	Lateral SI	1.7	1.3	1.3	3.0	11.5	7.0	3.1	7.1	0.5	0.4	5.7	3.1	1.7	2.6
	Anterior SI	0.4	0.2	0.2	0.4	0.8	0.7	1.3	3.4	0.1	0.1	0.7	0.5	0.4	0.8
	Proximal SI	1.4	1.1	0.8	1.3	6.0	3.1	2.8	4.2	0.2	0.2	2.3	1.5	1.5	2.5
	Flexion SI	0.6	0.5	0.4	0.6	2.0	1.2	0.9	1.5	0.1	0.1	1.0	0.7	0.6	0.8
	Rotation SI	12.2	7.6	7.8	15.9	65.2	40.7	42.1	92.0	2.0	2.3	32.7	16.4	13.8	28.1
	Tilt SI	10.2	5.9	6.4	12.8	46.3	31.1	38.7	105.7	2.0	1.6	26.1	15.7	10.3	23.1
	OSI (Sum DOFs)	26.5	16.5	16.9	33.9	131.9	83.8	88.8	214.0	4.9	4.7	68.6	37.9	28.3	57.9
Vastus intermedius	Lateral SI	1.5	0.9	0.8	1.5	3.3	2.2	2.4	4.0	0.5	0.2	2.7	1.8	2.0	2.7
	Anterior SI	0.2	0.1	0.1	0.2	0.6	0.4	0.4	0.9	0.1	0.0	0.5	0.3	0.4	0.6
	Proximal SI	0.8	0.5	0.3	0.8	2.5	1.3	2.5	5.7	0.2	0.1	2.2	1.1	1.9	3.4
	Flexion SI	0.6	0.3	0.3	0.6	1.6	1.1	1.2	2.6	0.1	0.0	1.4	0.8	0.9	1.4
	Rotation SI	8.5	4.8	4.3	8.2	22.4	14.2	15.0	30.3	3.2	0.9	19.8	11.7	12.5	19.4
	Tilt SI	5.4	3.8	3.1	4.9	9.8	7.7	8.4	12.1	2.4	0.8	9.5	6.7	7.8	10.1
	OSI (Sum DOFs)	17.0	10.4	9.0	16.3	40.1	26.9	29.9	55.6	6.5	2.1	36.0	22.5	25.5	37.6
Vastus lateralis	Lateral SI	2.0	1.4	1.5	1.9	7.3	3.9	8.5	18.6	0.5	0.7	2.0	1.6	2.1	4.2
	Anterior SI	0.4	0.2	0.2	0.4	4.1	2.1	0.9	0.8	0.1	0.1	0.7	0.4	0.4	0.7
	Proximal SI	1.5	0.7	1.2	1.5	3.4	2.5	2.7	3.3	0.2	0.2	1.8	1.3	1.4	2.3
	Flexion SI	0.7	0.3	0.5	0.7	1.3	1.2	1.4	2.3	0.1	0.1	0.8	0.6	0.7	1.0
	Rotation SI	16.1	8.5	8.2	14.1	84.8	53.3	60.4	114.9	2.6	3.3	23.2	12.1	15.3	28.4
	Tilt SI	12.1	6.6	6.7	11.3	148.9	72.2	39.4	53.5	2.3	3.1	23.1	11.3	13.3	23.2
	OSI (Sum DOFs)	32.9	17.7	18.3	29.8	249.8	135.1	113.3	193.3	5.7	7.6	51.6	27.4	33.2	59.8

Table 4-3: The mean OSI (%) computed for the perturbation of four MT parameters of the quadriceps muscles, the table provides the priority list and shows which MT parameters have the most impact on which MT parts.

Parameter / muscle	PCSA	Optimal fiber length	Pennation angle	Tendon length
RF	11.9	28.1	4.9	26.2
VM	23.5	129.6	4.8	48.2
VI	13.2	38.1	4.3	30.4
VL	24.7	172.9	6.6	43.0

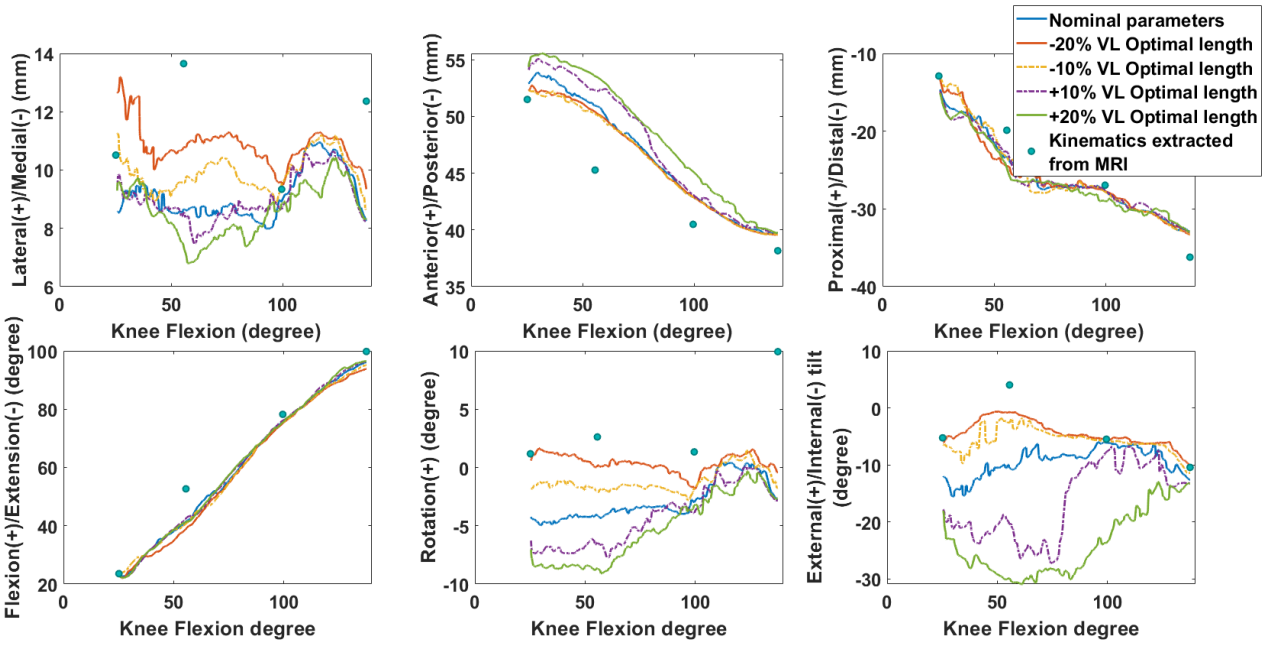

Figure 4-6, The impact of perturbing the optimal length of the Vastus Lateralis muscle on the predicted patellofemoral kinematics. The blue line represents the model using the nominal values reported in Table 4-1 without any perturbation. The blue circles are the kinematics obtained from the segmentation of patella in MRI sets at different knee flexion angles. The horizontal axis in all figures is the knee flexion angle. The vertical axes are the motion of the patella with respect to the femur in its six DOFs. The patellofemoral JCS is defined based on the ISB standards. The scale of the vertical axis is different in each figure.

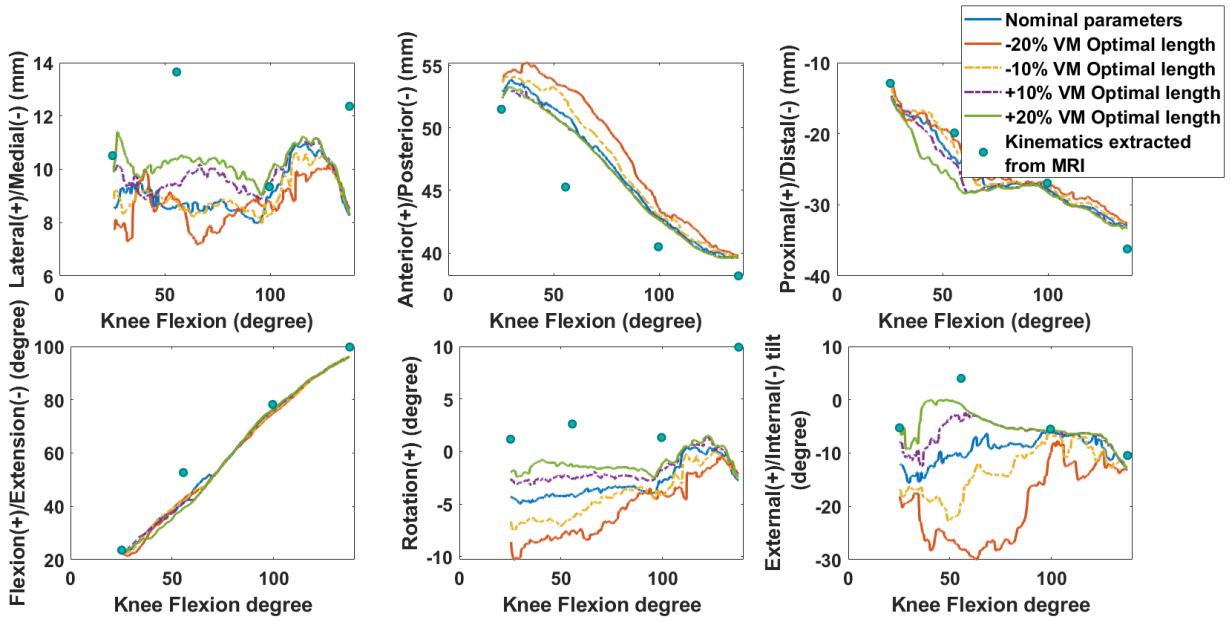

Figure 4-7, The impact of perturbing the optimal length of the Vastus Medialis muscle on the predicted patellofemoral kinematics. Further details are provided in the caption of Figure 4-6.

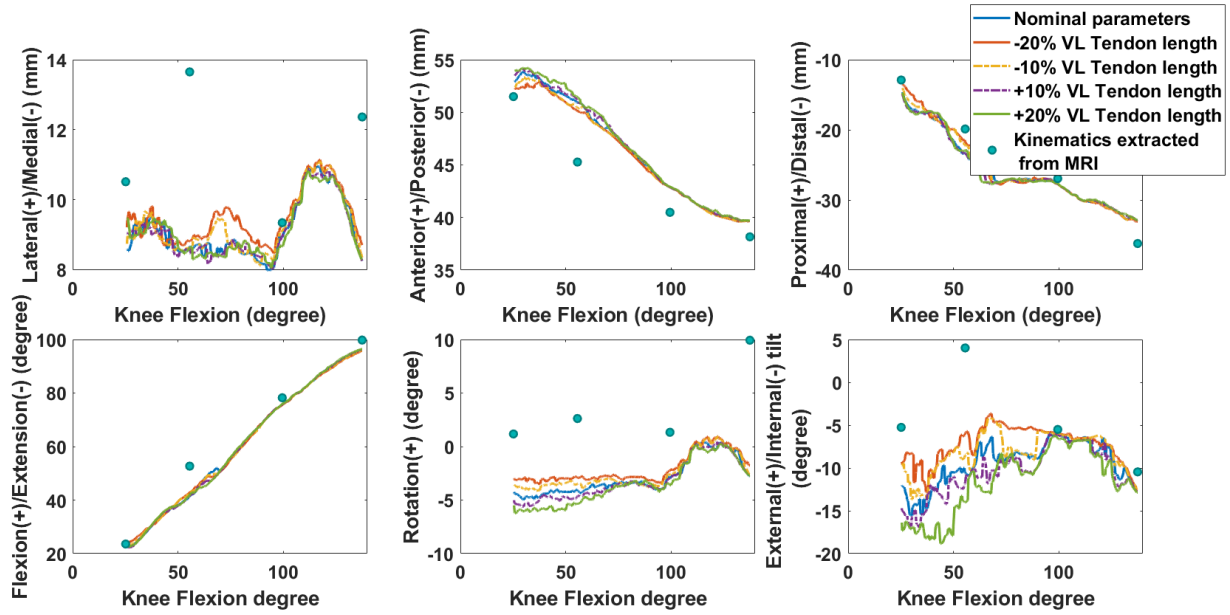

Figure 4-8, The impact of perturbing the tendon length of the Vastus Lateralis muscle on the predicted patellofemoral kinematics. Further details are provided in the caption of Figure 4-6.

The impact of the stiffness and the reference strain of the patellar ligament on the motion of the patella during passive deep knee flexion is depicted in Figure 4 10. The sensitivity index for each of the patella DOF (SI) as well as the overall sensitivity to each perturbation is presented in Table 4 4. As reported in this table, the maximum OSI is related to a -30% perturbation of the stiffness from its nominal value and is computed to be 40.8%. The mean OSI is computed for both parameters that are 25.28% and 29.05% respectively for the stiffness and reference strain.

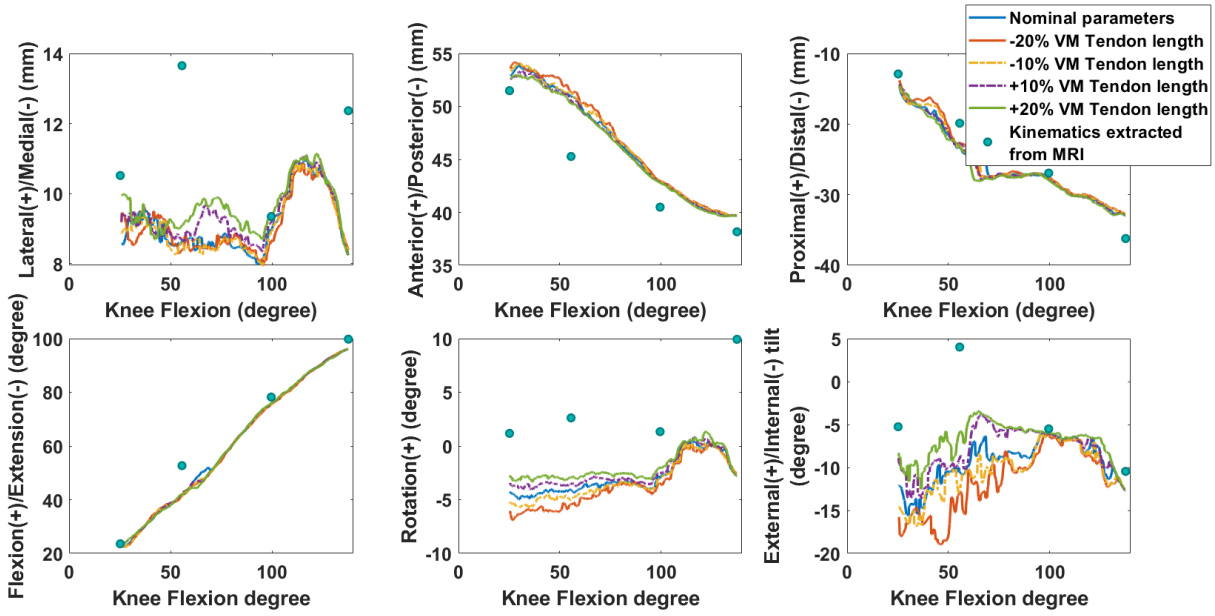

Figure 4-9, The impact of perturbing the tendon length of the Vastus Medialis muscle on the predicted patellofemoral kinematics. Further details are provided in the caption of Figure 4-6.

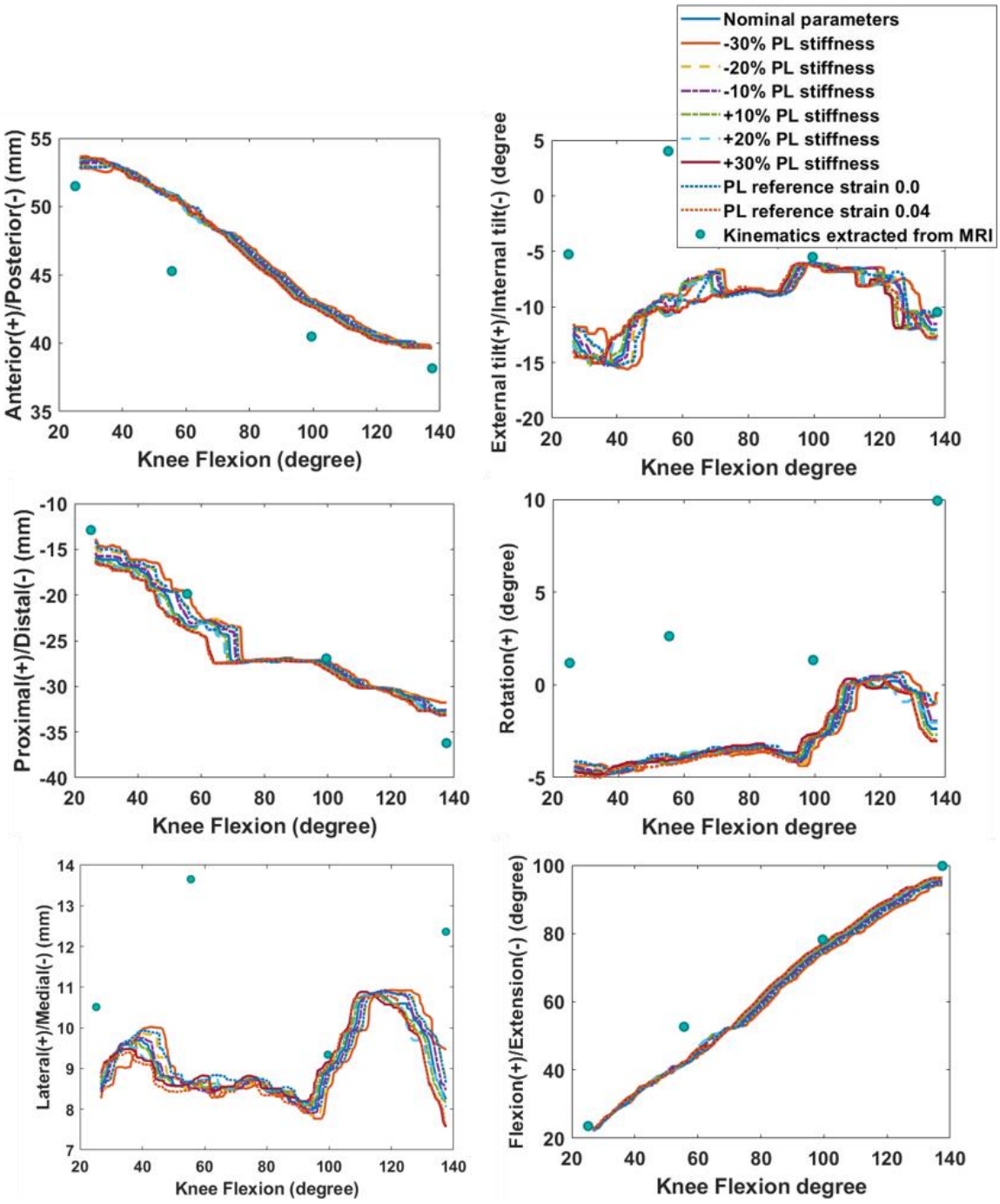

Figure 4-10, The impact of perturbing the stiffness value and reference strain of the patellar ligament on the predicted patellofemoral kinematics. The blue solid line represents the model using the nominal values without perturbation. The blue circles are the kinematics obtained from the segmentation of patella in MRI sets at different knee flexion angles.

Table 4-4: Complete sensitivity results for the perturbation of stiffness and reference strain of the Patellar Ligament (PL) bundles. The SI (%) is reported for each DOF of the patella and is prioritized in red. The OSI (%) for each perturbation level is presented and prioritized in green. The mean of OSI is computed for each parameter.

	Stiffness of PL						**Reference Strain of PL**	
Perturbation level / DOF	-30%	-20%	-10%	+10%	+20%	+30%	0.0	0.04
Lateral SI	4.3	2.9	1.6	1.3	2.1	2.8	3.0	2.9
Anterior SI	0.9	0.6	0.3	0.2	0.4	0.5	0.6	0.5
Proximal SI	4.1	2.5	1.4	0.8	1.6	2.7	2.7	2.8
Flexion SI	2.7	1.7	0.9	0.7	1.2	1.7	1.8	1.8
Rotation SI	15.4	11.0	7.2	5.8	9.1	11.2	11.3	11.4
Tilt SI	13.5	10.0	6.7	5.4	6.7	9.9	10.3	9.0
OSI (Sum DOFs)	40.8	28.7	18.0	14.3	21.1	28.8	29.7	28.4
Mean OSI	25.28						29.05	

4.2.4 Discussion on the sensitivity analysis

The objective of the extensive sensitivity analysis performed in this chapter was to distinguish the MT parameters and patellar ligament parameters that have a high impact on the patellofemoral kinematic outcomes. This process was conducted by computing the mean Overall Sensitivity Index (OSI) of each parameter to find the most effective ones on the patellofemoral kinematics.

Based on the results of mean OSI presented in Table 4-3 and Table 4-4, the optimal fiber length followed by the tendon length was found to have the highest impact on the outcomes. The pennation angle had the lowest impact among the MT parameters. The parameter perturbations of the VM and VL muscles had the highest impacts compared to the other two muscles. The mean OSI computed for the patellar ligament stiffness and reference strain parameters were noticeable but were not ranked among the highest OSI values.

In particular, this information can be relevant if the generated model is being used as an atlas model that needs to get scaled or morphed to generate patient-specific models. In such a case, the parameters found with the highest OSI will have to be adapted in priority to improve the model outcomes.

4.3 MS model of the quadriceps muscle group with 3D FE muscles

Having HTO patients in mind, if we aim to use combined FE-multibody modelling to assist the surgery or highlight some critical factors to improve the surgical outcomes, it is very important to know the extent of compromise that we are making by replacing the FE model of the muscles with MT parts. For this, the passive deep knee flexion simulation is used including a FE model of the quadriceps muscles and the corresponding results will be quantitatively compared to the results of a knee model that uses MT parts. The objective is to quantify the impact of the muscle modelling technique on the simulation outcomes.

4.3.1 Model generation

The FE model of the quadriceps muscle group (RF, VI, VM, VL) was generated using the muscle geometries reconstructed from the MRI segmentation. To control the number of finite elements and in particular to avoid very small elements, the segmented muscle surfaces were smoothed and treated to remove the unnecessary surface details and spikes. The end regions where the muscles insert into the bone were also simplified to avoid very small elements and to facilitate the meshing process with methods such as solid map meshing.

The process of mesh generation was conducted in HyperMesh 2019 (Altair Engineering, Inc., USA) to generate hexahedral dominant meshes (with control of element qualities and a limited number of wedge elements) for the four muscle parts as well as for the quadriceps tendon. The

mesh qualities were observed for all components and passed the conventional element quality tests defined as default in the software. The maximum element size was approximately 6mm to mesh the muscle parts and resulted in 2100 elements for RF, 1326 for VI, 9290 for VL and 2308 for VM. For the Quadriceps Tendon (QT), the approximate maximum element size was 3mm which resulted in a mesh with 5200 elements.

As previously mentioned, the complete dataset generated from the subject from different imaging inputs has been combined to share the same frame. Thus, the 3D meshed muscle components are simply imported into the musculoskeletal model of the passive deep knee flexion framework in order to replace the MT parts. All the other properties of the model are therefore conserved similar to what was defined in section 4.1.1 when introducing the model setup for passive flexion simulation.

Sliding contacts are defined between all muscle parts and between the femur and the Vastus Medialis and Vastus Lateralis muscles as they come in contact at higher knee flexion degrees. The nodes located in the proximal insertion of all the four muscles are attached to the femur head (that is supposed to be fixed in this simulation). The nodes of the VI muscle that are closer than one millimeter to the femur surface are attached to the femur. To represent the distal insertion of the four muscles to the QT, a distance limit with the QT is defined for each muscle, and all the nodes that are closer to the QT than the distance limit are attached to the proximal part of the QT. The nodes located in the distal part of the QT are attached to the patella. Contacts are defined between QT and the femur and the femoral cartilage, which is necessary at higher flexion degrees. The bundles of the patellar ligament and patellar retinacula are still modeled as nonlinear springs. The generated model is illustrated in Figure 4-11.

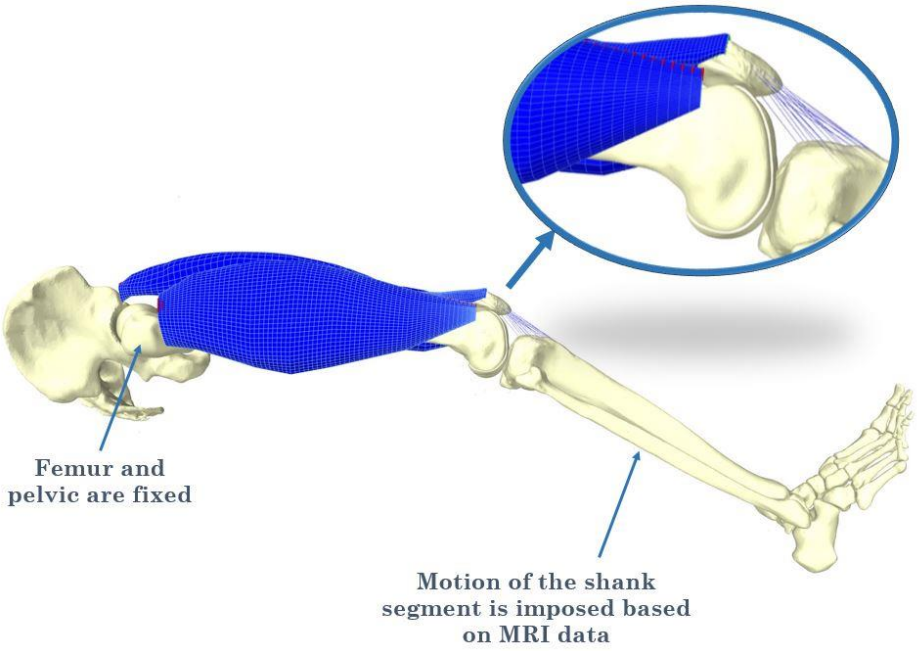

Figure 4-11, Generated combined FE-multibody model of the lower limb for simulation of passive deep knee flexion while modelling the quadriceps muscle group as FE components. Contacts are defined between the FE muscles with one another and the femur. The QT is connected to the four muscles and to the patella.

The constitutive law used to describe the muscle as a continuum material is separated into a passive and an active part. The muscle normally experiences large displacements and strains and has a nonlinear stress/strain curve. As a result, when the muscle is in the passive state and has no activation, its behavior can be best represented by using a hyperelastic material model [153]. This passive part can be treated as isotropic or transversely isotropic based on the level of complexity required for the model [154].

In the deep flexion simulation of the current study, the focus is mainly put on the overall behavior of the muscles and the patella kinematics. Therefore, we have assumed that the passive muscle behavior can be modelled with a nearly incompressible isotropic neo-Hookean hyperelastic material model. A neo-Hookean strain energy function (ψ) is defined as:

$$\psi = c_1(\bar{I}_1 - 3) + \frac{1}{D_1}(J-1)^2 \qquad \textit{Equation 4-9}$$

In which $\bar{I}_1$ is the first invariant of the isochoric part of the right Cauchy-Green strain tensor $\bar{C} = \bar{F}^T\bar{F}$ and $\bar{F}$ is the isochoric part of the deformation gradient *F* which determinant is *J*. c_1 and D_1 are material parameters that are respectively related to the shear modulus and the volumetric variations. The parameters used for the quadriceps muscles ($c_1 = 11.7\ kPa\ and\ D_1 = 16.3\ MPa^{-1}$) were defined based on the findings of *Affagard et al*. who presented an *in vivo* method to identify the behavior of the thigh muscles based on a displacement field obtained from ultrasound and digital image correlation techniques [155]. For the QT, a linear elastic material was assumed taking values of 30 MPa for Young's modulus and 0.46 for the Poisson ratio.

4.3.2 Model validation through comparison with MRI based kinematics

To compare the kinematic predictions of our knee models (the model with MT parts versus the one with FE muscles) with the MRI based data points and to find the model that gets the closest predictions to the images, the Normalized Root-Mean-Square Deviation (NRMSD) from the MRI data was computed. Normalization was performed for each degree of freedom because the scale and units are different. The sum of the normalized RSMD is computed over all 6 DOFs Equation 4-10 and reported as the total NRMSD for each perturbation.

$$NRMSD = \sum_{i=DOF} \frac{RMSD_i}{\bar{X}_i} \qquad \textit{Equation 4-11}$$

$RMSD_i$ is the root-mean-square deviation of the patellar motion in its ith DOF from the MRI data points in that DOF. $\bar{X}_i$ is the mean of the four MRI data points in the ith DOF. Lower values of NRMSD mean less deviation from the MRI data points that are directly extracted from images at different flexion angles.

4.3.3 Comparison between simulations with FE quadriceps muscles vs. simulations with MT parts

The simulation of passive deep knee flexion with the FE model of the quadriceps muscle group resulted in the patellofemoral kinematics presented in Figure 4-12. To facilitate the comparison, the results from the model with MT parts are imported in the same figure. Modelling the muscles as FE components seem to be affecting all the patellar DOFs and improving the patellar motion in multiple degrees while providing more smooth curves in all DOFs. To investigate how this change of modelling technique is affecting the outcomes in each DOF, the NRMSD is computed separately for each DOF and reported in Table 4-5. These results are demonstrating that the FE model is predicting closer results to the MRI based data points.

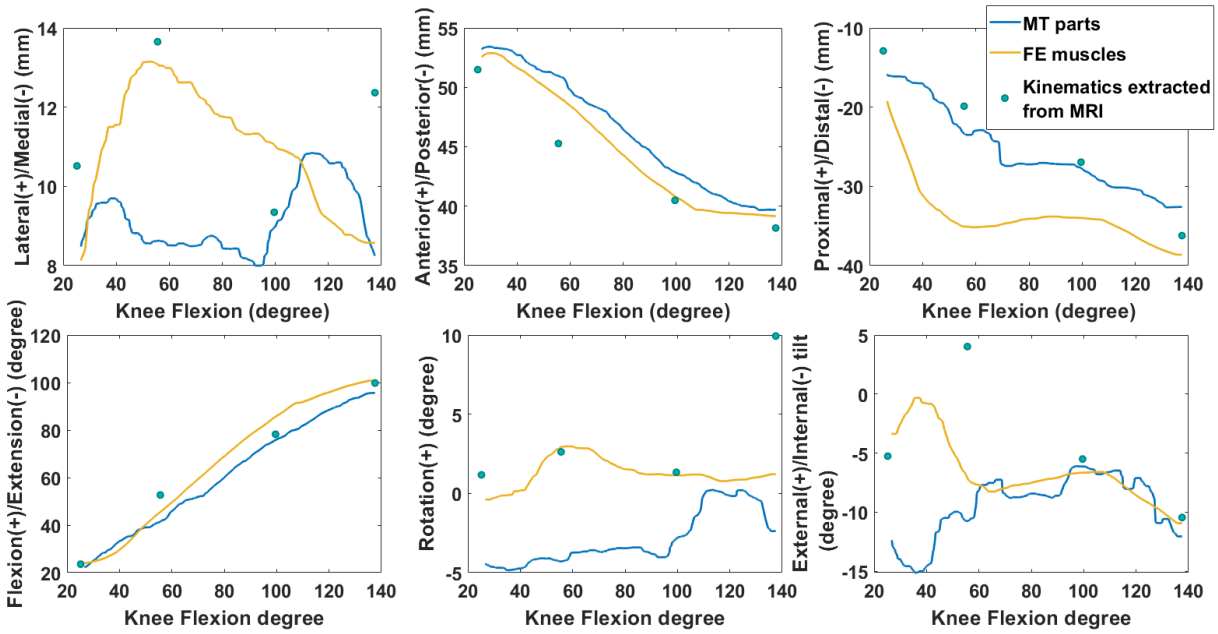

Figure 4-12, The impact of quadriceps muscle group modelling technique on predicted patellofemoral kinematics. The yellow line is showing the results of the model with FE muscle components. The blue line represents the model using MT parts. The blue circles are the kinematics obtained from the segmentation of patella in MRI sets at four different knee flexion angles.

Table 4-5: NRMSD computed for each DOF of the patella from the MRI data points for different models. The values are computed from the passive flexion simulation using MT parts and 3D FE parts for the quadriceps muscle group. The sum of the deviation of all DOFs is presented in the last column.

DOF of the patella / Muscle Model	Lateral	Anterior	Proximal	Flexion	Rotation	Tilt	Sum
MT parts of quad. muscle group	0.28	0.07	0.10	0.09	2.01	1.71	4.3
FE model of quad. muscle group	0.18	0.05	0.35	0.08	1.15	1.31	3.1

4.3.4 Conclusion on the required modelling complexity

In conclusion, the higher quality and stability of the obtained results for the patellofemoral kinematics clarifies that despite its higher computational cost, the FE representation of the quadriceps muscle model is a better choice for the investigation that we want to perform on the patellofemoral joint for assisting HTO surgery. This point plus the fact that we aim to analyze the muscle stress distributions makes our decision of using the FE muscle models definitive for the OWHTO study of the following chapter.

4.4 Mesh embedding technique to reduce the computational cost

Modelling the quadriceps muscles as FE components has the potential to enhance the predicted kinematics for the patella. However, this modelling technique suffers from having high preparation time as well as high computational cost due to the number of elements and complex contact between different muscles. Thus, reducing this time seems to be very challenging particularly for dynamic simulations.

To this aim, we will investigate a kind of model reduction technique that can provide a simplified version of the model and we control the loss of accuracy that it can cause in comparison with the full model (that includes nonlinear hyperelastic material models with complex contacts between muscles).

The proposed technique relies on mesh embedding that is a well-known approach in the computer graphics community but has more recently been applied to biomechanics [58,156]. The concept behind this technique is that a passive mesh (for instance a surface mesh) can be attached to an underlying FE grid. This passive mesh will be able to deform in accordance with the global deformation of the FE grid. This can be used as a model reduction technique because the number of dynamic DOFs for the resulting system is determined by the number of nodes in the embedding FE grid. By using a coarser FE grid this number can be significantly reduced. It is important to be mentioned that this technique can handle contact between the passive mesh and any other component that comes into contact with it using the conventional FE to FE contact detection methods. When the passive mesh comes into contact with another component, the contact force will be simply propagated back to the FE grid and deform the FE grid accordingly.

In the following, this technique is explained and tested on the FE model of the quadriceps muscle group with the objective to see if we can use this technique to reduce the computational cost without an important compromise on the quality of the results. To understand how this technique works, it is first required to explain the mechanism of “attachment” in the Artisynth platform [56], which enables us to connect surface mesh voxels to a deformable FE body.

4.4.1 ArtiSynth mechanism for connecting points to deformable bodies.

The attachment mechanism works by defining the coordinates of the attached component (x_a) to be a function of the coordinates of one or more master components to which it is attached (x_m) as follows:

$$x_a = f(x_m) \qquad \textit{Equation 4-12}$$

This implies that the velocities of these components have a linear relationship similar to:

$$\dot{x}_a = G_{am}\,(\dot{x}_m), \quad G_{am} \equiv \nabla f(x_m) \qquad \textit{Equation 4-13}$$

Based on the principle of virtual work, the force (f_a) of the attached point will be able to propagate back to the master components (f_m) as follows:

$$f_m = G_{am}^T f_a \qquad \textit{Equation 4-14}$$

Knowing this, a point attached to a FEM (for instance a vertex of the embedded surface mesh that is attached to a FEM grid), gets its position and velocity as a weighted sum of the nearby nodal positions $\boldsymbol{x_j}$ as follows:

$$x_a = \sum_j w_j x_j, \quad \dot{x}_a = \sum_j w_j \dot{x}_j \qquad \textit{Equation 4-15}$$

Forces applied to each vertex (f_a) then propagate back to each node according to:

$$f_j = w_j f_a \qquad \textit{Equation 4-16}$$

4.4.2 Application of embedded surface mesh for the quadriceps muscle group

In this section, a model was designed to test the application of the mesh embedding technique on the lower limb FE muscle models with the objective of reducing the computational cost. The purpose of modelling the muscles as FE bodies is of course not limited to improving the outcomes that could have been achieved with multibody models but it has the more important goal of monitoring the stress/strain distribution inside the muscles. As a result, the scope of the

investigation that we are doing in this section shall not be limited to the kinematic outcomes of the model.

As a result, we have designed a model that uses the exact same setup of passive deep knee flexion simulation with FE quadriceps muscle as was described in section 4.3.1. However, we have considered the QT and RF FE models to be the most important parts that we want to monitor in terms of stress distribution. The other surrounding muscle (VI, VL, and VM) are the surrounding muscles of our main muscle and their stress distribution is not a priority. Therefore, to reduce the overall computational cost, we propose to replace these surrounding muscles with their corresponding surfaces embedded in a coarse FE grid. The defined objective for this preliminary study is to see how does this embedding technique impact the model outcomes both in terms of kinematics and predicted stress in the RF muscle.

A coarse FEM grid was generated for VI, VM, and VL muscles to embed their external surface mesh. An example of the embedded mesh in comparison to the normal FE mesh is depicted for the VI muscle in Figure 4-13. It is important to mention that the embedded surface mesh does not require a high level of treatment and simplification of the insertions sites. This significantly reduced the preparation time of the model.

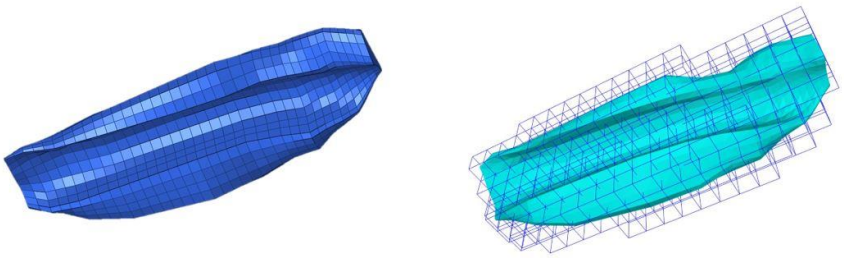

Figure 4-13, The image on the left is the Hexahedral dominant mesh with 1326 elements, generated for the VI muscle and used in the model explained in section 4.3.1. The image on the right is the polygonal surface mesh embedded in a coarse FE mesh composed of 324 voxel elements of maximum two-centimeter edges.

Figure 4-14 illustrates the case of a model having the RF and QT as finely meshed components and the other muscles represented as surfaces embedded in a coarse FE grid. Sliding is still modeled between all surfaces (bone or muscle) that may come into contact and the other details of the model setup, and material parameters are conserved to be identical to what was explained in section 4.3.1. Regarding the embedded parts, to account for the FEM voxels that are either empty or partially filled with the embedded surface mesh, the mass and the stiffness values of the embedding FEM are weighted based on the methods proposed by *Nesme et al*. to improve the resulting behavior of the model [156]. This technique is fully implemented in Artisynth [58].

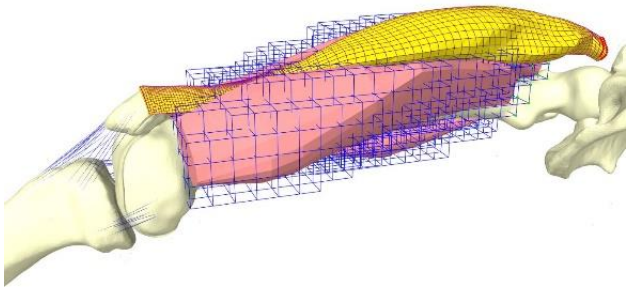

Figure 4-14, Generated combined FE-multibody model of the lower limb for simulation of passive deep knee flexion while considering the RF and QT as main FE components finely meshed (highlighted in yellow). The other muscles are modeled as surface meshes embedded in a FE grid. Contacts are defined between all muscles. The QT is connected to four muscles and to the patella.

The passive deep knee flexion is simulated using this model by imposing the motion of the tibiofemoral joint. As the quadriceps muscles are all connected to the QT that is attached to the patellar bone, changing the modelling technique of the quadriceps muscles will affect the kinematics of the patellofemoral joint that is free to react to the forces transmitted to it through soft tissues and contact forces.

4.4.3 Mesh embedding technique results and discussion

The model of the embedded surface mesh for VI, VL, and VM muscles were successful to simulate the whole deep knee flexion. The deformed model at various steps of the simulation is depicted in Figure 4-15 and compared to the finely-meshed FE model (section 4.3.1). Regarding the simulation time, the finely-meshed FE model took more than 8 hours to complete while the embedded model took about two hours and a half, despite that the Rectus Femoris and quadriceps tendon are still finely meshed. As previously mentioned, since all our modeled muscles are indirectly connected to the patella, the first comparison of the results between our two simulations was the comparison of the patellofemoral kinematics.

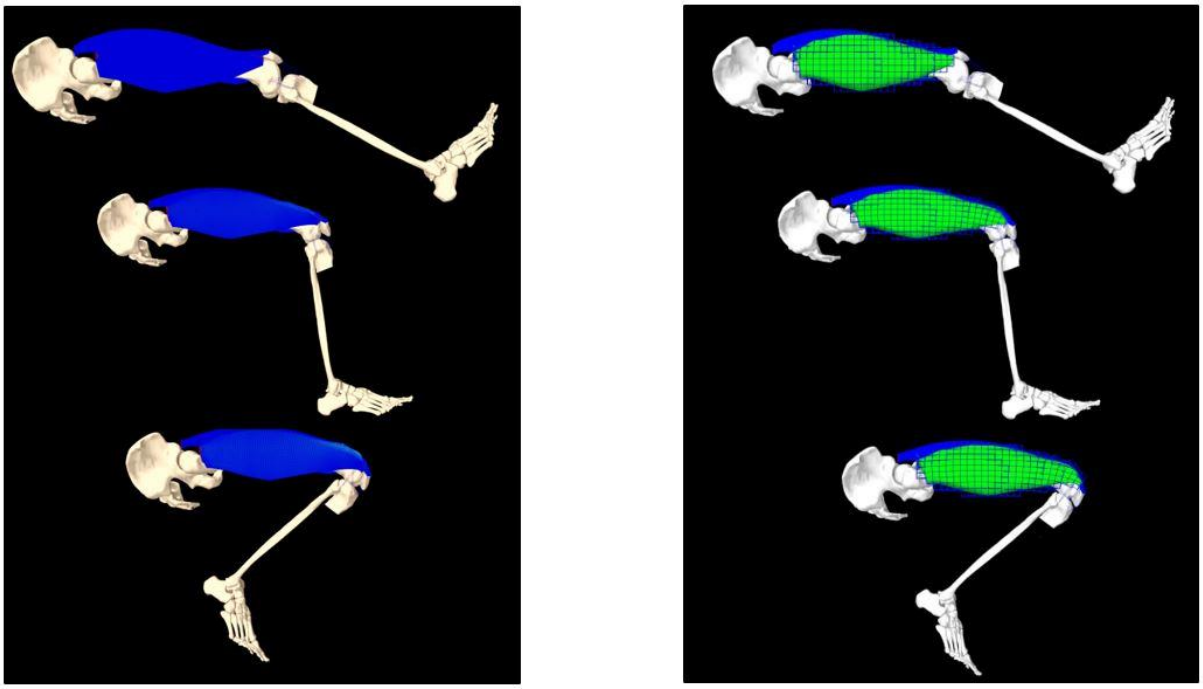

Figure 4-15, left: The deformed state of the finely-meshed FE model at various steps of passive knee flexion. Right: The deformed state of the model with embedded surrounding muscles at various flexion degrees.

The predicted patellofemoral kinematics are demonstrated in Figure 4-16 and compared with the outputs of the finely meshes FE model. The predicated kinematics using the mesh embedding technique has significantly reduced the preparation and computational time for the simulation. However, as the results are suggesting, the patellofemoral kinematic outcomes have not been compromised as the maximum differences observed in the curves are approximately one-millimeter differences in medial/lateral and rotational degrees of freedom.

To perform a preliminary investigation on the impact of changing the modelling technique of the VI, VL, and VM muscles on the predicted stress distribution of the RF muscle, we have monitored the maximum principal stress in the RF muscle throughout the simulation time. The result is presented in Figure 4-17. The RF maximum principal stress was not substantially impacted by changing the modelling technique despite the reduced computational time.

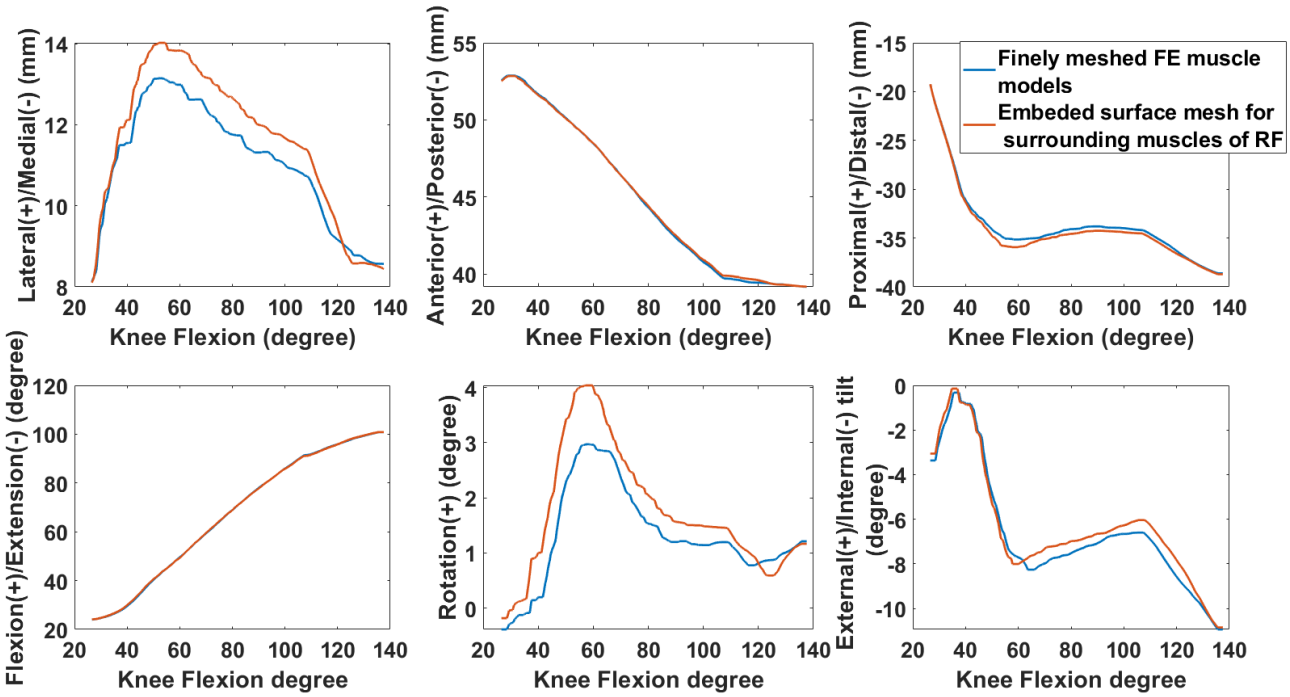

Figure 4-16, The effect of replacing the FE model of the VI, VL, and VM muscles with embedded surface meshes in a FEM grid on the patellofemoral kinematics.

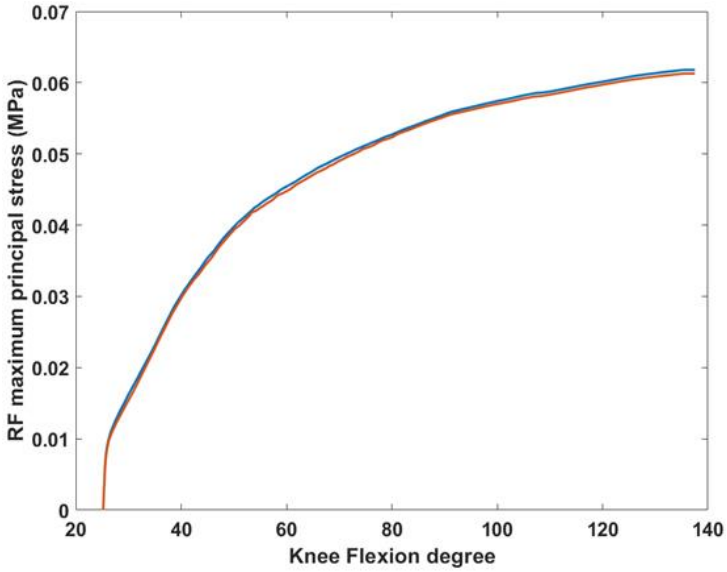

Figure 4-17, Maximum principal stress of the RF muscle that was considered as the main muscle throughout the passive deep knee flexion simulation with finely meshed FE models of the quadriceps muscle group and QT (blue line), and finely meshed RF and QT, but replacing the VI, VL, and VM muscles with surface meshes embedded in coarse FE grids with voxel elements (orange line).

In conclusion, in this section we evaluated mesh embedding to be used as a model reduction technique in the MS models of the lower limb that represent the muscles with FE components. The full and reduced lower limb models were used to simulate passive deep knee flexion and the kinematic outcomes were compared. The use of the mesh embedding technique was successful to reduce the computational cost of the simulation as well as model preparation time. The outcomes of the reduced model did not show a substantial difference from the full model.

4.5 Overall conclusion

The dataset of the subject collected in chapter 3 enabled us to present a modular model for simulating the passive deep knee flexion. Thus, a variety of modelling possibilities with different levels of complexity were demonstrated in this chapter as an implicit aim. In this sense, MS models

of the quadriceps muscle group were generated while representing the muscles by MT units or FE parts. A sensitivity analysis was performed on the model with MT parts that showed the importance of a proper choice of the optimal fiber length and the tendon length in MT models. A new technique to reduce the computational cost of FE muscle models in their environment was introduced and seems encouraging for future simulations.

The explicit aim of finding the modelling complexity level required for our study on the patellar trajectory after HTO was followed. The kinematic results obtained from different models were compared to the MRI-based data points to test the validity of the models. The MS model having a 3D FE representation of the quadriceps muscles was shown to predict the patellofemoral kinematics with higher accuracy. As a result, the model of the patellofemoral joint will be generated with this consideration in the next chapter in order to study the effect of OWHTO on this joint.

The foundations set in the previous chapters along with the conclusions made in the current chapter will be used in the next chapter to form an extensive study on the OWHTO.

5

Application on medial open-wedge high tibial osteotomy

As previously noted in the extensive review of the literature provided in chapter 2, the contact pressure distribution on the two compartments of the knee after HTO is correlated to the limb alignment obtained after correction. However, finding the exact amount of correction in each patient is a challenge as it is affected by deformity in all body planes as well as the condition of the soft tissues.

To overcome this challenge, the capabilities of biomechanical numerical simulations have been shown to be useful and generated a line of research on HTO. In that research line, the aim is to get the answer to the question of finding the optimal correction angle that balances the contact force in the two knee compartments or shifts the weight off of the damaged compartment. This question is either answered by providing a general rule applicable to various cases [127,129,157] or by proposing a patient-specific modelling method or protocol that finds the answer for a single patient [24,125,126]. In any case, based on our observations from clinical and cadaveric studies analyzed in chapter 2, these types of studies might be oversimplifying the problem in terms of the role of

the soft tissues. Because the preexisting soft tissue laxities and also the alteration made in the soft tissues after HTO can be different between patients and can substantially impact the results. This point is supported by the results of the multibody study performed by *Purevsuren et al*. that proves the effect of pre-existing laxity in MCL on contact force distribution after HTO [128].

Considering that various complications in OWHTO surgical outcomes such as MCL tightness and patellar descent are related to soft tissues, the potential of numerical simulations in addressing this aspect seems not to be used to its maximum. As a result, we sensed the need to address the soft tissue aspect of OWHTO. It is important to be mentioned that our aim is not to get an answer to the optimal alignment for a patient. But, it is to investigate and highlight the impact that modelling the alteration of the soft tissues after OWHTO can have on the results of the numerical simulations that are used for finding the optimal alignment. Thus, the healthy subject dataset collected in the previous chapters can be used in the framework of the analysis that we conduct in this chapter. Meanwhile, the provided insight about the soft tissue alteration after OWHTO can be beneficial for the clinicians making a decision about the OWHTO surgery even without the help of numerical simulations.

Based on the findings of the systematic review performed on the complications of medial OWHTO, there are two aspects of the surgical complications that need to be explored. Firstly, further insight is required about the role of MCL in achieving tibiofemoral contact balance. This understanding may affect the design of future studies both in medical and biomechanical fields. Secondly, the correlation between patellar descent and distalization of the patellar ligament insertion to tibia due to the opened wedge shall be further investigated.

Therefore, two main questions will be addressed in this chapter. Firstly, we want to investigate if the approach we take towards modelling the MCL and thus potential tightness of MCL after

OWHTO can noticeably impact the tibiofemoral contact stress distribution at a time frame during level walking. Secondly, we would like to see if the alteration made in the insertion of the patellar ligament after HTO results in changing the position of the patella and if it has an effect on the passive force of the quadriceps muscle group. To answer these questions, two different models have been developed so that the effects are studied in isolation without interfering with one another.

The first model is a model of the tibiofemoral joint at a time frame during level walking that corresponds to the knee flexion angle observed during our high-resolution MRI acquisition (to be explained in section 5.2). The subject knee model at 25° flexion is used as the base and virtual HTO is performed on the tibia to simulate various limb alignments. Different scenarios are hypothesized about the superficial bundle of MCL after HTO to study the impact of the tightness of MCL caused by wedge opening on the stress distribution on the two tibiofemoral compartments.

The second model is a non-weight-bearing model of the patellofemoral joint (to be explained in section 5.3) that is free to move and a fixed tibiofemoral joint. The idea is to perform HTO surgery with different opened wedge angles and to monitor the patellar position and the stress in the quadriceps muscle group while the subject is lying in the supine position. As a result, we will be able to see if larger wedge sizes result in patellar descent and if the stress distribution in the passive muscles is noticeably affected.

In the following sections of this chapter, the process of performing a virtual OWHTO cut and alignment change on the tibia will first be explained. Followed by that, we will continue with the methods, results, and discussion on each of the aforementioned studies on patellofemoral and tibiofemoral joints. Finally, the findings of both studies will be used to conclude the chapter.

5.1 Virtual OWHTO for model generation

Computer models with opened wedges on the tibia were developed from the dataset of the healthy subject explained in sections 3.1 and 3.2. The frontal plane of the tibia is defined based on its local coordinate system. An oblique cut was simulated on the tibia with a plane perpendicular to the frontal plane and passing through the lateral cortex 16 mm distal to the lateral tibial plateau and a medial cortex 37mm distal to the medial tibial plateau inspired from the literature [158,159]. This cut divided the tibia into proximal and distal parts that were added to our dataset used for generating the model in Artisynth.

To perform wedge opening, the hinge axis was defined to be perpendicular to the frontal plane and passing through the most lateral point on the OWHTO cut. Computer models with various angles of wedge opening were developed using a custom-made Java code in the Artisynth platform. This code takes the hinge axis and the opening degree as an input and rotates the distal part of the tibia around the hinge axis to achieve the desired alignment as depicted in Figure 5-1. In this process, all the connective tissue and muscle insertion points were defined as Frame Markers that were attached based on their location to either the distal or the proximal part of the tibia. As a result, the initial length and thus the tension of the ligaments and muscles attached to the distal part of the tibia are automatically modified by rotating the distal tibia to open a wedge. For simplification, the fibula is considered to be attached to the distal part of the tibia. Once the wedge is open (Figure 5-1), the distal and proximal parts of the tibia are reunited and attached to act as a single bony part.

The process is conducted for a 2.5°, 5.0°, 7.5°, and 10.0° wedge angles to create a total of five different limb alignments as depicted in Figure 5-2. The posterior tibial slope (PTS) was computed in all the five cases through measuring the angle between the sagittal proximal tibial joint

orientation axis and a line perpendicular to the anatomical axis of the tibia. The PTS was checked to remain constant before and after wedge opening to make sure that the hinge axis is defined correctly. This constant PTS was about 9° that is in the normal range of PTS (10° ± 3.5°) [59].

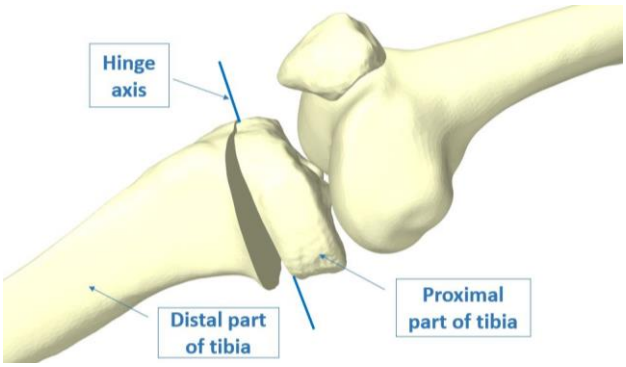

Figure 5-1, The virtual wedge opening on the model through cutting the tibia into a proximal and a distal part and rotating the distal part around the defined hinge axis.

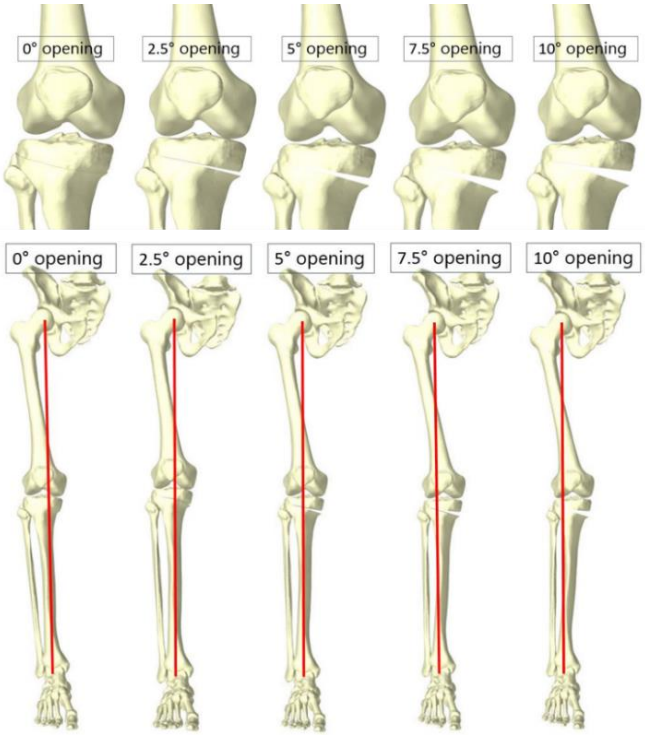

Figure 5-2, Simulated wedge opening angles. Top: close view of the tibia after different wedge openings. Bottom: limb alignment after different wedge openings. The red line shows the weight-bearing line.

5.2 The role of MCL tightness on tibiofemoral contact forces at various wedge opening degrees

As the first objective of this chapter, we would like to investigate if the alteration in MCL tension in response to various wedge openings can impact the tibiofemoral contact stress distribution during level walking.

5.2.1 Model generation

The bone geometries obtained in the previous section after wedge opening along with the native knee bone and soft tissue geometries were used to build models of the lower limb with 0°, 2.5°, 5°, 7.5°, 10° opened wedge degrees. To avoid the impact of the patellofemoral joint on the simulation results, the patellofemoral joint was decided to be excluded. Therefore, the generated model only contains the tibiofemoral joint with its articular and connective tissues (Figure 5-3).

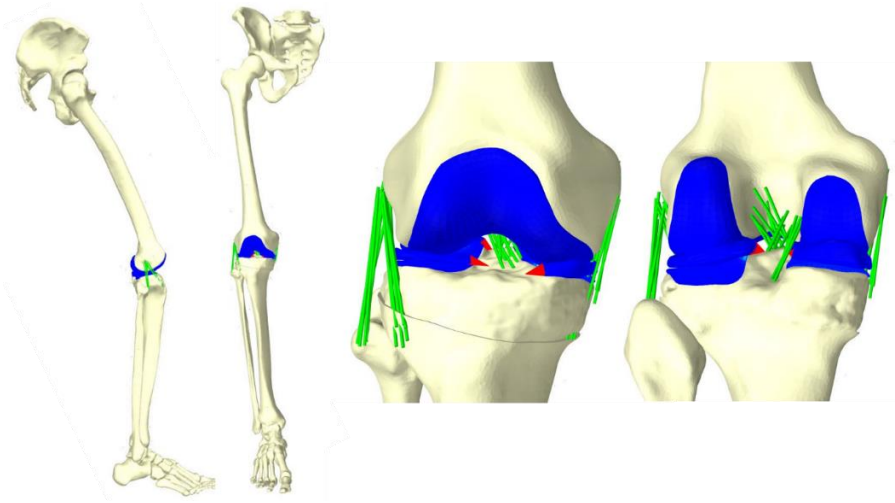

Figure 5-3, The model of the tibiofemoral joint used to investigate the effect of MCL tightness after wedge opening

This includes the medial and lateral tibial cartilages, the femoral cartilage, and the medial and lateral meniscus, all modeled with FE components. The anterior and posterior cruciate ligaments,

medial and lateral collateral ligaments, and anterolateral ligaments were all defined similar to the previous chapter. The meniscal horns were represented with multiple linear springs.

The mesh generation process for the articular tissues was conducted in Hypermesh 2019 software. In order to mesh the cartilage parts with hexahedral dominant elements, the surfaces of the bone parts corresponding to the cartilage area were meshed with 4-node shell elements (and a small number of 3-node elements). Followed by that, this mesh was projected to the outer surface of the segmented cartilage. This resulted in two shell meshes having a variable distance that represents the thickness of the cartilage at each point. The linear solid mesh tool in Hypermesh was used to generate a hexahedral dominant mesh of the cartilage with a limited number of wedge elements that correctly respect the cartilage thickness. This process was repeated for the tibial and the femoral cartilages; the corresponding meshed parts are depicted in Figure 5-4. This resulted in the formation of 1106 elements for the femoral cartilage, 419 elements for the lateral cartilage, and 471 elements for the medial cartilage, that all had a single layer of element with approximate 2mm maximum edge size. The medial and lateral meniscus were respectively meshed with 10506 and 3354 hexahedral elements of maximum 1mm edge size. These meshes were produced using the solid map mesh method in Hypermesh.

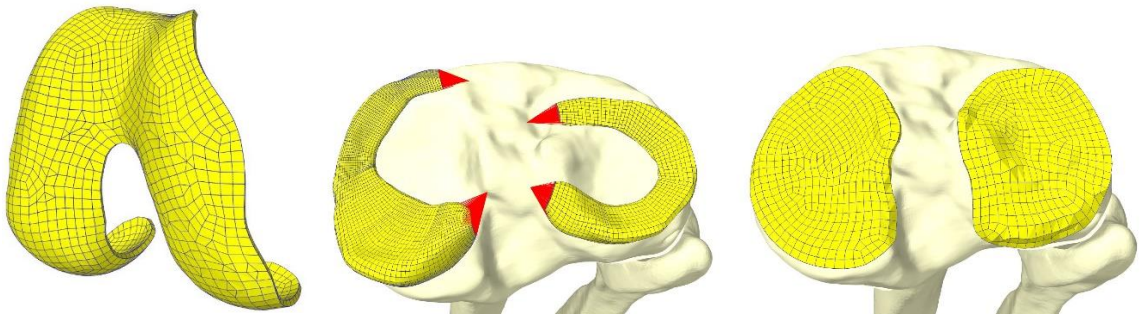

Figure 5-4, The generated hexahedral dominant mesh for articular surfaces. Left: femoral cartilage. Middle: menisci and the horns represented by springs (in red). Right: tibial cartilages.

5.2.2 Material properties

Ligament bundles were modeled with multiple strands that had non-linear stiffening spring behavior at low strains and had a linear stiffness at higher strains [140]. The stiffness of each bundle was divided between the strands as they were acting in parallel. The reference lengths of the ligament bundles were defined to be their length at full extension. The Anterior Cruciate Ligament (ACL) and Posterior Cruciate Ligament (PCL) were each formed of two anterolateral and posteromedial bundles (aACL, pACL, aPCL, pPCL). The Medial Collateral Ligament (MCL) was composed of a deep and a superficial layer. The superficial MCL had an anterior (aMCL), posterior (pMCL) and inferior (iMCL) bundle. The deep layer of the MCL had an anterior bundle (aDMCL) as well as a posterior bundle (pDMCL). The Lateral Collateral Ligament (LCL) and the knee Antero-Lateral Ligament (ALL) were each formed of a single bundle. We used the definition of the bundles and their properties defined in the literature [141,142,160], but the number of strands in each bundle was chosen based on the area of their attachment sites. The bundle properties as well as the number of strands used to represent each bundle is presented in Table 5-1.

Table 5-1: The ligament parameters [142,160] *and number of springs per bundle*

Ligament bundle	**Stiffness**	**Reference strain**	**Number of springs**	**Ligament bundle**	**Stiffness**	**Reference strain**	**Number of springs**
aACL	1500 N	0.02	4	**aMCL**	2500 N	0.02	1
pACL	1600 N	0.01	4	**iMCL**	3000 N	0.04	1
aPCL	2600 N	-0.23	4	**pMCL**	2500 N	0.02	1
pPCL	1900 N	0.02	4	**aDMCL**	2000 N	-0.08	2
LCL	2000 N	0.02	7	**pDMCL**	4500 N	0.03	2
ALL	41.9 N/mm	0.0	7				

The Artisynth combined FE-multibody platform allows defining the bones as rigid bodies, similar to what is done in a multibody simulation. Since we were not interested in the bone deformation, we have modeled all the bones as rigid bodies same as all other simulations in this thesis. The viscoelastic behavior of cartilage and menisci was not considered as the viscoelastic time constants (~1500 s [123]) are much larger than the elapsed loading time during gait. Therefore, the femoral cartilage and the medial and lateral tibial cartilages were modeled with isotropic linear elastic material having Young's modulus of 15MPa and a Poisson ratio of 0.45 similar to what was previously used for an HTO study in the literature [127].

The menisci were modeled with a transversely isotropic linear elastic material having Young's modulus of 20 MPa and the Poisson ratio of 0.2 in the radial and axial directions [25,123,161] and Young's modulus of 120 MPa and the Poisson ratio of 0.3 in the circumferential direction [25,127]. To assign the primary material direction circumferentially, a custom-made code was generated to define the material direction as an element vector field (as depicted in Figure 5-5).

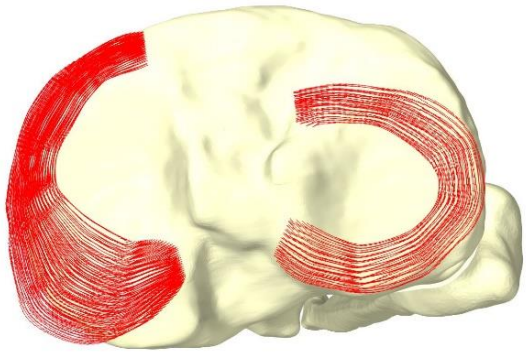

Figure 5-5, The material direction defined for the menisci illustrated with red-colored vectors.

Assuming that the material directions of a number of control points are defined on the surface of the meniscus, we should implement a code to be able to assign these directions to the elements without causing discrete changes in the neighboring element directions. As a result, a method was

created in the model that takes a set of reference points assigned with their reference directions as an input and creates array lists from them. Then, for each of the elements of the FE body, this method finds the center of the element and uses the Delaunay interpolation to calculate the direction of the element based on the neighboring reference points. This includes first finding the four closest points and forming a tetrahedron out of them. Then the method checks whether the centroid is inside or outside the tetrahedron. If it is outside, the method deletes the 4th node, takes only the three closest ones, and computes the weights based on the Delaunay triangulation query coded in the Artisynth platform. The computed weights are used to scale and add the material directions given for the reference points. The material direction is then assigned to the element as Equation 5-1 denotes. w_i is the weight dedicated to ith closest reference point.

$$Element\ Material\ Direction = \sum w_i\ (Reference\ Direction)_i \qquad \textit{Equation 5-2}$$

To simulate the meniscal horn attachments, linear springs were used with no pre-strain (strain existing in the spring at its reference length). A combined spring stiffness of 350 Nmm^{-1} was used for each horn [162]. The springs were attached to the top surface of the tibia as shown in red in the image on the middle of Figure 5-4.

5.2.3 Load and boundary conditions

Subject-specific loading data were obtained from gait analysis performed in the CHU Lyon-Sud gait laboratory with an eight-camera motion analysis system (Optitrack, NaturalPoint, OR, USA) and one floor-mounted force-platform (dimensions 0.5m x 0.4m, Advanced Mechanical Technology, Inc., Watertown, MA, US). The subject performed five walking trials at a self-selected speed in a 10 m long walking lane from the same start position. First, model-based kinematics was obtained by Multibody kinematics optimization in Matlab software by our

collaborator Raphaël Dumas in the Laboratoire de Biomécanique et Mécanique des Chocs [163]. Inverse dynamic analysis was used to calculate the body forces at each time frame. Further details and a complete description of the inverse dynamics analysis are provided in chapter 6.

The generated models are at 25° knee flexion which was the knee position during the acquisition of the high-resolution MRI. The knee flexion angle of the subject during a gait cycle was plotted to find the time frame that corresponds to the 25° knee flexion angle of the model (Figure 5-6).

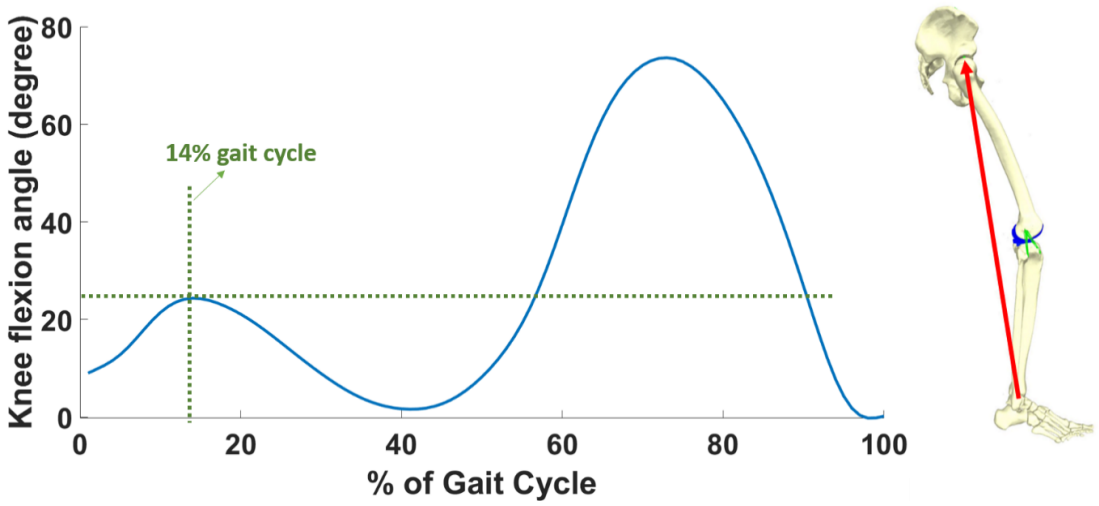

Figure 5-6, Knee flexion angle of the subject throughout a gait cycle. At 14% gait cycle the subject's knee flexion angle is 25°. The force along the mechanical axis of the limb is calculated at this angle.

The subject's knee flexion angle at 14% gait cycle was the closest to this value. Thus, the force applied to the limb along the weight-bearing line at this time frame was computed to be 667 N and was applied to the model at the ankle. The direction of the load vector was adjusted for the different models based on the alteration of the weight-bearing line after wedge opening (visible in Figure 5-2). Regarding the boundary conditions, the femur was fixed and the tibia was free to move in all its translational and rotational degrees of freedom as long as the knee maintained the 25° flexion

angle. The knee joint movement was only constrained by the ligaments and tibiofemoral joint contact.

Another important aspect of the loading condition concerns the superficial bundle of MCL (sMCL). To investigate the importance of providing a realistic model of the sMCL in biomechanical models that address OWHTO alignment problem, we have tested three different approaches towards it. Following the wedge opening, the superficial bundles of MCL are modelled in three different ways that are depicted in Figure 5-7. In the first case, the insertion points of the sMCL to the tibia are assumed to be attached to the distal part of the tibia (which is the case if the sMCL is not released during surgery). As a result, their length and tension differ by wedge opening. In the second case, these bundles are assumed to be attached to the proximal part of the tibia and thus are not affected by wedge opening (which is the case if their adaptation is neglected in biomechanical models). In the third case, the sMCL bundles are removed after wedge opening representing the surgical resection of these bundles. The impact of each of these scenarios about MCL is monitored on the tibial cartilage to see if it can alter the contact pressure balance during an activity such as walking. On the lateral side of the knee, the LCL and ALL are always attached to the distal part of the tibia.

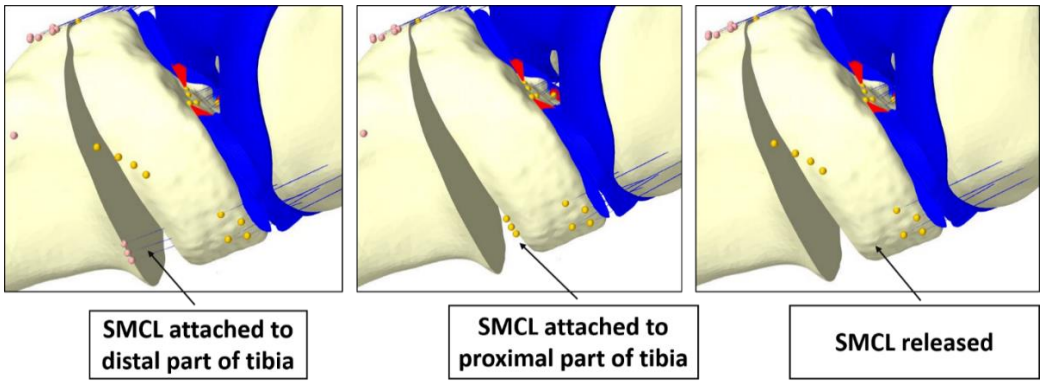

Figure 5-7, The sMCL treated in three different ways after virtual OWHTO surgery to study its effect on tibiofemoral contact pressure balance.

5.2.4 Outcomes measures

The distribution of von Mises stress on the medial and lateral tibial cartilages was monitored for each simulation. Additionally, we have computed the total normal contact force on the medial and lateral cartilages defined as the sum of the contact forces at the nodes in contact and projected along the long axis of the tibia as defined by *Grood et al*. [138]. The contact forces of the two compartments were also normalized based on the sum of the medial and lateral contact forces to show the relative contact force balance between them.

5.2.5 Results

The von Mises stress distribution on the medial and lateral tibial cartilages in HTO models with various approaches towards sMCL and different wedge openings are presented in Figure 5-8 to Figure 5-10. Opening the wedge while the sMCL was attached to the distal part of the tibia resulted in substantially increasing the stress on the medial cartilage. On the other hand, in the models with the sMCL attached to the proximal part of the tibia, the lateral stress following wedge opening was substantially higher than the knee without wedge opening. The increase of lateral stress was higher with larger openings. Meanwhile, as we expected, changing the insertion of the sMCL from the distal part of the tibia to its proximal part does not affect the stress results of the knee without wedge opening that is visible when comparing the left top images in Figure 5-8 with Figure 5-9.

Releasing the sMCL instantly reduced the medial cartilage von Mises stress at all opening angles compared to the models where the sMCL was conserved (attached to the distal or proximal tibia). The lateral cartilage in the models with sMCL released experienced slightly higher stresses compared to the models with sMCL conserved and the stress values were noticeably higher than the case where sMCL was attached to the distal tibia.

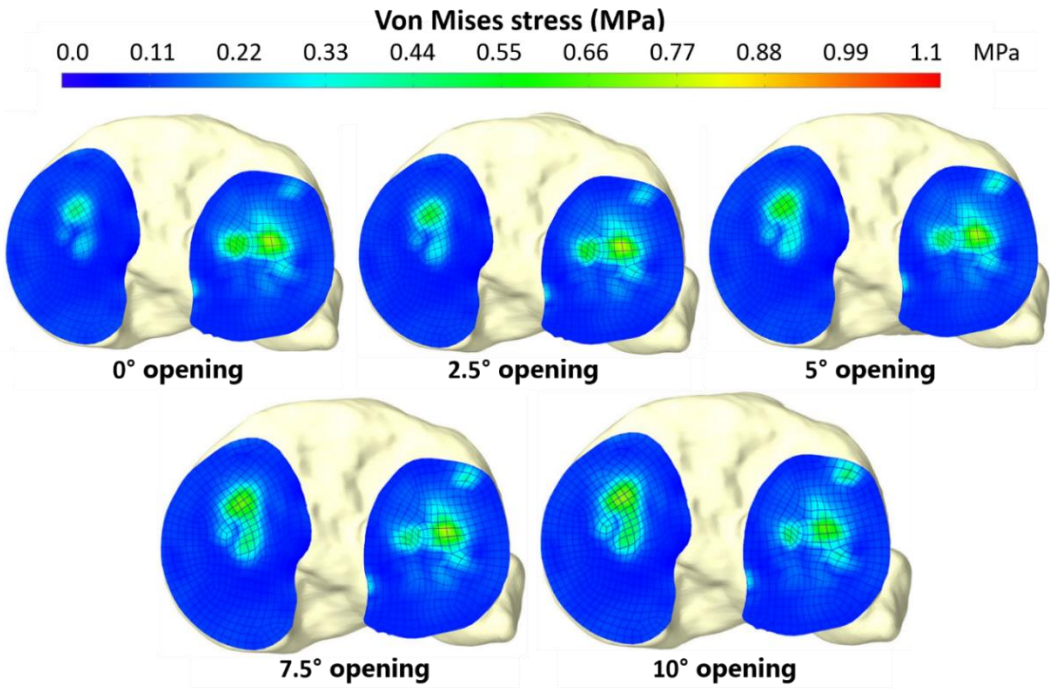

Figure 5-8, Von Mises stress distribution on the medial and lateral tibial cartilage at different HTO wedge openings while the sMCL is attached to the distal part of the tibia.

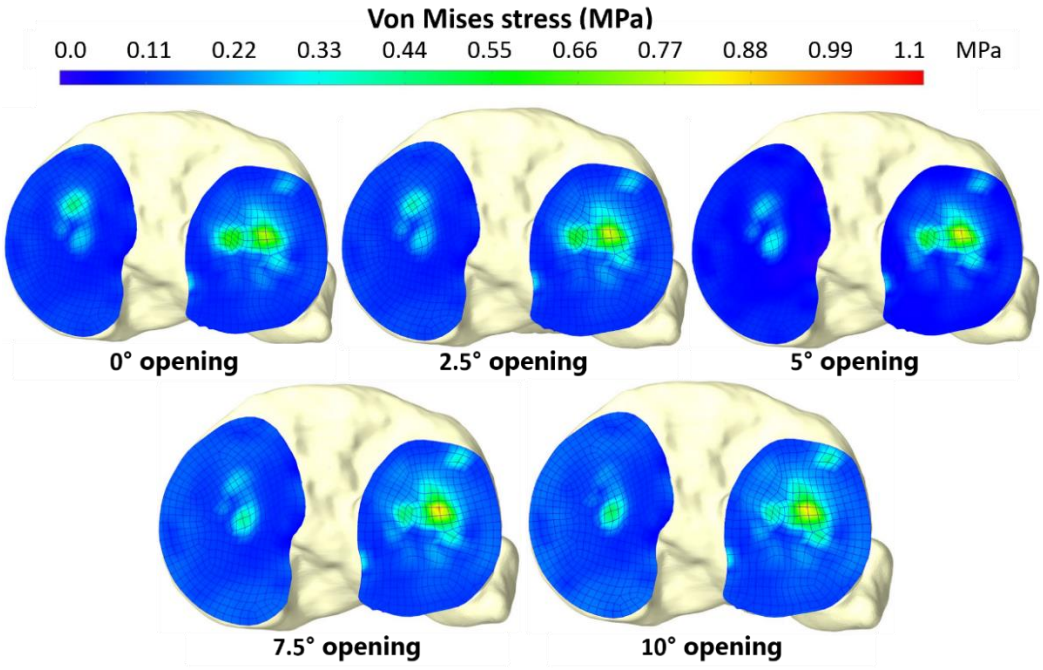

Figure 5-9, Von Mises stress distribution on the medial and lateral tibial cartilage at different HTO wedge openings while the sMCL is attached to the proximal part of the tibia.

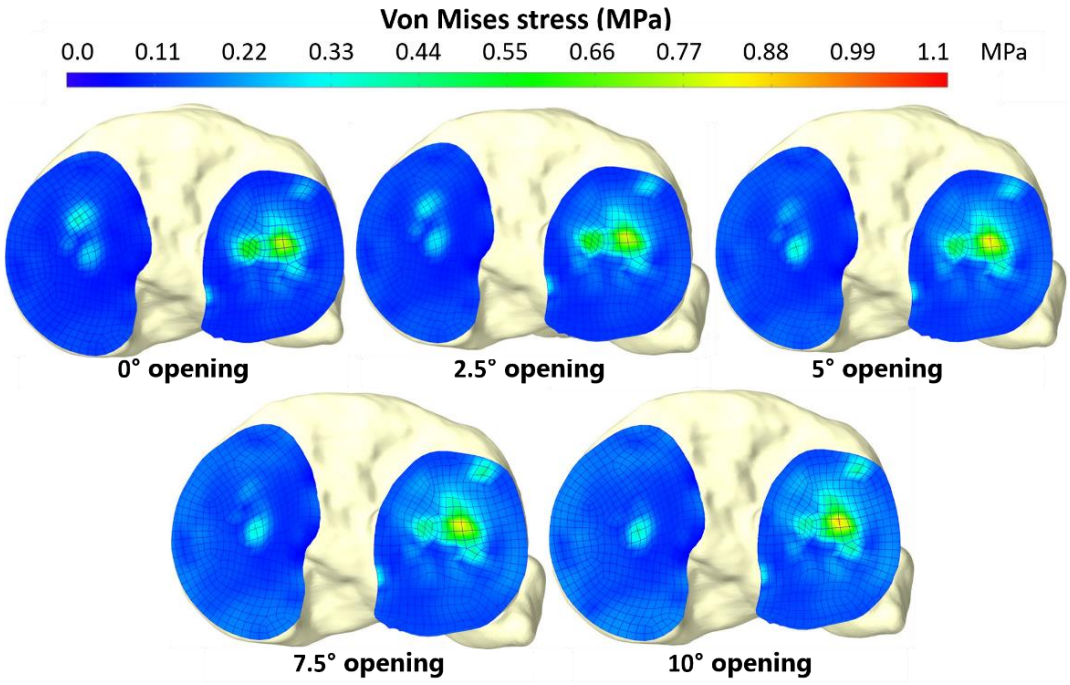

Figure 5-10, Von Mises stress distribution on the medial and lateral tibial cartilage at different HTO wedge openings while the sMCL is released.

The results regarding the total contact forces of the medial and lateral cartilages are presented in Figure 5-11. As depicted in this figure, in the model with the sMCL attached to the distal part of the tibia, the excessed tension produced in the ligament due to wedge opening is resulting in increasing the total contact force of the medial side and decreasing the total contact force of the lateral side, which is exactly the opposite to the objective of wedge opening. This trend is improved in the model with sMCL attached to the proximal side in multiple opening degrees although the overall trend is not stable. Release of the sMCL seems to be improving the trend and achieving the objective of reducing the medial contact force and shifting the force to the lateral side.

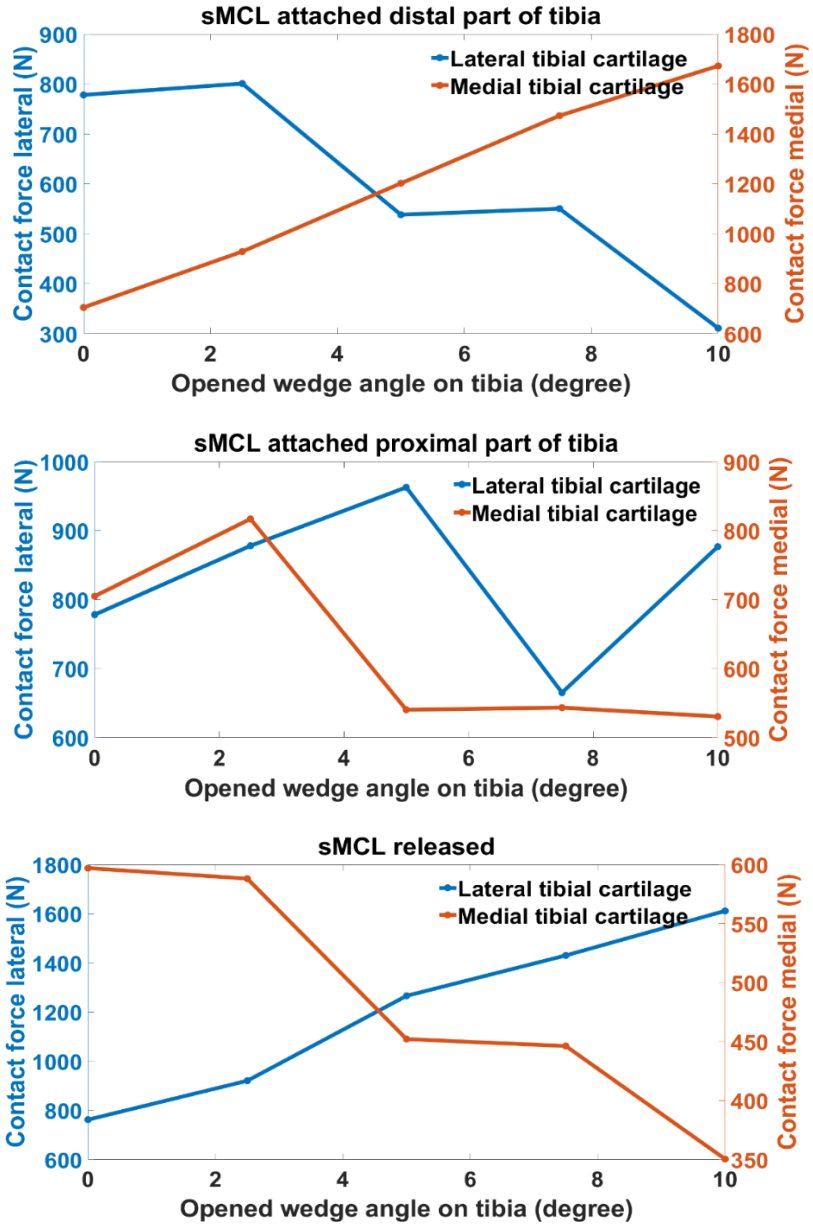

Figure 5-11, The total normal contact force on (blue) lateral and (red) medial tibial cartilages at different HTO wedge openings with (top) sMCL attached to distal part of tibia, (middle) sMCL attached to proximal tibia and (bottom) sMCL released.

To better observe the shift of the contact force between the medial and lateral compartments, we have plotted the relative contact force in the medial and lateral tibial cartilages in Figure 5-12. The balance of the contact forces changes when taking different approaches towards modelling the sMCL while wedge opening. The medial cartilage is getting an increasingly larger share of the

contact force when the sMCL is attached to the distal tibia. However, releasing the sMCL immediately reduces the share of the medial side and shifts the force laterally. Opening larger wedges on the tibia while the sMCL is released was the most successful to increase the share of the lateral side from the total contact force.

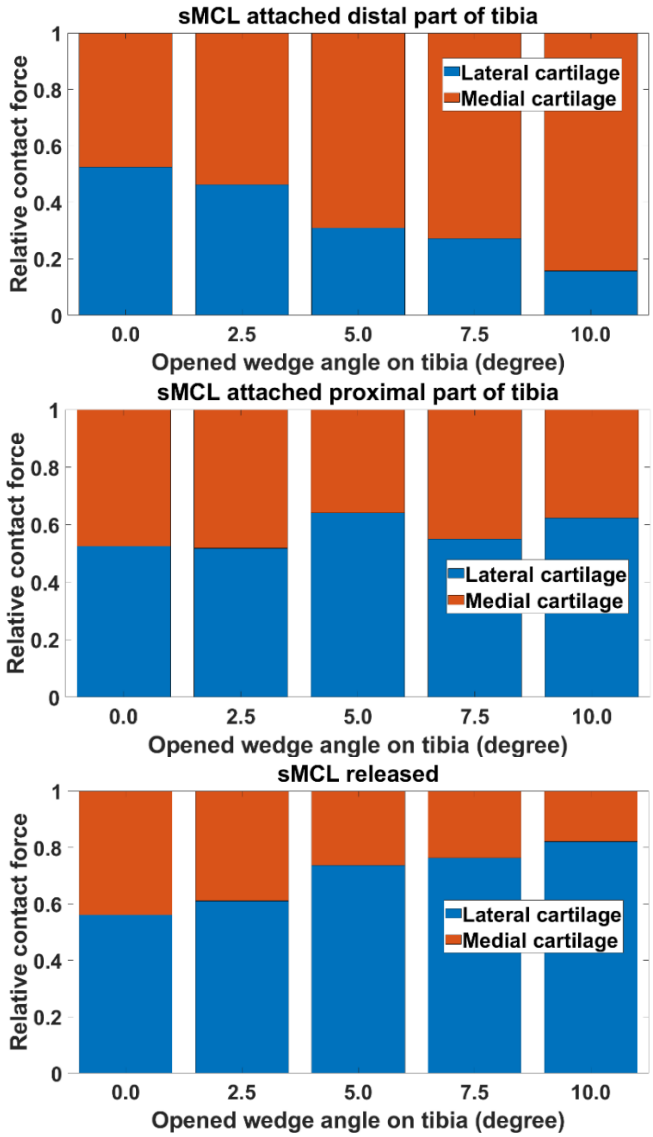

Figure 5-12, Relative contact force on the (blue) lateral and (red) medial tibial cartilages.

5.2.6 Discussion

The objective of this part of the manuscript was to highlight the importance of taking a realistic modelling approach towards the sMCL in numerical simulations that are developed for assisting OWHTO. Additionally, the conducted investigation provides insight into the extent to which the sMCL can affect the tibiofemoral contact balance which can be beneficial for clinicians as well. This was motivated by the fact that various cadaveric studies had shown that performing an OWHTO without any release of the MCL increases the MCL strain and pressure in the medial compartment and decreases the pressure on the lateral compartment [94,98,99]. In this sense, we tried three different approaches towards modelling the MCL after wedge opening to see if our biomechanical simulations can reproduce these observations. In the first case, the sMCL was attached lower than the HTO cut (length and tension affected by wedge opening) that is the case if this ligament bundle is maintained during surgery. In the second case, the sMCL was attached above the HTO cut (length and tension not affected by wedge opening) that is similar to what has been previously used by the numerical simulations in the literature. In the third case, the sMCL was removed which is equivalent to the surgical resection of this ligament bundle.

Looking at the relative contact force between medial and lateral compartments, it is evident that when the sMCL is attached lower than HTO cut it is experiencing more and more tightness due to larger wedge openings, the share of the medial compartment from contact force is significantly increasing. This means that the objective of HTO surgery could not be achieved and the situation is deteriorating with larger openings due to sMCL tightness. Of course, this conclusion is only relevant when the MCL does not have any preoperative laxity. However, if the sMCL was attached above the HTO cut, the situation would have been very different and the share of the medial compartment from contact force was significantly less. Thus if a numerical simulation that is

aiming to find the optimal alignment for a patient takes this assumption, the final decision on the opening angles required for the patient may be affected. In this sense, it seems critical to specify and account for the insertion of the sMCL bundles relative to the HTO cut if the surgeon does not intend to release the sMCL. However, this effect is neglected by many biomechanical studies that are aimed to take simulation-based decisions on the optimal correction that balances the contact force in knee compartments [125,127]. In addition, the authors have faced a lack of data and many contradictory reports in the clinical literature in this regard.

The results of the model with sMCL attached lower than HTO cut (distal part of the tibia in HTO models) is indeed in accordance with the observation of excessive medial pressure in cadaveric studies when the sMCL is not released [94,98,99].

Surgical release of the sMCL (complete or partial) at the tibial attachment is a very common practice during OWHTO [94,164]. Our results demonstrated that releasing the sMCL immediately reduced the von Mises stress and total contact force of the medial side at all opening degrees while the lateral side experienced the highest stress values among the three models. This point accords with the observation made by various cadaveric studies that the release of the superficial bundle results in a decrease in the contact area and pressures on the medial compartment and in an increase in these parameters on the lateral compartment [94,98,99].

The observation of lower medial contact forces is in complete accordance with the trends witnessed in the study performed by *Kuriyama et al*. [129]. In their study, they have used a musculoskeletal model to find the ideal coronal alignment under dynamic conditions. They tested the release of MCL by making the MCL function inactive in their multibody model but had the deep layer function of the medial joint stabilizer active. This can be seen as equivalent to the release for sMCL in our model while the deep MCL is conserved.

Looking at the relative contact force between medial and lateral compartments in our results (Figure 5-12), it is evident that opening larger wedges on the tibia while the sMCL is released was the most successful to increase the share of the lateral side from the total contact force. This is consistent with the general consensus that releasing the superficial bundle of the MCL during OWHTO helps with shifting the weight to the lateral compartment [94]. This can of course change in presence of initial ligament laxity or medial ligamentary instability as the conditions may vary and MCL release should be avoided in that case [94,96,98,128].

In a recent clinical study by *Bagherifard et al*. [164], it is indicated that the medial pressure increased in the majority of their studied cases following OWHTO without sMCL release. Whereas, the factors affecting this increase were not thoroughly identified and sMCL release was mentioned to be the "wiser option" until the identification of the factors. Our study highlighted the importance of clarifying the insertion site of sMCL with respect to HTO cut and could be potentially contributing to the identification of the sources of increased pressure when not releasing the sMCL during HTO.

The study performed in this part of the manuscript also has some inherent limitations. Firstly, as the generated knee model was at 25° flexion, the model results could not be directly compared to the experimental studies available in the literature as the knee was mostly at full extension in these studies. Secondly, the material parameters and reference strain of the ligament bundles were estimated from the literature and we did not have the means to tune these properties for the subject. Finally, the 3D representation of the ligaments was not included to facilitate modelling the tension and length variations after wedge opening and account for the modifications that were required in the superficial bundle of MCL. Regarding the perspectives of the study, it is beyond expectation that potentially some alteration due to wedge opening is made in the length and moment arms of

the Sartorius, Gracilis, and Semitendinosus muscles as they are inserted beneath the OWHTO cut. These alterations can also play a role in the contact force balance between the tibiofemoral compartments and can be addressed in future studies. In addition, to extend the models developed for making simulation-based clinical decisions to assist the OWHTO surgery on a patient-specific basis, the material models used for the cartilages can be improved to more complex models such as fibril-reinforced poro(visco)elastic models [31,53]. This improvement opens new perspectives as it is beneficial for the investigation of fluid flow and fluid pressure that are important indicators in presence of osteoarthritis as in patients that are subject to OWHTO.

5.3 Investigation of the patellofemoral joint after HTO

The findings of the extensive review of the literature performed in chapter 2 demonstrated that OWHTO could alter the trajectory of the patella. In the majority of the analyzed clinical and cadaveric papers, the patellar height was found to be significantly decreasing after surgery based on the Blackburne-Peel ratio. However, we observed that various methods were used to report the patellar height. Some of them could have been criticized not to be the best representatives of the patellar height after HTO while others were new methods that had not been widely used. A limited number of studies monitored the modification of the patellar tilt, mostly observing a decrease. Regarding patellar shift, only one study found a significant increase compared to the pre-operative situation.

However, from a biomechanical perspective, it is clear that the tibial insertion site of the patellar ligament is moved distally during OWHTO, proportionally to the opened wedge degree. This distalization could be linked to the observation of the change in patellar tracking after OWHTO in the studies mentioned in chapter 2. As a result, we were motivated to further analyze the impact of OWHTO on the position of the patella through numerical simulations and to find the answer to

the patellar tracking alteration without being sensitive to the clinical measuring methods. The results can provide better insight into the effect of HTO on the patella and thus may be beneficial to the clinicians since it can highlight the need to adjust the parameters measured in clinical or cadaveric studies. Additionally, the results can affect the decision of surgeons in practice on using other surgical techniques such as biplanar osteotomy that avoid patellar alteration.

Therefore, the objective of this section is to investigate the effect of the modification of patellar ligament insertion (due to wedge opening) on the position of the patella in its all six degrees of freedom (DOFs). As the patellar position is controlled by the balance of the force between soft tissues connected to it, we were also interested to see if the modified patellar position can have a noticeable impact on the muscular stress distribution in a passive state (that can be expanded to conclude about the muscle passive force). The muscles attached to the patella were therefore modeled, VL, VM, VI, and RF. The results of this investigation may be beneficial in the design of the musculoskeletal models that study gait modification after OWHTO.

5.3.1 Model generation

The model was built using the geometries from the subject's dataset described in chapter 3. To conserve all the articular tissue details, the state of the knee model is the same as the subject's knee position collected during the high-resolution MRI exam. The custom-made Java code was used to generate models with 0°, 2.5°, 5°, 7.5°, 10° opened wedge degrees. To perfectly isolate the effect of distalization of the patellar ligament insertion on the patellar position and the muscles attached to the patella, the tibiofemoral joint was fixed to conserve the 25° knee flexion angle. As a result, to avoid unnecessary computations, the FE components that are only active inside the tibiofemoral joint (i.e. the medial and lateral tibial cartilages and the menisci) were excluded from the model.

The objective is to define a fixed tibiofemoral joint and a model of the patellofemoral joint that is free to move while the subject is lying in the supine position as depicted in Figure 5-13.

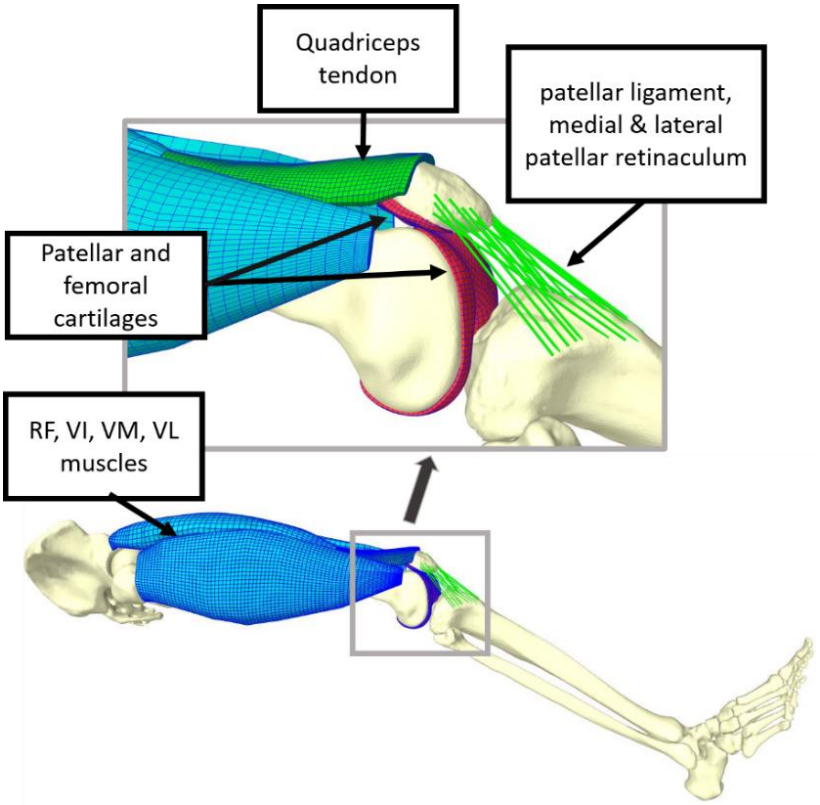

Figure 5-13, The model of the patellofemoral joint used for investigating the effect of HTO on patellar position and muscle stress distribution.

The included FE components were the patellar cartilage, the femoral cartilage, the QT as well as the RF, VI, VM, and VL muscles, all finely meshed with hexahedral dominant elements. Similar to chapter 4, for the mesh generation process, the maximum element size was approximately 6mm for the muscle parts that resulted in a total of 2100 elements for RF, 1326 for VI, 9290 for VL, and 2308 for VM. For the QT, the approximate maximum element size was 3mm that resulted in the formation of 5200 elements. The mesh generation process for the femoral and patellar cartilages was similar to what is described in section 5.2.1 and was conducted in Hypermesh 2019. This

resulted in the formation of 1106 elements for the femoral cartilage having a single layer of element and 969 elements for the patellar cartilage with two layers of element.

Again similar to the passive deep knee flexion simulation in the previous chapter, bundles were defined based on the segmented geometries to represent the patellar ligament, as well as the medial and lateral patellar retinacula. The patellar ligament was represented with a total of seven bundles consisting of three bundles for the central region and two bundles for each of the medial and lateral regions based on the results of the cadaveric study of *Yanke et al*. [143]. Five bundles were defined to represent each of the medial and lateral patellar retinacula.

5.3.2 Material parameters

Patellar ligament bundles were modeled similar to what is explained in section 4.2. Thus, the nominal stiffness values for the patellar ligament bundles were adapted from the literature [143]. The total stiffness of the central region (composed of three bundles) was set to $278\ N/mm^2$. The total stiffness of medial and lateral regions (each composed of two bundles) were set to $201\ N/mm^2$ and $173\ N/mm^2$ respectively. The nominal reference strain was assumed to be 0.02 for all the bundles of the patellar ligament at full extension. As the knee position in the model is corresponding to a 25° knee flexion, the ligament strain alteration was accounted from full extension for all ligaments.

Five bundles were defined to represent each of the medial and lateral patellar retinacula with the respective total stiffness of $31\ N/mm^2$ and $97\ N/mm^2$ taken from the literature [144,145] while assuming a 0.01 reference strain.

For the femoral and patellar cartilages, a linear elastic material was used having Young's modulus of 15MPa and a Poisson ratio of 0.45 similar to what was previously proposed for a study on HTO in the literature [127]. The passive muscles were modeled with a nearly incompressible

isotropic neo-Hookean hyperelastic material and the parameters used for the muscles were $c_1 = 11.7\ kPa$ *and* $D_1 = 16.3\ MPa^{-1}$ and were defined based on the findings of *Affagard et al*. who identified the behavior of the thigh muscles based on a displacement field obtained from ultrasound and digital image correlation techniques [155]. For the quadriceps tendon, a linear elastic material was used with a value of 30 MPa for Young's modulus and 0.46 for the Poisson ratio that was chosen for the model after testing multiple values estimated based on the literature [165].

5.3.3 Loading and boundary conditions

The femur and tibia were fixed to isolate the effect of wedge opening on the patellofemoral joint. The patella was left free to react to the forces transmitted to it through the soft tissues and the contact forces. As this simulation is assuming a non-weight-bearing knee while the subject is lying in the supine position, the inertial parameters of the patella and of the FE muscles were neglected.

The attachment of the patellar ligament to the tibia is inserted in the distal part of the tibia when performing the virtual OWHTO. Therefore, the length and thus the tension in the nonlinear springs forming its bundles are changed due to wedge opening. The reference length of the bundles (the length at which the springs experience the reference strain) is set to be their length at full extension in the native knee. A 0.02 pre-strain is also imposed along the axial direction of the QT FE component.

5.3.4 Outcome measures

The various wedge opening angles performed on the tibia can result in alteration of the patellar position. This effect was tested on the model while conserving the state of the tibiofemoral joint in its initial state (knee flexion angle 25°) through fully constraining the tibia and the femur.

Predicted medial/lateral patellar shift, proximal/distal translation, and patellar tilt and rotation are monitored in different models to quantify the effect of wedge opening angles on the patellofemoral joint. To see the impact on the stress distribution in the passive muscles, von Mises stress distribution and maximum principal stress were monitored on the Rectus Femoris muscle since it is supposed to be the main muscle that is connected to the patella.

5.3.5 Results

The simulation results showed that after wedge opening the forces acting on the patella through the soft tissues were affected and thus the patella achieved a new balance position in each case. This balance position is quantified and compared between different models generated for different wedge opening angles. The results of the modifications observed in the patellar translations and rotations due to various simulated wedge openings are depicted in Figure 5-14. In this figure, each DOF of the patella is analyzed separately and plotted against the wedge opening angle. As depicted, all the analyzed translational and rotational patellar DOFs were affected by wedge opening (with patellar translations and rotations that can respectively reach 5mm and 4°). The larger wedge openings result in distalization of the patella, shifting the patella laterally, rotating the patella, and tilting it internally (in other words medially).

Following the observation of the stress distribution in the muscles, we noticed that the largest impact was visible in the Rectus Femoris (RF) muscle. The von Mises stress distribution in passive RF after OWHTO with various wedge openings is demonstrated in Figure 5-15. The maximum von Mises stress increased from 7.5 kPa for the native knee to 9.1 kPa for the model simulating a 10° wedge opening on the tibia. In addition, having larger wedge sizes noticeably increased maximum principal stress in passive RF as plotted in Figure 5-16.

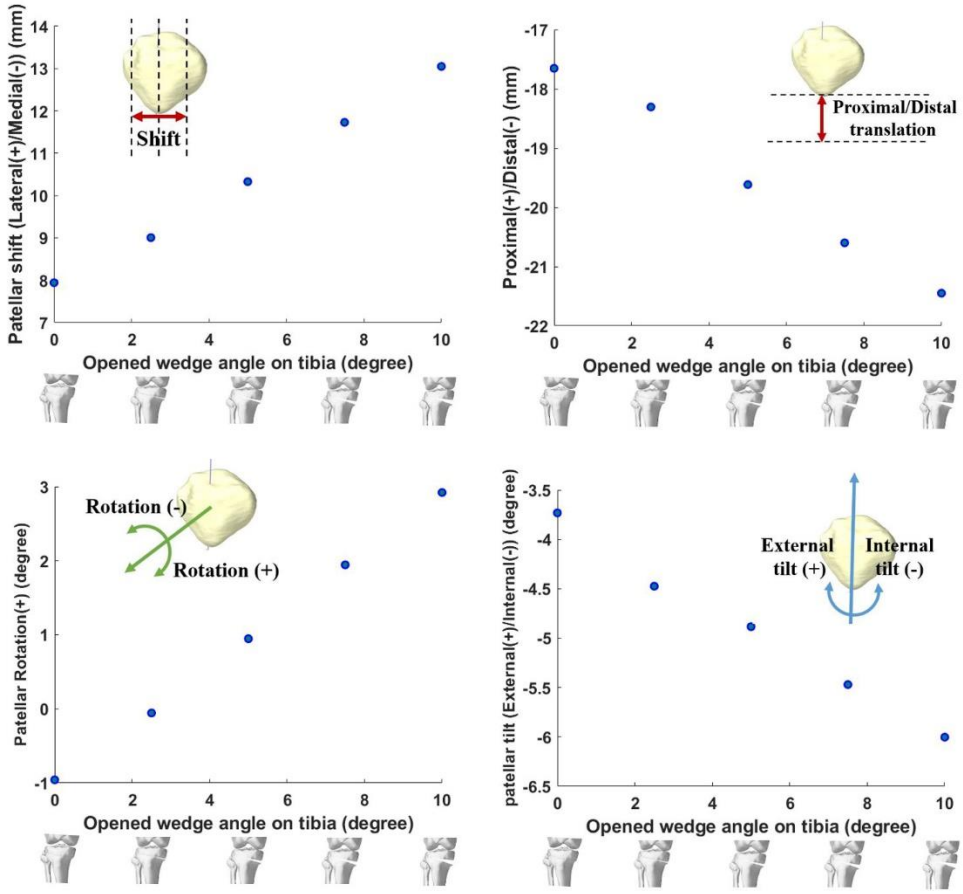

Figure 5-14, Predicted patellar position in response to different wedge opening angles on the tibia. The tibiofemoral joint is fixed at 25° knee flexion. The horizontal axis shows the wedge opening degree while the vertical axis is the state of the patella in its different DOFs defined based on ISB standards [138].

5.3.6 Discussion

The OWHTO not only has an effect on the tibiofemoral joint but also can alter the trajectory of the patella and impact the patellofemoral joint. The patellar ligament insertion on the tibia is located distal to the OWHTO cut, thus the length and tension of the patellar ligament in the model are changing with different wedge opening angles. This can modify the balance of forces on the patella and alter the tracking of the patella. Our aim was to observe if this impact is high enough to get noticed on the position of the patella and on the passive muscular stress distribution. To

study this, we monitored the rotations and translations of the patella predicted by the models generated after wedge opening. Our observations showed that larger wedge openings result in distalization of the patella, shifting it laterally, rotating it, and tilting it internally (medially).

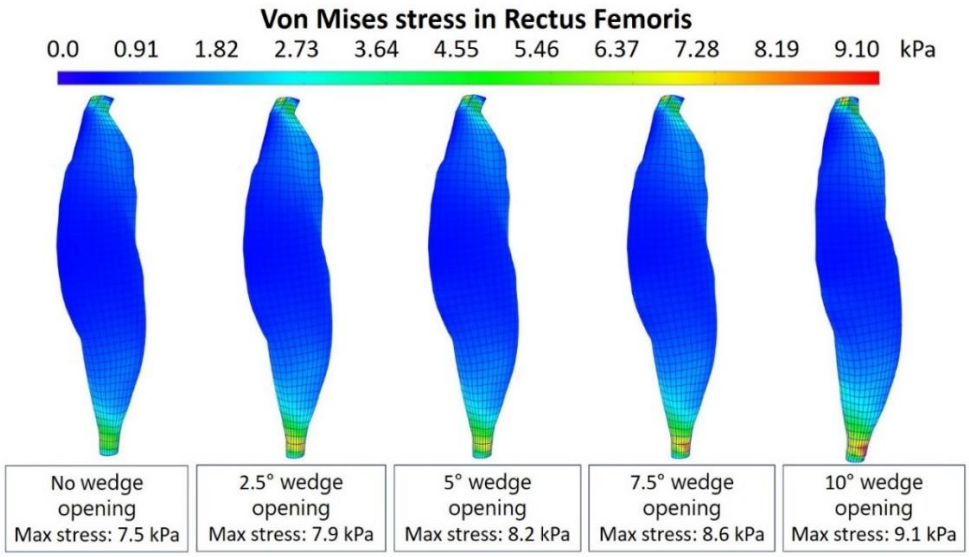

Figure 5-15, Von Mises stress distribution in the Rectus Femoris muscle in response to different wedge opening angles on the tibia.

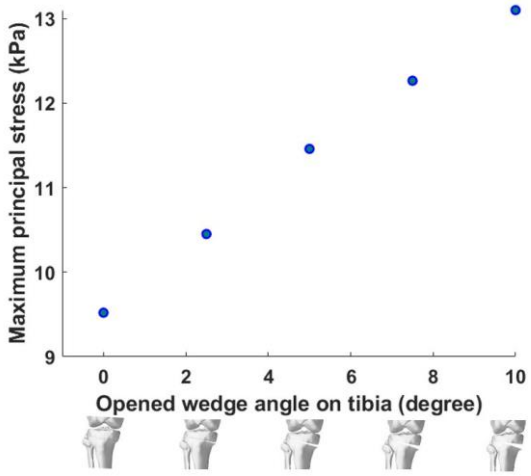

Figure 5-16, Rectus Femoris maximum principal stress alteration in response to different wedge opening angles on the tibia

Although the methodologies for evaluating the change in patellar height are different among clinical studies, the qualitative conclusion in this regard is consistent with the literature [85,116,166,167]. Our findings showed that at 25° knee flexion our subject could experience a 3.8 mm post-operative decrease in proximal translation for a 10° wedge opening on the tibia that is equivalent to a 21.5% decrease from the pre-operative value. This is consistent with the observation of an MRI-based study [85] that found a 14.2% decrease at 30° of flexion among their subject group with various correction angles.

Regarding the alteration of patellar tilt, our results showed a maximum internal (or medial) tilt of 2.3° happening for a 10° wedge opening on the tibia results. This finding is again consistent with the major alterations found in the literature reporting significant decreases of lateral patellar tilt between 1.8° and 2.2° [114,119,135] or a significant increase of medial patellar tilt of 2.2° with MRI based method [85]. And finally for the patellar shift, although the findings of the clinical papers had not been able to observe a significant change (Table 2-3), our observation was similar to the MRI-based study to experience a lateral shift but we observed a larger magnitude [85].

To our knowledge, the correlation between the opened wedge size on the tibia and the patella trajectory has not been studied in the literature. As the literature review performed in chapter 2 clarified, the studies on patellar position monitored the patellar tracking alteration on a group of patients undergoing HTO without providing information about their pre-operative bone deformation level or the wedge angles used for the surgery. As a result, the findings of our study have the advantage of showing the correlation between wedge size and patellar position and of highlighting the need for reporting the wedge opening angle in future studies. In addition, it gets the advantage of looking at the kinematics of the patella in various DOFs that are not measured with standard radiographs. But at the same time, the lack of available data in the literature acts as

an obstacle along the way to make an exact quantitative comparison between the results of our modelling with existing clinical studies. The main reason is that the only indications of correction amount in clinical studies on the same topic were the standing hip–knee–ankle (HKA) or Weight-bearing Axis (WBA) achieved after OWHTO. In that case, the opened wedge size or degree was not reported. In our study, the model was defined on a native knee with a very small varus deformation (thus without any requirement for an HTO surgery). Therefore, WBA and HKA are probably not good representatives of the wedge opening angle, especially when addressing the modifications of the soft tissues.

It is true that the exact clinical effect of alteration in patellar position is still unclear on patellofemoral pain despite the fact that symptoms of association with patellofemoral pain have been observed with patellar lateral shift [168]. While our study was a static analysis, we could observe an increase in the stress distribution (Maximum principal stress and von Mises stress) in the passive Rectus Femoris muscle. This observation highlights the fact that the studies on HTO should go beyond simply changing the varus-valgus alignment of the limb, especially when looking at gait modification.

Meanwhile, we should acknowledge some of the inherent limitations of the study performed in this section. The first limitation is indeed the simplifications that were made at the distal insertion of the quadriceps muscle group to the patella and not modelling further stabilization structures connected to the patella. Additionally, the aponeurosis was not modelled and the impact of the thigh muscles that were absent in the model was neglected. However, these simplifications are similar to the model generated in chapter 4 with FE muscles and the model was validated through comparison with the MRI based data points.

5.4 Overall conclusion

The first objective of this chapter was to investigate if the approach taken towards modelling the MCL can affect the predicted tibiofemoral contact stress distribution after wedge opening. Three different scenarios were studied. In the first one, the length and tension of sMCL were altered when opening a wedge (based on the wedge size). In the second scenario, we assumed that the sMCL is not modified after wedge opening (which is the assumption in many biomechanical simulations of HTO). Finally, in the third scenario, the sMCL bundles were removed that represented their surgical resection during the surgery. The results revealed that the stress distribution and contact forces predicted in these three cases are substantially different. Thus, a clear approach as concerns the way sMCL is modeled for OWHTO seems critical to be able to make simulation-based decisions on the optimal alignment correction. Additionally, our results successfully demonstrated that releasing the sMCL immediately reduced the stress amounts and contact force of the medial side at any opening degree. Such a release thus helps with better achieving the goals of the surgery in the absence of preoperative medial laxity.

Concerning the second objective of the chapter, our MS model successfully demonstrated that opening a wedge during HTO can alter the trajectory of the patella in rotational and translational degrees of freedom. Our observations showed that larger wedge openings result in distalization of the patella, shifting it laterally, rotating it, and tilting it internally (medially). Our provided data showed the correlation between the opened wedge size on the tibia and the patella trajectory, which had not been previously studied in the literature. Additionally, an increase in the stress distribution was observed in the passive Rectus Femoris muscle. This observation suggests that studies on HTO should go beyond simply changing the external forces to truly simulate the effects of this surgery.

6

Combined FE-multibody musculoskeletal lower limb model, application to gait

In this chapter, we present a developing collaborative work towards the application of our combined FE-multibody model with MT parts for a simulation of gait. This preliminary work is motivated to evaluate the consistency of joint modelling in the inverse multibody MS models with the forward-based models with deformable and detailed joints.

6.1 Introduction

Musculoskeletal (MS) models with multibody approaches provide the opportunity to use the kinematic and kinetic data obtained from a subject during activity and recorded with a Motion Capture system, to estimate muscle forces and joint contact forces. However, it is not sufficient to directly investigate the mechanics of the joint tissues. In this context, Finite Element (FE) models are used to help with the estimation of tissue response in terms of stress and strain.

One way to go from kinematic and kinetic data of a subject during an activity all the way to the tissue response using computer modelling is the combination of FE and MS models. Progress in

this sense has been made through multiscale modelling workflows where usually MS models are generated in one platform and then the corresponding results are exported to a FE modelling package [53,55,169].

Studies have shown that the inclusion of deformable joints can substantially impact the estimation of muscle forces [43]. Thus, one limitation of the sequential approach is that the tissue deformation and parameters of the joint level FE model cannot influence the results of muscle recruitment problem solved with the multibody model. Meanwhile, the sequential approach is widely applied [48–54], as it has advantages such as facilitating the use of advanced muscle recruitment algorithms and avoiding the high computational cost of a fully FE approach.

The multibody models used in sequential approaches normally feature simplified joints (such as a hinge mechanism for the knee) that is inconsistent with the FE deformable joint level models having the connective tissues and contact between the bones. Nevertheless, the subsequent FE simulations are mainly solved quasi statically while the primary kinematics of the joint are prescribed to obtain the secondary kinematics [53]. However, it is not clear how the forward simulation would react in a dynamic simulation and if the primary kinematics were not imposed. Furthermore, it has not been investigated if using more advanced knee mechanisms in the inverse kinematics and dynamics steps of the workflow will help with acquiring better results with the forward simulation.

The modelling platform used for this study (Artisynth), provides the opportunity to generate a model that combines the multibody and FE techniques in the same platform. Although this platform is not designed for gait simulation, we have tried to take a primary step towards using the modelling possibilities in this platform for gait simulation that could open new perspectives for combined inverse and forward modelling techniques.

The aim of this section is to make an attempt to explore the consistency of joint modelling between inverse multibody MS models and forward-based deformable models. This will indeed provide further insight into the use of the sequential approach in dynamic situations. To achieve this goal, we have collaborated with Raphaël Dumas in Laboratoire de Biomécanique et Mécanique des Chocs to use our combined FE-multibody model with MT parts and contact in the joint for gait simulation. The idea is to test the predictions made with inverse multibody MS models having the same personalized description of the muscular geometry but different kinematic knee models on a forward simulation in Artisynth with deformable knee joint. This can provide insight into the necessary consistency between inverse multibody MS models and forward-based models with deformable joints.

6.2 Musculoskeletal model generation in Artisynth

A personalized musculoskeletal model of the full lower limb was generated using the subject's dataset formed in chapter 0 as depicted in Figure 6-1. For each of the segmented 3d geometries corresponding to a muscle-tendon part, we defined the insertion site to the bones and the via-points required to represent the muscle line of action. Five body segments were defined based on the literature [170] including the pelvic, thigh, patella, shank, and foot segments. The muscle insertions/via-points were each attached to their corresponding segment as provided in Table 6-1.

Wrapping around the femur surface was activated for the muscles of the quadriceps group (RF, VL, VI, VM) using the novel method proposed by *Lloyd et al*. for computing wrapping paths across arbitrary surfaces that are implemented in Artisynth [57]. For simplification reasons, the via-points defined for the muscles were not adapted throughout the model's range of motion.

Figure 6-1, The full lower limb musculoskeletal model generated from the subject. The pink lines represent the muscle-tendon units and the green lines represent the ligament bundles.

Similar to what was defined in the previous chapters for the tibiofemoral and patellofemoral joints, axial springs having nonlinear elastic properties were defined to represent each ligament bundle, which means that the bundle's tension is a function of its length L [140]. In the musculoskeletal model of the lower limb, we included the patellar ligament, medial and lateral patellar retinacula, anterior and posterior cruciate ligaments, medial and lateral collateral ligaments and the knee anterolateral ligament. The definition of the bundles and the properties are similar to what explained in sections 5.2.2 and 5.3.2.

*Table 6-1, The list of MT parts included in the model and the corresponding body segments on which the muscles have an insertion or a via-point. If multiple insertions/via-points are placed on one segment, the number is indicated by *(number).*

Muscle name	Attached segments				
Gastrocnemius Medial Head	Foot	Shank		Thigh	
Gastrocnemius Lateral Head	Foot	Shank		Thigh	
Soleus	Foot	Shank			
Tibialis Posterior	Foot*2	Shank*2			
Tibialis Anterior	Foot*2	Shank*3			
Peroneus Brevis	Foot	Shank*3			
Peroneus Longus	Foot*3	Shank*4			
Peroneus Tertius	Foot	Shank*2			
Extensor Digitorum Longus	Foot*4	Shank*3			
Extensor Hallucis Longus	Foot*4	Shank*3			
Flexor Digitorum Longus	Foot*5	Shank*2			
Flexor Hallucis Longus	Foot*6	Shank*2			
Tensor Fasciae Latae		Shank		Thigh*2	Pelvis
Gracillis		Shank*2			Pelvis
Semimembranosus		Shank			Pelvis
Semitendinus		Shank*2			Pelvis
Biceps Femoris Long Head		Shank			Pelvis
Sartorius		Shank*3		Thigh	Pelvis
Biceps Femoris Short Head		Shank		Thigh	
Vastus Medialis			Patella	Thigh*3	
Vastus Intermedialis			Patella	Thigh*2	
Vastus Lateralis			Patella	Thigh*3	
Rectus Femoris			Patella	Thigh*2	Pelvis
Gluteus Maximus I, II and III				Thigh*2	Pelvis*2
Gluteus Medius I, II and III				Thigh	Pelvis
Gluteus Minimus I, II and III				Thigh	Pelvis
Adductor Longus				Thigh	Pelvis
Adductor Brevis				Thigh	Pelvis
Adductor Magnus I, II and III				Thigh	Pelvis
Pectineus				Thigh	Pelvis
Illiacus				Thigh	Pelvis*3
Psoas				Thigh	Pelvis*3
Quadratus Femoris				Thigh	Pelvis
Gemellus				Thigh	Pelvis
Piriformis				Thigh	Pelvis

6.2.1 Evaluation of the moment arms of the MT part

To evaluate the moment arms of the muscle-tendon parts of the musculoskeletal model depicted in Figure 6-1 around the knee flexion axis, we have simulated a passive knee flexion having the exact same setup as what was described in chapter 4 (sections 4.1 and 4.1.1). The motion of the tibiofemoral joint was fully prescribed throughout the simulation based on the MRI data points available from the knee at different flexion angles while the hip and ankle joints were considered to be solid. However, as previously mentioned, the patella is in contact with the femur surface and is totally free to act in response to the forces transferred to it through the tendons, ligaments, and contact forces. The femur medial-lateral axis (about which the flexion angle is computed) is defined based on standardization of the International Society of Biomechanics (ISB) [171].

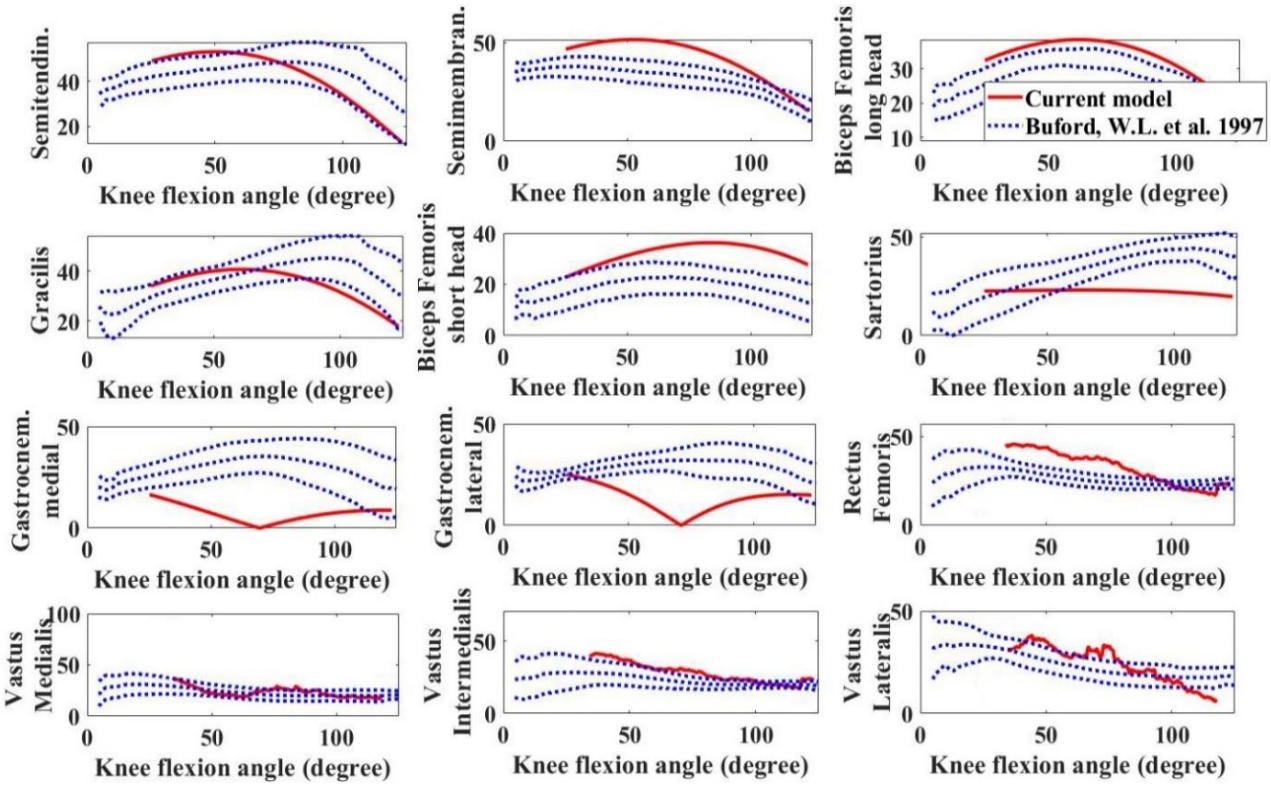

Figure 6-2, The effective moment arm of selective muscles in the musculoskeletal model

The effective Moment Arm (MA) value of each muscle around the femur medial-lateral axis, was computed through a custom-made Matlab script (Mathworks, Natick, MA, USA) based on the methods proposed in the literature [172,173] presented in Equation 6-1.

$$effective\ MA = -\frac{dl/_{dt}}{d\theta/_{dt}} = -\frac{dl}{d\theta}, \qquad \text{Equation 6-1}$$

where $dl/_{dt}$ denotes the derivative of muscle-tendon part length with respect to time and $d\theta/_{dt}$ denotes the derivative of knee flexion angle (θ) with respect to time.

To compare the moment arms of the muscles generated in our model with the experimental cadaveric study of Buford, *W. L. et al*. [172], we have plotted the computed moment arms against knee flexion angle in Figure 6-2. The results show that the predicted moment arms for the muscles provide acceptable results for the majority of the muscles. However, the moment arms of the Gastrocnemius medial head and lateral head would need to be improved through defining a wrapping surface or moving the via-points for predefined flexion ranges. This decision was not taken into account in the current study for simplification reasons.

6.2.2 Exporting the generated model to other platforms

The muscle insertion points, muscle-tendon unit via-points, and ligament bundle insertion points are defined as frame markers in the Artisynth model. By definition, a frame marker is a massless point attached to a frame or a rigid body. As a result, each of the ligament or muscle insertions or via-points are attached to a body segment and are fixed with respect to it.

The skin markers placed on the subject during motion capture can be used to define the body segments and the local coordinate frame of each body segment [170]. We made the assumption that the local coordinate frames that we define on the bones based on the bony landmarks are the same as the ones that will be generated from the skin markers positioned on the subject during gait

analysis, with the consideration that the axes directions we used are defined based on the ISB standardization. So the X axis is anterior, Y axis is superior, and Z axis is lateral (to the right) [171]. As previously mentioned, these local coordinate frames are necessary for the definition of the Joint Coordinate System (JCS) to report joint kinematics [138].

The same segment frames can be used for defining the muscle insertions and via-points to make them independent of the global coordinate frame. As a result, to export the model of our subject from Artisynth to be used in the Matlab inverse model generation process, it was needed to extract the coordinates of all frame markers in their corresponding segment frames.

A custom-made code was generated to transform the coordinates of any frame marker to its corresponding segment frame. Following that, another custom-made code was generated to go over the list of the defined muscles and report the first and last insertion point or via-point of the muscle (if existing) corresponding to each segment. Then the data is saved in the required format to be used for inverse model generation in Matlab. These custom-made codes provide the opportunity to recreate the exact same muscular geometry in other modelling platforms as long as the standards used for segment frame definition are compatible.

6.3 Development of an inverse model of the subject in Matlab

The bone geometry of the subject along with the insertion/via-points of the muscles and insertion points of the ligaments defined in the local frame of their corresponding body segment was provided for our collaborator Raphaël Dumas in Laboratoire de Biomécanique et Mécanique des Chocs. This data was used to recreate the musculoskeletal model of our subject in the validated inverse modelling package developed in Matlab [163].

The inverse kinematic model was generated with the following specifications: 1) The hip joint was considered to be a spherical joint. 2) The foot was considered as a single rigid segment.

However, the ankle joint was defined using an MRI-based morphological fitting methodology personalizing the definition of the tibiotalar and the subtalar joint axes [174]. 3) The patellofemoral joint was modeled as a hinge joint between the patella and the femur and the axis was adjusted by performing a surface fit to the patellofemoral contact area at full extension [175]. The patellar tendon (PT) was defined while having the same attachment points as the Artisynth model at full extension but was considered to be rigid similar to what was used by *Delp et al*. [176]. 4) The knee mechanism featured prescribed contact points as a function of flexion angle (these points are defined so that they respect personalized sphere-on-plane constraints and minimize all ligament length variations during motion) [177–179]. The medial and lateral spheres and planes were fitted on the articular surfaces (condyles and plateaus). The ligaments used at this step were the lateral collateral ligament, medial collateral ligament, anterior cruciate ligament, and posterior cruciate ligament all composed of multiple bundles similar to the Artisynth model. As we had the objective of testing the importance of compatibility of the inverse kinematic model used for the knee with the knee model used in the forward simulation, a hinge mechanism for the knee joint was also tested to build a second case for the inverse model. The hinge axis is defined as passing through the fitted spheres. It is important to note that this hinge axis is not aligned with the femur medial-lateral axis and not passing through the knee joint center (midpoint between the medial and lateral femoral epicondyles. This results in coupled rotations and translations when estimated using the Joint Coordinate System (JCS).

6.3.1 Application of the inverse model to gait

As previously mentioned in Chapter 3 (section 3.4), gait analysis was performed on the same subject of which we obtained the imaging data. The analysis was conducted in the CHU Lyon-Sud gait laboratory equipped with a motion analysis system and one floor-mounted force-platform in

order to simultaneously measure the kinematics and the kinetics of the subject during gait. The skin markers during this acquisition were used to define the five lower limb segments. Multibody kinematics optimization (MKO) method with the constraints specified in the previous section (hinge or sphere-on-plane with ligament for the knee) was used to compensate for the soft tissue artifact and obtain model-based kinematics during gait.

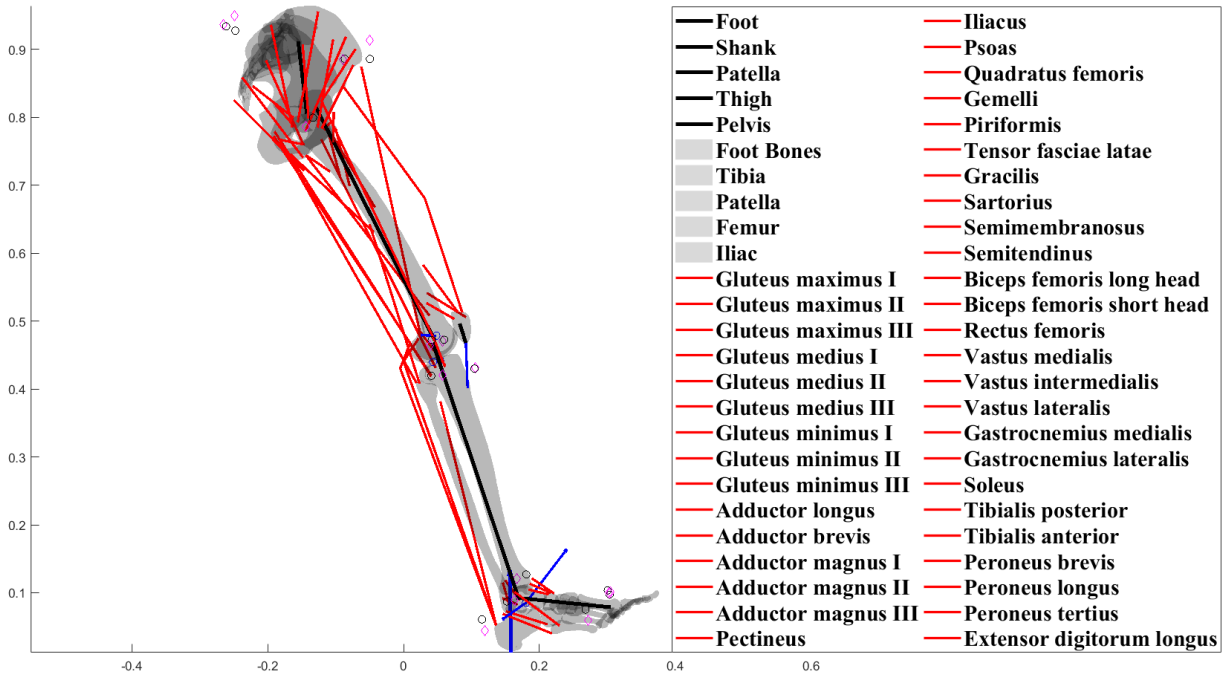

Figure 6-3 The inverse model generated from our model data in the Matlab modelling package. The model in the image is positioned at the beginning of the stance phase (heel contact). The position of the segments is obtained from skin marker positions through multibody kinematics optimization. Modeled and measured skin markers position is depicted in magenta diamonds and black circles, respectively.

The inverse model generated in the Matlab package located in the initial time frame of the stance phase (heel contact) is depicted in Figure 6-3. As a sample of the obtained kinematics from the model during gait, the tibiofemoral and patellofemoral joint kinematics using different knee mechanisms are provided in Figure 6-4 and Figure 6-5. For the computation of the translations, the origin of the femur and shank local frames (defined based on ISB standards) were both defined

to be placed midpoint between the medial and lateral femoral epicondyles at neutral position (considered to be the bone positions while taking the CT scan). The origin of the patellar frame was positioned at its most distal point. As the hinge axis is based on the condyle sphere centers, the tibiofemoral and joint kinematics with both knee mechanisms have similarities. The main differences appear for the medial-lateral and anterior-posterior translations and internal-external rotation while adduction-adduction is shifted. The impact on the patellofemoral joint kinematics is limited, unless for anterior-posterior translation.

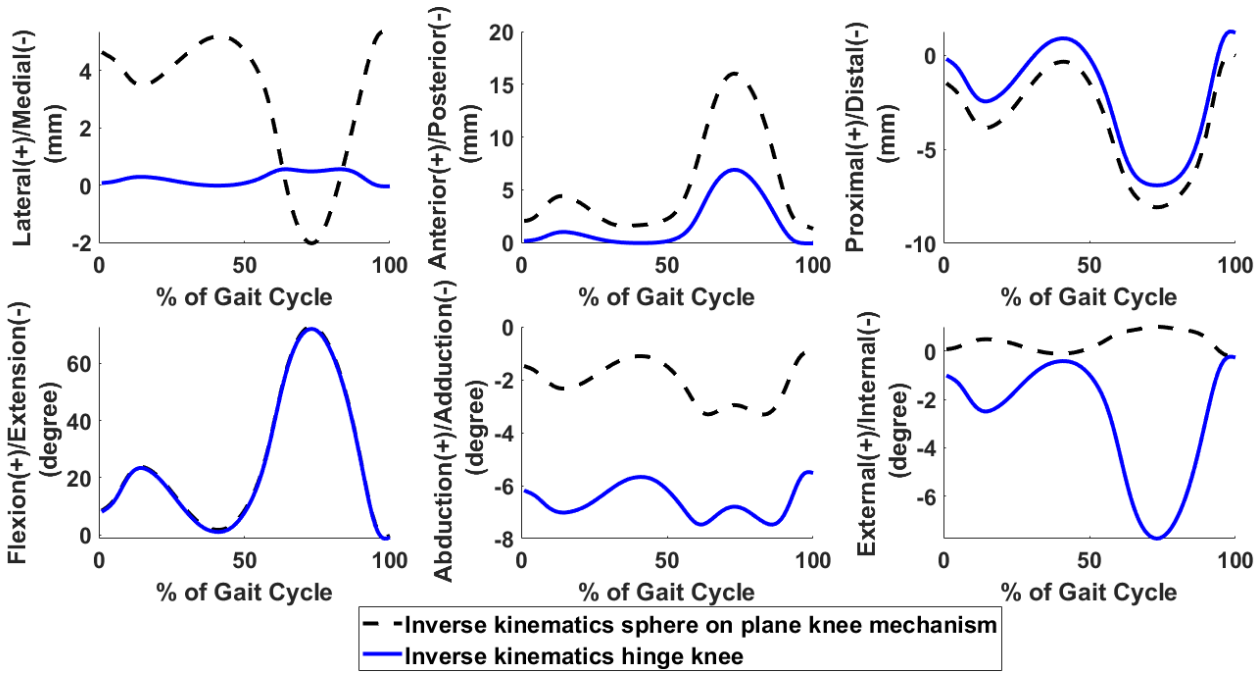

Figure 6-4, Tibiofemoral joint kinematics during a gait cycle obtained from the inverse kinematic model of the subject developed in Matlab. The knee mechanism once features personalized sphere-on-plane constraints while minimizing the ligament lengths and once a hinge mechanism.

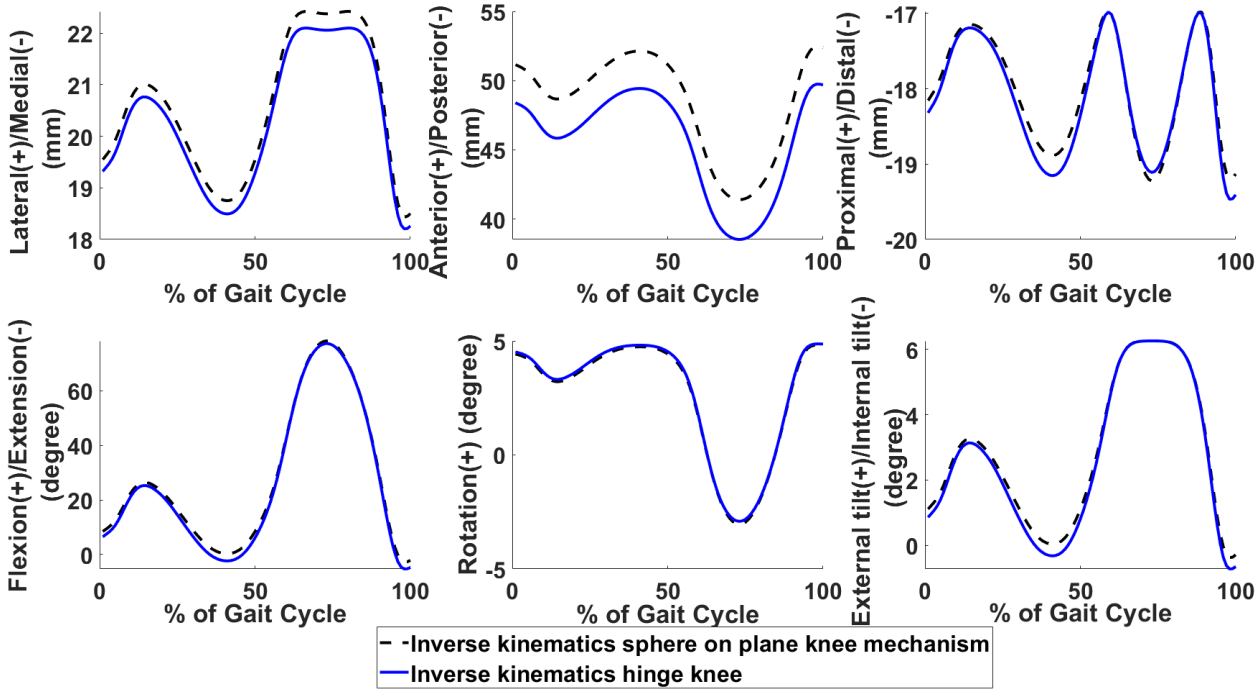

Figure 6-5, Patellofemoral joint kinematics during a gait cycle obtained from the inverse kinematic model of the subject developed in Matlab with different knee mechanisms.

6.3.2 Defining the inertial parameters of the inverse model

The skin markers placed on the subject during gait analysis were used to define the five lower limb segments and the local coordinate frame of each body segment [170]. These segment frames were used to define the inertial parameters of the subject. The inertial parameters of the segments are estimated by the regression equations of Dumas et al. [180,181] adjusted from the data of *McConville et al*. [182] and *Young et al*. [183].

The Body Segment Inertial Parameters (BSIPs) refer to: 1) segment mass, 2) position of the segment's center of mass with respect to its local frame, 3) segment moments and products of inertia with respect to the segment's local frame about its center of mass. BSIPs defined for the subject in this study are provided in Table 6-2. Patella mass and position of its origin are approximated based on by *Delp et al*. [176].

Table 6-2 The BSIPs for the musculoskeletal model

Segment name	Segment length	Segment mass	Center of mass in segment frame	Rotational inertia with respect to the center of mass in its local frame
Foot	0.1411	1.1092	[0.0473;-0.0187;0.00322]	[4.91e04,0,0; 0,0.0023,0; 0,0,0.0022]
Shank	0.3959	4.4370	[-0.01844;-0.1575;0.0027]	[0.0513,0,0; 0,0.0065,0; 0,0,0.05134]
Patella	0.0302	0.0975	[0;0;0]	[0,0,0;0,0,0;0,0,0]
thigh	0.3857	11.3698	[-0.0160;-0.1677;0.0129]	[0.1462,0,0; 0,0.0391,0; 0,0,0.1565]
pelvic	0.1075	10.4998	[0.0023;-0.0230;-4.944e-04]	[0.0909,0,0; 0,0.1001,0; 0,0,0.08043]

6.3.3 Inverse dynamics and solving the muscular redundancy

The obtained segment kinematics from section 6.3.1 along with the force-platform data during the gait session and the defined inertial parameters were used to solve the inverse dynamics problem and to acquire the inter-segmental moments. Followed by that a one-step static optimization procedure (that is to say computing simultaneously muscle-tendon forces and contact forces) with minimizing the sum of squared muscle-tendon forces was conducted to solve the muscular redundancy [184].

The procedure conducted at this level was the same for the kinematic data acquired from both knee mechanisms (sphere-on-plane and minimized ligament length variations versus hinge). The principles of the conducted inverse dynamic optimization is described in Figure 6-6. The computed muscle-tendon forces using the sphere-on-plane knee mechanism is presented in Figure 6-7 as a sample.

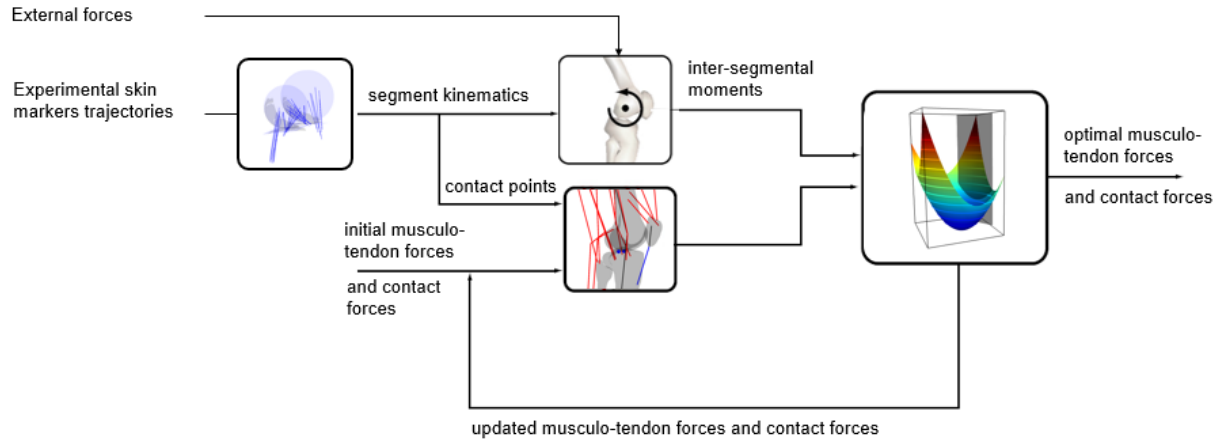

Figure 6-6, Principles of the inverse dynamics-based optimization (adapted from Erdermir et al. [2] to the present model and method)

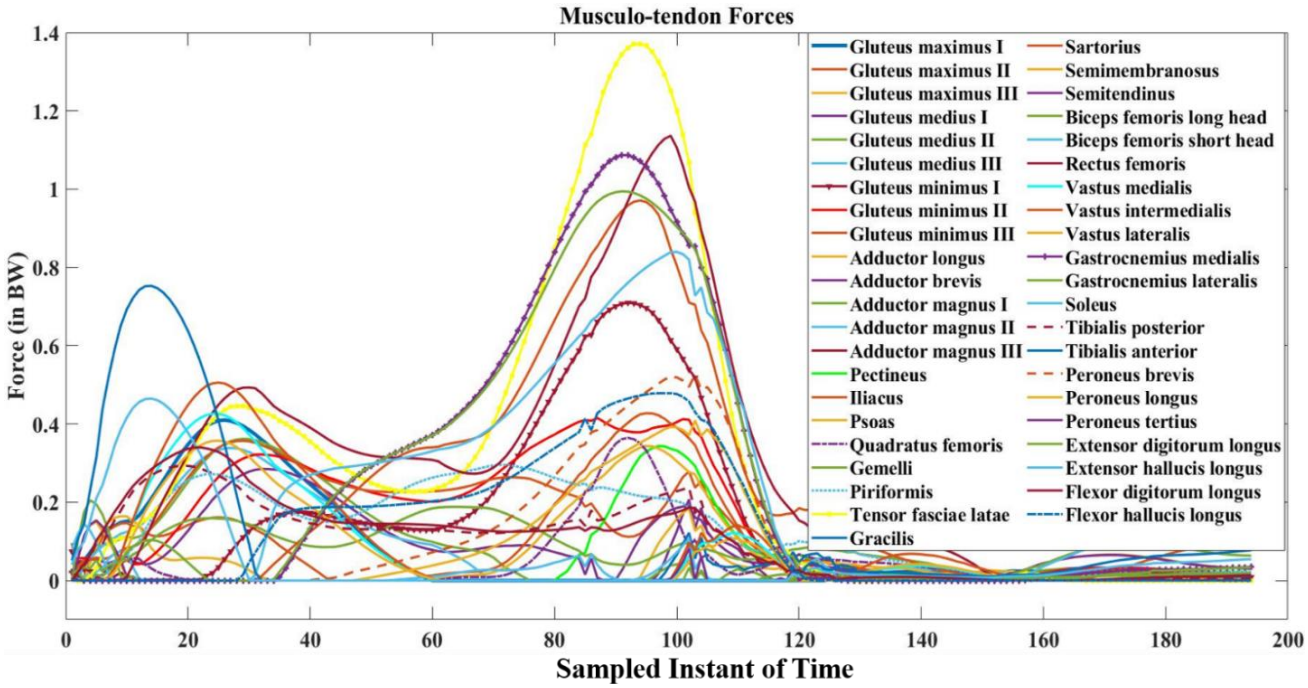

Figure 6-7, Muscle-tendon forces computed for the subject at each time frame during a gait cycle.

6.4 Forward simulation of gait in Artisynth

Following the steps conducted in the previous sections, we have obtained the kinematics of the subject's body segments and the muscle forces during a gait cycle. In addition, the position of the center of pressure on the foot during gait is provided to apply the ground reaction forces and

moments corresponding to each time frame. The coordinates of the center of pressure and the positions of the segments are defined in a global coordinate system that is defined at one corner of the force-platform during the gait session.

Our objective is to run a forward simulation of the gait session with the Artisynth model having deformable knee joints. The first step to do so is to transform the segments to the correct position defined in the global frame of the gait session. The provided data from the results of the inverse kinematic simulations contain the transformation matrices of each segment that takes the segment to its correct position at each time step during gait. However, it is important to be mentioned that the Artisynth musculoskeletal model was defined in the global frame of the CT scan image acquisition and thus we have performed an extra step of transformation to take each segment to its local segment frame before applying the transformation that takes the segments to its position at a time step during gait.

The same concern exists while importing the BSIPs to the Artisynth model. In the BSIP presented in Table 6-2, the position of the segment's center of mass is given with respect to its local frame. Additionally, the segment moments and products of inertia are defined with its local frame and about its center of mass. As a result, when importing the BSIP to the Artisynth model a step of transformation was required. Further information about the methods required to define the inertial parameters of a rigid body in Artisynth when the body local coordinate frame is not located at its center of mass can be found in Appendix A.6 of the Artisynth documentation (www.artisynth.org).

6.4.1 Model setup

As a reminder, the model-based kinematics in section 6.3 was obtained once having personalized sphere-on-plane constraints in the knee mechanism and minimization of ligament

length variations and once using a hinge mechanism for the knee joint. As a result, we first were interested to see if the exact same predicted kinematics in the aforementioned cases can be used for setting up the model for a forward simulation starting at the beginning of the stance phase while adding the articular cartilages and deformable ligaments. Figure 6-8 shows the relative position of the femur and tibia at the beginning of the stance phase predicted by the two aforementioned kinematic models. As visible in this figure, the gap between the bones is close to zero in some areas, and insertion of the tibial cartilages will cause model divergence due to intersecting FE components despite the fact that the cartilages are very thin layers of elements attached to the surface of the bone and generated based on the segmentation of the articulation from high-resolution MRI images.

Having this information in mind, to set up the model for a forward simulation starting from the beginning of the stance phase, we have decided to include only the femoral cartilage. Additionally, models were generated without the presence of any FE components with the objective of recreating a forward version of the multibody inverse model and compare the kinematics with the ones expected from the model.

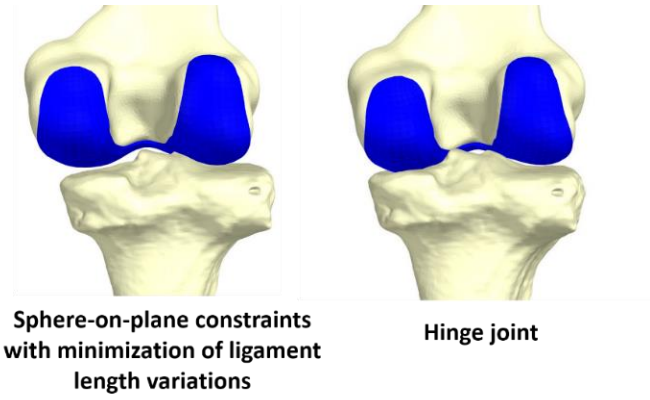

Figure 6-8, The relative position of femur and tibia at the beginning of stance phase predicted by different kinematic models used on the same gait trail. The blue FEM is the femoral cartilage.

As a second step, inspired by the conventional studies combining the FE and MS models [53,169], we have used the FE model of the articulation (tibial and femoral cartilages in absence of the menisci) at 25° knee flexion that was generated from the MRI images. As a result, the relative position of the bones is coming from MRI segmentation and there is no interpenetration of the tissues. The FE components in this model were then transformed to the closest time frame of the gait with similar knee flexion that was found to be at 14% of the gait cycle without changing the relative position of the bones. This enabled us to run a forward simulation of gait starting at 14% gait cycle in presence of the tibial and femoral cartilages without the issues regarding FE model interpenetration (other soft tissues could also be included but for simplicity reasons, they were excluded in the current study) to monitor the local response of the joint. A schematic of the model setups explained is presented in Figure 6-9.

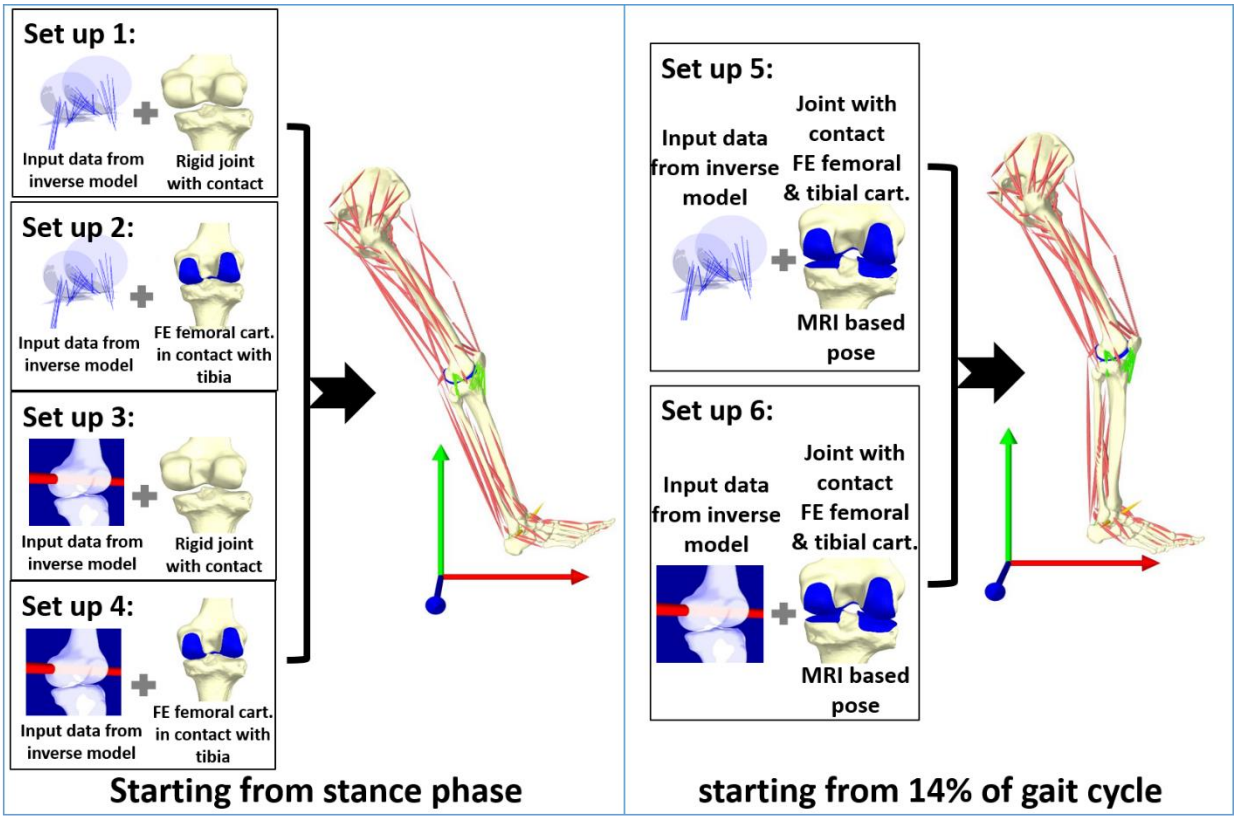

Figure 6-9, Schematic of the model setups used for the forward gait simulation with Artisynth

6.4.2 Loading and boundary conditions

The forces of 43 muscle-tendon units computed by minimizing the sum of squared muscle-tendon forces in the inverse dynamics model were imported to the model at each time step. The motions of the pelvic and foot segments were controlled using their transformation matrices extracted from the results of the corresponding inverse simulation. Similar to the inverse kinematics model generated from the subject, the hip joint was defined as a spherical joint positioned at the center of the femoral head. The ankle joint was formed of a tibiotalar and a subtalar joint. The patellofemoral joint was modeled as a hinge joint between the patella and the femur. For further details on the joint axes used please refer to section 6.3. As the focus of the forward simulation was on the knee joint, no ligaments were defined at the ankle and hip level to conserve the joint moments similar to the ones computed with the inverse model. The initial speed of each segment at the beginning of the simulation was computed using the results of inverse kinematic simulations and was set as an input of the model.

The ground reaction forces and moments were directly applied to the center of pressure of the foot, based on the data obtained from the force-platform. It is important to be mentioned here that the location of the center of pressure as well as the force and moment vectors provided from the force-platform at each time step are defined in the global coordinate frame of the gait session that is placed at one corner of the platform. It is also important to be mentioned that the external forces and moments applied to a rigid body in Artisynth are defined with respect to the global coordinate frame of the model but are applied to the origin of the body frame. As a result, the extra moment vector produced when moving the force vector from the center of pressure to the origin of the frame was computed and added to the ground reaction moment vector.

6.4.3 Outcome measures

Tibiofemoral and patellofemoral kinematics as defined by the ISB standards were computed in the Artisynth models to be compared with the kinematics obtained from the corresponding Matlab inverse model. The generated Artisynth models use contact between components as well as the connective tissues for running the joint mechanism. Thus in presence of the FE cartilages, the contact area, as well as nodal values of contact forces, can be computed. On the other hand, as mentioned in Figure 6-6, the location of the medial and lateral contact points are estimated with the inverse kinematic model that features a sphere on plane knee mechanism. These contact points are then prescribed at the level of solving the muscular redundancy to estimate the contact forces.

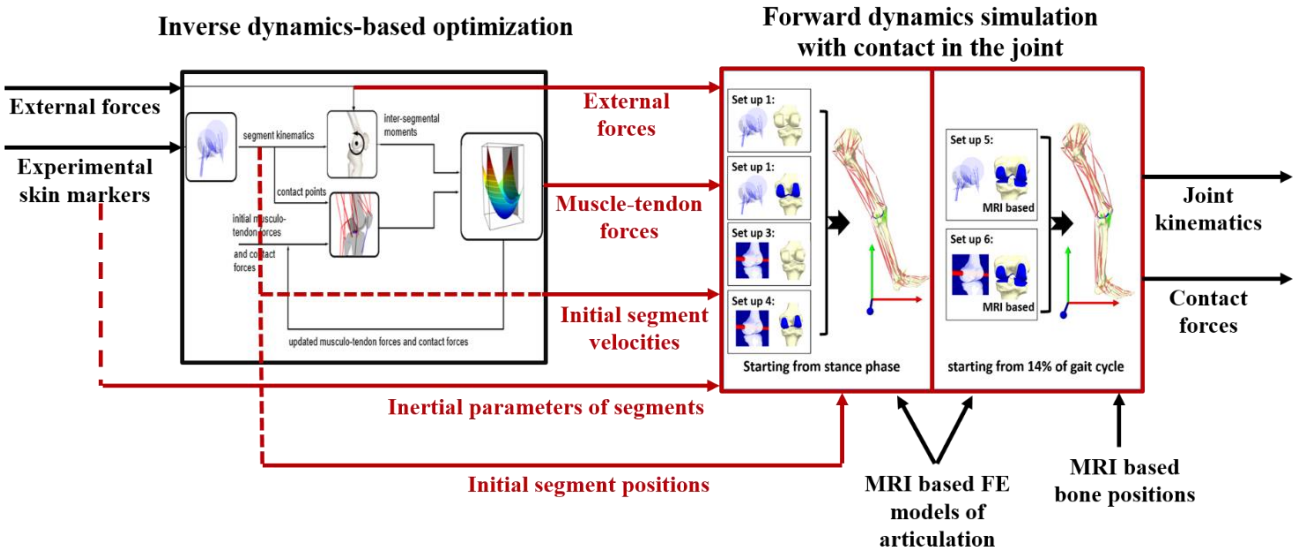

Figure 6-10, Principles of the inverse-forward study performed in the current chapter.

In the current manuscript, the contact area of the medial and lateral cartilages was monitored in the combined model that included the tibial and femoral cartilage had the muscular forces of the sphere on plane inverse model as in input (model setup 5). These areas where compared against the contact point locations of the inverse model at several time frames during gait cycle.

A schematic of the principles of the inverse-forward study conducted in the present chapter is presented in Figure 6-10 to clarify the input and output of the combined model generated in Artisynth.

6.4.4 Results

Simulations that were run by the data acquired from the inverse models having hinge and sphere on plane knee mechanisms predicted different kinematic results for both tibiofemoral and patellofemoral joints. The kinematic results of the Artisynth models were compared against their corresponding inverse models that were used to define their input including their initial positions and velocities and/or muscle forces (Figure 6-11 to Figure 6-14).

The predicted tibiofemoral kinematics with the forward simulation in presence of contact show noticeable instabilities in all degrees of freedom other than flexion/extension (primary kinematics). The proximal-distal translation plots substantially deviate during a period in the gait cycle. This period is matching the only deviated part of the flexion-extension plots from the inverse kinematics and the largest observed deviations in the medial/lateral direction as depicted in Figure 6-11 and Figure 6-12. Similar ranges and patterns can be spotted in the translational degrees of freedom other than during the aforementioned deviated period. Meanwhile, the rotational degrees of freedom experience a non-stability that affect visual pattern recognition. It is interesting to note that atypical external tibial rotation tends to appear with flexion with the deformable joint. This was present in the inverse kinematics obtained with the hinge joint but not present in the inverse kinematics obtained with the sphere on plane joint with minimized ligament length variations.

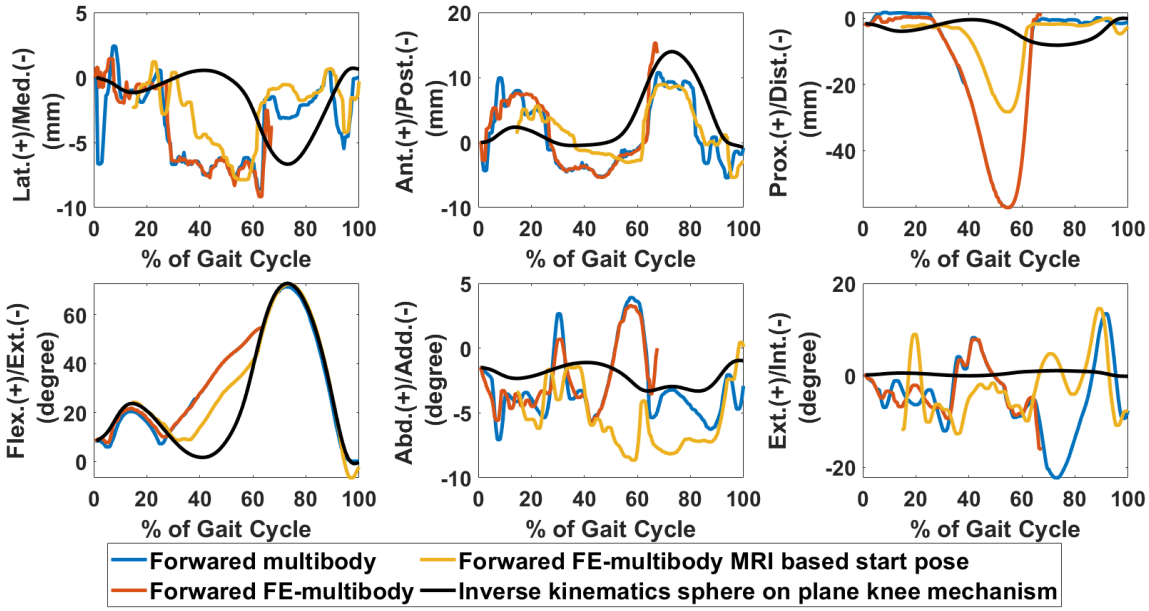

Figure 6-11, Tibiofemoral kinematics by inputting the muscle forces computed with the inverse method having sphere on plane knee mechanism and minimized ligament length variations

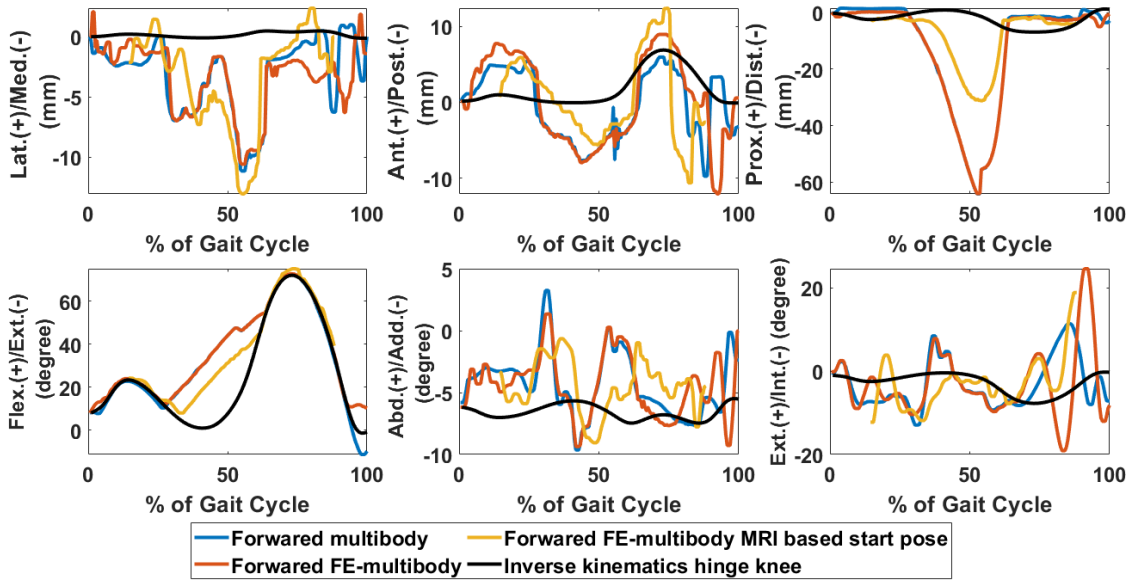

Figure 6-12, Tibiofemoral kinematics by inputting the muscle forces computed with the inverse method having hinge knee mechanism

Concerning the patellofemoral kinematics, the overall instability observed in the curves is less compared to the tibiofemoral kinematics. However, the plots are substantially different compared

to the inverse kinematic plots despite the fact that the patellofemoral joint was defined in the exact same manner as the inverse model (a hinge joint between the patella and the femur). Some similar patterns can be spotted in the initial peaks and final parts of the kinematic curves other than the medial/lateral and internal/external tilt. The same deviation effect of the tibiofemoral plots is present and the results have a sudden deviation in a time period starting at around 30% of the gait cycle. The MRI-based model shows higher quality results when ran by hinge knee mechanism muscle forces.

The contact area of the medial and lateral cartilages was monitored in the combined model that included the tibial and femoral cartilage and was ran by the muscular forces of the sphere on plane inverse model (model setup 5 of Figure 6-9). These areas are compared against the corresponding contact points prescribed in the inverse model in Figure 6-15. Again, atypical external rotation of the contact points on the tibia appears with the deformable joint at 80% of flexion, opposite to the contact points derived from the inverse kinematics obtained with the sphere on plane joint with minimized ligament length variations.

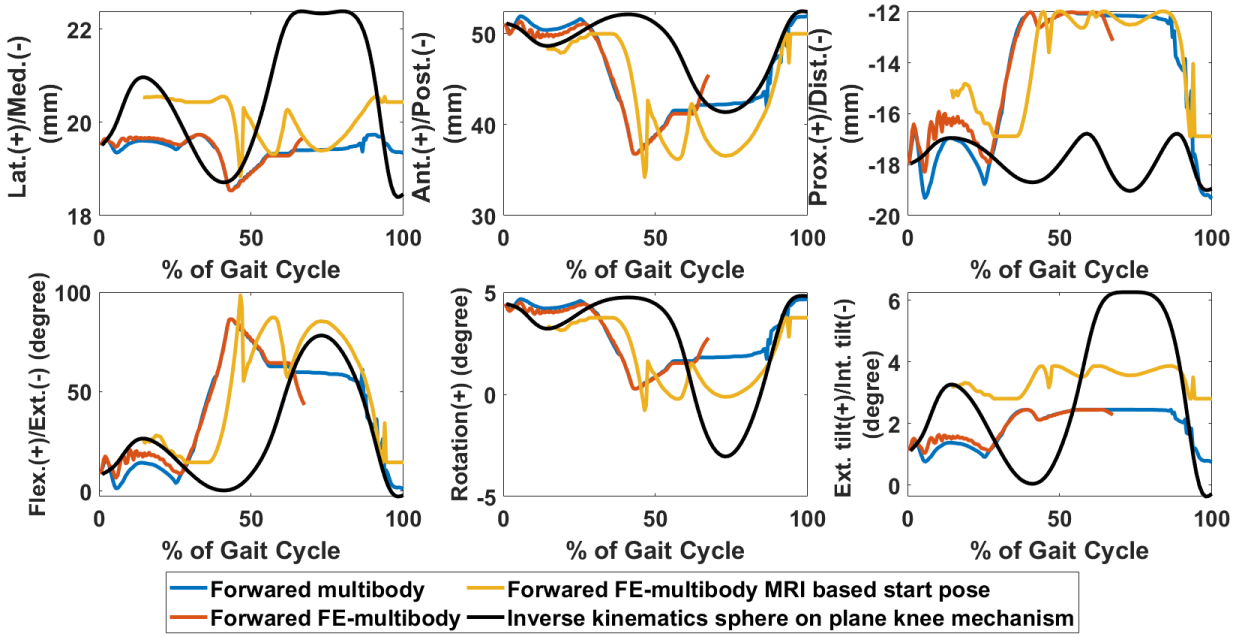

Figure 6-13, Patellofemoral kinematics by inputting the muscle forces computed with the inverse method having sphere on plane knee mechanism and minimized ligament length variations

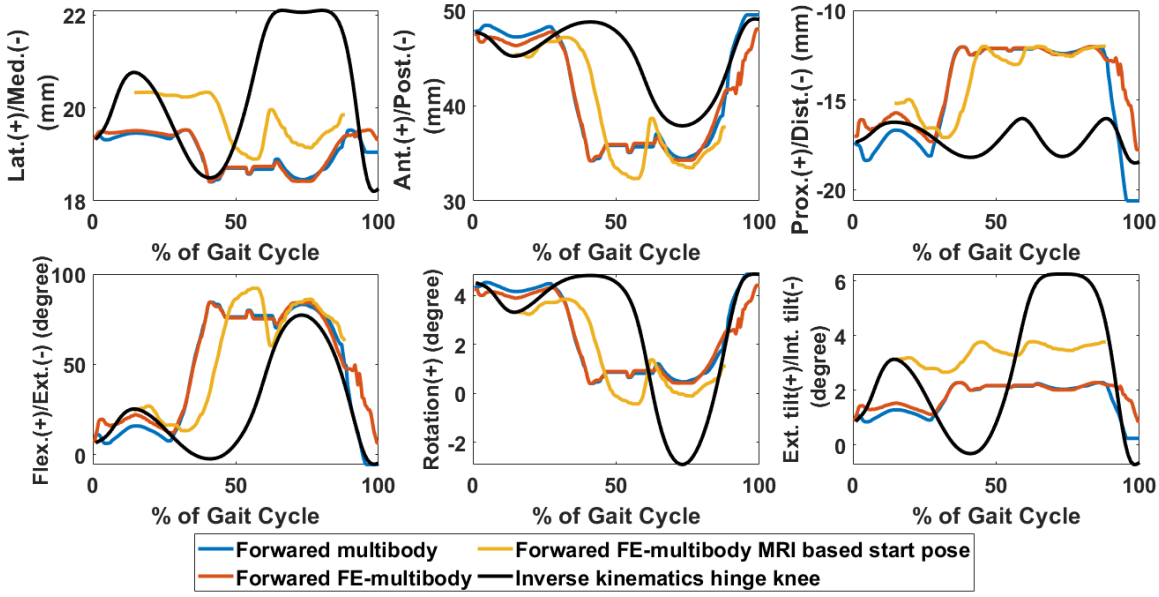

Figure 6-14, Patellofemoral kinematics by inputting the muscle forces computed with the inverse method having a hinge knee mechanism.

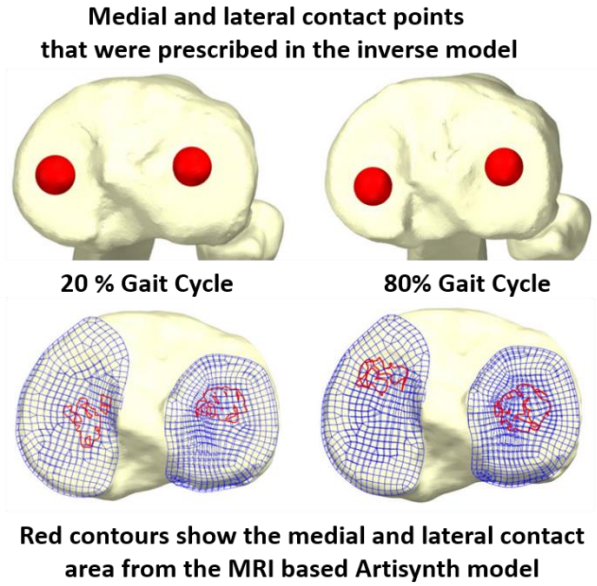

Figure 6-15 The predicted contact areas on the FE cartilages compared to contact points prescribed to the inverse multibody model.

6.4.5 Discussion

We have introduced a dynamic combined FE-multibody model of the lower limb that features the muscle-tendon units along with connective tissues and FE representation of articular surfaces. As a primary application, we aimed to evaluate the predictions made with inverse multibody MS models having the same personalized description of the muscular geometry but different kinematic knee models and muscle recruitment algorithms on a forward simulation in Artisynth without committing a high computational cost. This application is particularly aimed to provide further insight into possible limitations of using sequential combined FE and multibody approach with inconstant joint definitions at modelling scales and in dynamic situations.

In each of the simulations that were conducted with the combined Artisynth model, the muscular forces, inertial parameters, initial segment velocities and positions, and external forces are similar to the corresponding inverse simulation. Indeed, the only difference was that instead of

defining a joint mechanism, the joints were constrained by contact and connective tissues (in existence or nonexistence of FE articular cartilages). Thus the objective was to see if prescribing the muscle forces and other aforementioned inputs (including the position of the pelvic and foot segments that were prescribed throughout simulation) will lead to divergence from the inverse kinematics that was used as the starting point of the calculations.

The first observation we made from the extracted tibiofemoral and patellofemoral kinematics (Figure 6-11 to Figure 6-14) was that other than the primary kinematics (which was only deviated during a period) the predicted kinematic plots were different and rather unstable compared to the original kinematic plots of the inverse model. While the source of this difference and instability is not clear, it can primarily be related to the fact that the dynamic simulation includes the efforts related to the articular structures that were not included in the inverse models. In addition to this main effect, minor instabilities can be caused due to running the models with direct muscle force inputs without the existence of a muscle-tendon model that features damping parameters. The forward simulation works as an open-loop that blindly applies the computed muscle forces without any feedback or correction mechanism to impose kinematics. Thus, the model is very sensitive to the input values and also the way that the values are used especially in longer simulations such as a whole gait cycle where the deviations have time to accumulate.

The kinematics produced with the forward simulation did not have a noticeable improvement when using the input data from the sphere on plane knee mechanism but using this model provided the chance to pursue further investigations such as on the medial and lateral contact forces and contact points that can be interesting for applications on pathological joints. Nevertheless, currently, the kinematics obtained with this inverse model is not directly applied but transformed into contact point trajectories prescribed as a function of knee flexion. This interpolation with

flexion angle results in a similar (averaged) behavior during stance and swing. As a result, direct application of the contact points in the inverse model could have improved the results obtained by the forward simulation.

Monitoring the extracted kinematics (Figure 6-11 to Figure 6-14) shows that the kinematic plots of the models starting from the stance pose matched the inverse kinematic plots at the first time frame as expected. Meanwhile, for the cases where the model started from MRI-based relative bone positions, the plots do not initiate from a matching point on the inverse kinematic plots in some degrees of freedom of the secondary kinematics. This indeed can be an indication of the difference that exists between the passive and active secondary kinematics (in other words load-dependent kinematics) of the joints as previously shown by a forward simulation conducted by *Lenhart et al*. [10]. Interestingly, for the patellofemoral joint other than the proximal/distal and medial/lateral kinematic plots the other plots of the MRI-based pose model are initiating from a point on the curve predicted by inverse kinematics. This indicated that the passive kinematics were similar to the model predictions at this specific point. Of course, the observation cannot be generalized as further points along the gait cycle are not assessed.

Taking a closer look at the various plots we observed a substantial deviation from the inverse kinematics during a period of gait cycle starting at around 30%. Starting the simulations from the MRI based relative bone positions helped with reducing the deviation values during this period and also resulted in shortening the deviation period.

To find the potential correlation between this deviation, we plotted the muscle forces that were active in the knee and compared the deviation period of the primary kinematics as depicted in Figure 6-16. This investigation clarified that 7 of the muscles active in the knee (out of 14 muscles modeled for this joint) are experiencing zero or very low forces at approximately the same period

where the deviation present. Particularly in the quadriceps muscle group that consists of the RF, VM, VL, VI, only the RF muscle stays active. The other three muscles are inactive until the time frame that the deviation is increasing in the proximal/distal direction. Additionally, the patellar ligament has been modeled with a rigid link in the inverse model although in the Artisynth combined model it is represented by nonlinear springs. As a result, taking a rigid assumption for the patellar ligament might have affected the prediction of quadriceps muscle group calculation with decreased activation levels. This point should be further investigated in the future steps of this study and the forces of the patellar ligament can be compared between models.

On the posterior side of the knee joint, the gastrocnemius which has the role of a knee flexor presents a significant force on the muscle-tendon force curves during the deviated period. However, during this phase of the gait cycle, a synergistic work with the quadriceps muscle group seemed required to limit the advance of the tibia. Thus excessive force in the gastrocnemius could have created a deficient agonist-antagonist ratio with the quadriceps muscle group. This excessive force can be caused by the compromise made on the moment arm of these muscles when using a single fixed via-point for the whole range of motion. Finally, since the hip and ankle center of rotation are constrained by the simulation, any modification in one plane will have consequences in the other two planes, so the increase in flexion and adduction will cause the unrealistic distance between tibia and femur that is observed in Figure 6-16. As a result, a part of this deviation problem might also be sourced out to the activation of the muscles in the hip joint that need further investigation in the future steps of this study.

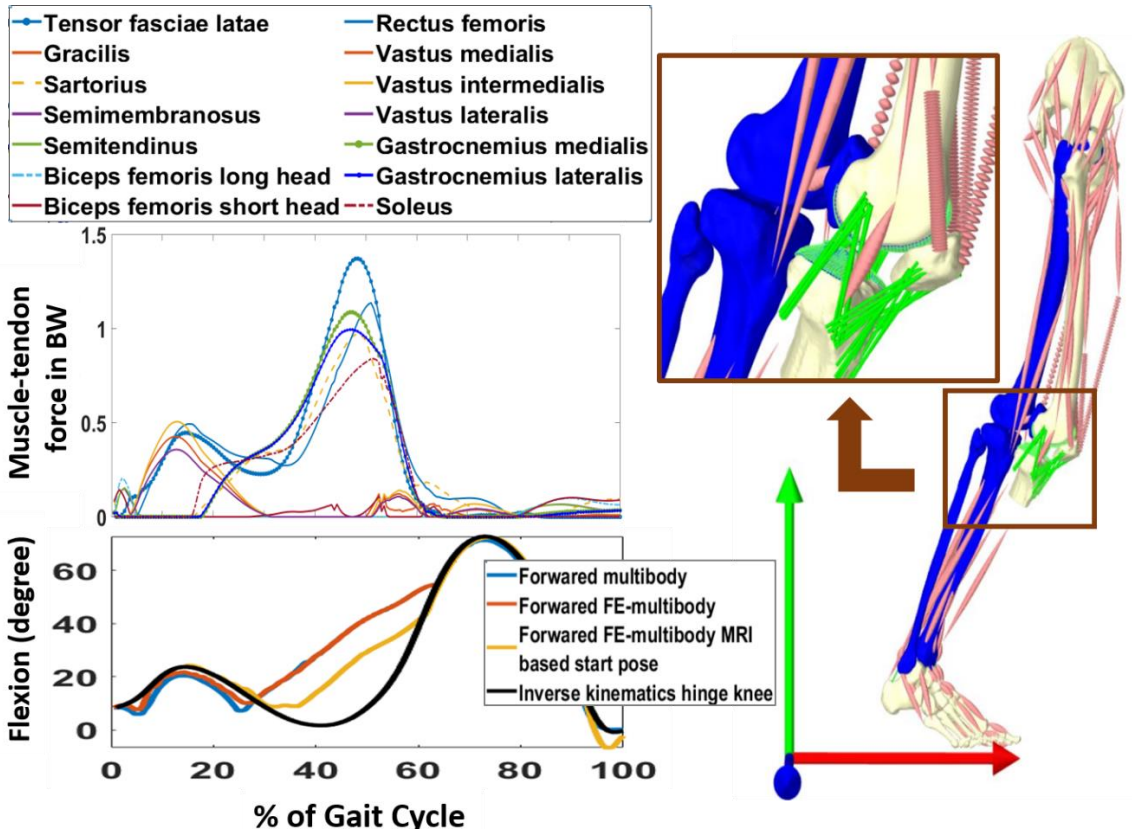

Figure 6-16, Observation of the most deviated period during gait cycle and correlation with the muscle forces (blue is the segment position obtained with inverse kinematics).

The location of the contact area is found to be more anterior in the medial cartilage at 80% gait due to differences in tibiofemoral internal/external rotation as depicted in Figure 6-15. It is important to be mentioned that the contact forces of the medial and lateral tibiofemoral compartments could be also monitored from model setup 5 and get compared against the inverse computations. The means to pursue such an objective are being developed currently but the results have not been provided in this manuscript as the computations are facing slight instability problems that need to get resolved in future steps.

In conclusion, on the basis of the current observations, it seems that the generated forward simulation is highly sensitive to the prescribed muscular forces and thus can be used for evaluating various inverse modelling options. The present inconsistency between the joint models used in the

inverse and forward simulations could raise problems our dynamic simulations. This issue is observed despite the fact that we used state-of-the-art methods to build personalized inverse models of our subject [185].

6.5 Perspectives of combined FE-multibody gait simulation

As previously mentioned, the presented collaborative work in this chapter is still developing and thus there are multiple perspectives envisioned for it. While we have taken a primary step towards testing the performance of the sequential multibody and FE approach with joint definition inconsistency at different scales, further investigation of the instability sources and recreating the same models in quasi-static situations seems necessary to validate our conclusions. Additionally, further detail at the joint level such as the FE model of the menisci and enhancement of the muscle moment arms shall be done in future versions. In addition, at the current step we have only tested one criterion for static optimization (minimizing the sum of squared muscle-tendon forces). Indeed, other choices which simultaneously minimized contact forces or patellar tendon could also get tested with the developed framework [163]. Another envisioned perspective is to explore the sensitivity of the method to integrate the "screw-home" mechanism of functional anatomy [186].

In addition to this model testing application, the future goal of the present work is to make an attempt on designing a framework where the muscle recruitment problem is solved while accounting for the response of the deformable components and benefitting from the validated muscle recruitment algorithms that are developed for multibody inverse models. With development of such framework, it will be possible to attempt for having forward dynamic simulations including deformable joints that have muscle control from motion analysis as an input.

The aforementioned future steps shall pave the road for the application of combined FE-multibody models to dynamic simulations of subjects with pathological joints or surgical

interventions such as high tibial osteotomy. Indeed, the chance of having a modular model as created in chapter 3 and using the 3D FE representation of the muscles similar to what was defined in chapters 4 and 5 for the quadriceps muscle group, also open new perspectives in the formation of models with active FE muscles.

7

General conclusion

In this thesis, combined FE-multibody musculoskeletal models of the lower limb have been developed and applied to study biomechanically and clinically relevant questions. The contributions, results, limitations and perspectives of the various performed studies have been already discussed in the corresponding chapters. In the following parts, we summarize the main findings and contributions of the thesis.

A complete dataset of a subject was collected as a starting point including the geometry of the joints, muscles, articulations, and connective tissues and further information obtained from gait analysis and from MRI collected at various knee flexion angles. This dataset was formed and treated while having the objective of a modular modelling concept in mind. This concept can indeed be introduced while using a combined FE-multibody platform because the various components of the lower limb can be represented with different levels of complexity. In this sense, the decision about inclusion and representation of each component can be made based on the application that the model is being generated for. Hence, in the current thesis, we have taken an

initial step towards a complete modular model of the lower limb where the design of the model can be fully changed in a few minutes. The capabilities of such modelling approach were indeed reflected in the various models that were presented for clinical or biomechanical applications throughout the different chapters of this thesis. The models ranged from multibody MS models including only 2D muscle-tendon actuators to more complex models that included the 3D FE representation of the quadriceps muscle group along with deformable joints. Different joints, for instance the patellofemoral or the tibiofemoral joint, can be brought under the spotlight based on the application and the components are interchangeable. Additionally, different representations for the components and new modelling techniques can get tested for an application similar to what was done in chapter 4.

To bring this modelling approach into practice, we had envisioned applying it for better understanding the complications of open wedge high tibial osteotomy (OWHTO), an orthopedic surgery to treat patients with a varus lower limb deformity. An extended systematic review of the medical and biomechanical literature was conducted to find the areas where such biomechanical models can contribute or the areas where the existing numerical studies need to be enhanced. The findings of this review revealed that some of the complications of this surgery, namely the patellar height descent and excessive medial pressures due to MCL tightness, could be related to modifications of the soft tissue insertion sites after wedge opening. Meanwhile, despite the need for further analysis on the soft tissue aspect of the OWHTO, this point has not been addressed and has mainly been neglected by numerical simulations. As a result, two questions were formed that required further investigation with a biomechanical simulation.

The first question concerned the impact that alteration of the superficial bundle of MCL (happening due to OWHTO) can have on the contact force and stress distribution on the

tibiofemoral compartments. In the investigation performed on this question, our results showed that the change induced in the length and tension of sMCL in the process of wedge opening can substantially impact the tibiofemoral contact forces and stress distribution. Besides, releasing the sMCL bundle could instantly reduce the medial contact forces. As a result, the impact of wedge opening on moments produced by the soft tissues should not be neglected and the approach of the surgeon towards releasing sMCL shall be considered in numerical simulations. Hence, if a numerical simulation that is aiming to find the optimal alignment for a patient does not account for these points, the final decisions on the opening angles required for the patient may be affected. However, this effect is unfortunately neglected by many biomechanical studies that are used for taking simulation-based decisions on the optimal correction balancing the contact force in knee compartments. Our results were also in agreement with the general consensus that releasing the sMCL while wedge opening helps with shifting the weight to the lateral compartment in normal situations without initial ligament laxity or instability. In addition, the performed investigation highlighted the importance of clarifying the insertion site of sMCL with respect to HTO cut.

The second question regarding OWHTO was indeed about the correlation between the distalization of the patellar ligament insertion (due to wedge opening) and the patellar position. For investigation on this matter, we used the validated MS model of the quadriceps muscle group developed in chapter 4, with FE muscle and articular surfaces. Our results demonstrated that wedge opening can alter the patellar position. The simulations provided information about the correlation between the size of the wedge opened on the tibia and the patellar position in various DOFs that are not measured with standard radiographs. An increase of the stress inside the passive Rectus Femoris muscle was observed that could be an indication that the studies on OWHTO should adapt

the internal loading conditions in addition to the external loads that are changed due to modification of limb alignment.

The final part of this thesis presented a collaborative work under development that is being conducted to see the effect of the inconsistency of joint models used in a sequential approach. The joint models used for the multibody step of the sequential approaches are normally very simplified joints (such as a hinge mechanism for the knee) that are inconsistent with the FE deformable joint models in presence of connective tissues and contact in the articulation. The objective was to use the results of inverse multibody MS models with simplified joint models as an input to run forward-based dynamic simulations in presence of deformable FE components and monitor the results. This indeed can highlight the importance of such inconsistency in dynamic simulations and also be used as an evaluation method in some sense to enhance the principles used for inverse dynamics-based optimizations.

A complete MS model of our subject was developed having MT units and was exported to another platform and turned into a multibody model to solve the muscle recruitment problem. The results of that step were then imported to the combined model in Artisynth and were used to run forward combined FE-multibody simulations. The kinematic results showed that the primary tibiofemoral kinematics were reproduced relatively well other than during a period of gait cycle starting at around 30%. On the other hand, the tibiofemoral secondary kinematics and patellofemoral kinematics were generally not stable and showed only some partial similarities. From the current observations, it can be concluded that the inconsistency of the joint models used in a sequential approach can raise problems when using dynamic simulations especially without imposing the primary kinematics. This effect is present even though we used state-of-the-art methods to build personalized inverse models. As a result, solving the muscular redundancy

problem in a single platform as the deformable joint model and while accounting for the ligament moments can be a major improvement. Indeed, solutions for such issues can also be found through modifying the principles used for inverse dynamics-based optimizations. In addition, the developed inverse-forward method in this chapter is very sensitive to the input data and thus can be used for evaluation purposes. However, further data extraction and investigations are still required on the simulation results of this developing work.

BIBLIOGRAPHY

[1] Pandy MG. Computer Modeling and Simulation of Human Movement. Annu Rev Biomed Eng 2001;3:245–73. https://doi.org/10.1146/annurev.bioeng.3.1.245.

[2] Erdemir A, McLean S, Herzog W, van den Bogert AJ. Model-based estimation of muscle forces exerted during movements. Clin Biomech 2007;22:131–54. https://doi.org/10.1016/j.clinbiomech.2006.09.005.

[3] Praagman M, Chadwick EKJ, Van Der Helm FCT, Veeger HEJ. The relationship between two different mechanical cost functions and muscle oxygen consumption. J Biomech 2006;39:758–65. https://doi.org/10.1016/j.jbiomech.2004.11.034.

[4] Rasmussen J, Damsgaard M, Voigt M. Muscle recruitment by the min/max criterion - A comparative numerical study. J Biomech 2001;34:409–15. https://doi.org/10.1016/S0021-9290(00)00191-3.

[5] Crowninshield RD, Brand RA. A physiologically based criterion of muscle force prediction in locomotion. J Biomech 1981;14:793–801. https://doi.org/10.1016/0021-9290(81)90035-X.

[6] Pedotti A, Krishnan V V., Stark L. Optimization of muscle-force sequencing in human locomotion. Math Biosci 1978;38:57–76. https://doi.org/10.1016/0025-5564(78)90018-4.

[7] Liu MQ, Anderson FC, Pandy MG, Delp SL. Muscles that support the body also modulate forward progression during walking. J Biomech 2006;39:2623–30. https://doi.org/10.1016/j.jbiomech.2005.08.017.

[8] Pandy MG, Zajac FE. Optimal muscular coordination strategies for jumping. J Biomech 1991;24:1–10. https://doi.org/10.1016/0021-9290(91)90321-D.

[9] Raasch CC, Zajac FE, Ma B, Levine WS. Muscle coordination of maximum-speed pedaling. J Biomech 1997;30:595–602. https://doi.org/10.1016/S0021-9290(96)00188-1.

[10] Lenhart RL, Kaiser J, Smith CR, Thelen DG. Prediction and Validation of Load-Dependent Behavior of the Tibiofemoral and Patellofemoral Joints During Movement. Ann Biomed Eng 2015;43:2675–85. https://doi.org/10.1007/s10439-015-1326-3.

[11] Delp SL, Loan JP. A graphics-based software system to develop and analyze models of musculoskeletal structures. Comput Biol Med 1995;25:21–34. https://doi.org/10.1016/0010-4825(95)98882-E.

[12] Damsgaard M, Rasmussen J, Christensen ST, Surma E, De Zee M. Analysis of

musculoskeletal systems in the AnyBody Modeling System 2006. https://doi.org/10.1016/j.simpat.2006.09.001.

[13] Delp SL, Anderson FC, Arnold AS, Loan P, Habib A, John CT, et al. OpenSim: Open-source software to create and analyze dynamic simulations of movement. IEEE Trans Biomed Eng 2007;54:1940–50. https://doi.org/10.1109/TBME.2007.901024.

[14] Paul C, Bellotti M, Jezernik S, Curt A. Development of a human neuro-musculo-skeletal model for investigation of spinal cord injury. Biol Cybern 2005;93:153–70. https://doi.org/10.1007/s00422-005-0559-x.

[15] Higginson JS, Zajac FE, Neptune RR, Kautz SA, Delp SL. Muscle contributions to support during gait in an individual with post-stroke hemiparesis. J Biomech 2006;39:1769–77. https://doi.org/10.1016/j.jbiomech.2005.05.032.

[16] Margaretha van der Krogt M, Bar-On L, Kindt T, Desloovere K, Harlaar J. Neuro-musculoskeletal simulation of instrumented contracture and spasticity assessment in children with cerebral palsy 2016. https://doi.org/10.1186/s12984-016-0170-5.

[17] Shelburne KB, Kim H-J, Sterett WI, Pandy MG. Effect of posterior tibial slope on knee biomechanics during functional activity. J Orthop Res 2011;29:223–31. https://doi.org/10.1002/jor.21242.

[18] Cohen ZA, Henry JH, McCarthy DM, Mow VC, Ateshian GA. Computer simulations of patellofemoral joint surgery: Patient-specific models for tuberosity transfer. Am J Sports Med 2003;31:87–98. https://doi.org/10.1177/03635465030310012701.

[19] Reinbolt JA, Fox MD, Schwartz MH, Delp SL. Predicting outcomes of rectus femoris transfer surgery. Gait Posture 2009;30:100–5. https://doi.org/10.1016/j.gaitpost.2009.03.008.

[20] Piazza SJ, Delp SL. Three-dimensional dynamic simulation of total knee replacement motion during a step-up task. J Biomech Eng 2001;123:599–606. https://doi.org/10.1115/1.1406950.

[21] Ali AA, Harris MD, Shalhoub S, Maletsky LP, Rullkoetter PJ, Shelburne KB. Combined measurement and modeling of specimen-specific knee mechanics for healthy and ACL-deficient conditions. J Biomech 2017;57:117–24. https://doi.org/10.1016/j.jbiomech.2017.04.008.

[22] Kiapour A, Kiapour AM, Kaul V, Quatman CE, Wordeman SC, Hewett TE. Finite element model of the knee for investigation of injury mechanisms: Development and validation. J Biomech Eng 2014;136:0110021. https://doi.org/10.1115/1.4025692.

[23] Wang Y, Fan Y, Zhang M. Comparison of stress on knee cartilage during kneeling and standing using finite element models. Med Eng Phys 2014;36:439–47. https://doi.org/10.1016/j.medengphy.2014.01.004.

[24] Mootanah R, Imhauser CW, Reisse F, Carpanen D, Walker RW, Koff MF, et al. Development and validation of a computational model of the knee joint for the evaluation of surgical treatments for osteoarthritis. Comput Methods Biomech Biomed Engin 2014;17:1502–17. https://doi.org/10.1080/10255842.2014.899588.

[25] Yang NH, Canavan PK, Nayeb-Hashemi H, Najafi B, Vaziri A. Protocol for constructing subject-specific biomechanical models of knee joint. Comput Methods Biomech Biomed Engin 2010;13:589–603. https://doi.org/10.1080/10255840903389989.

[26] Bendjaballah MZ, Shirazi-Adl A, Zukor DJ. Finite element analysis of human knee joint in varus-valgus. Clin Biomech 1997;12:139–48. https://doi.org/10.1016/S0268-0033(97)00072-7.

[27] Peña E, Calvo B, Martínez MA, Doblaré M. A three-dimensional finite element analysis of the combined behavior of ligaments and menisci in the healthy human knee joint. J Biomech 2006;39:1686–701. https://doi.org/10.1016/j.jbiomech.2005.04.030.

[28] Marchi BC, Arruda EM. A study on the role of articular cartilage soft tissue constitutive form in models of whole knee biomechanics. Biomech Model Mechanobiol 2017;16:117–38. https://doi.org/10.1007/s10237-016-0805-2.

[29] McLean SG, Mallett KF, Arruda EM. Deconstructing the Anterior Cruciate Ligament: What We Know and Do Not Know About Function, Material Properties, and Injury Mechanics. J Biomech Eng 2015;137. https://doi.org/10.1115/1.4029278.

[30] Orozco GA, Tanska P, Mononen ME, Halonen KS, Korhonen RK. The effect of constitutive representations and structural constituents of ligaments on knee joint mechanics. Sci Rep 2018;8. https://doi.org/10.1038/s41598-018-20739-w.

[31] Wilson W, Van Donkelaar CC, Van Rietbergen B, Huiskes R. A fibril-reinforced poroviscoelastic swelling model for articular cartilage. J Biomech 2005;38:1195–204. https://doi.org/10.1016/j.jbiomech.2004.07.003.

[32] Yao J, Snibbe J, Maloney M, Lerner AL. Stresses and strains in the medial meniscus of an ACL deficient knee under anterior loading: A finite element analysis with image-based experipmental validation. J Biomech Eng 2006;128:135–41. https://doi.org/10.1115/1.2132373.

[33] Naghibi Beidokhti H, Janssen D, van de Groes S, Hazrati J, Van den Boogaard T, Verdonschot N. The influence of ligament modelling strategies on the predictive capability of finite element models of the human knee joint. J Biomech 2017;65:1–11. https://doi.org/10.1016/J.JBIOMECH.2017.08.030.

[34] Dhaher YY, Kwon TH, Barry M. The effect of connective tissue material uncertainties on knee joint mechanics under isolated loading conditions. J Biomech 2010;43:3118–25. https://doi.org/10.1016/j.jbiomech.2010.08.005.

[35] Kazemi M, Li LP. A viscoelastic poromechanical model of the knee joint in large

compression. Med Eng Phys 2014;36:998–1006. https://doi.org/10.1016/j.medengphy.2014.04.004.

[36] Mo F, Li F, Behr M, Xiao Z, Zhang G, Du X. A Lower Limb-Pelvis Finite Element Model with 3D Active Muscles. Ann Biomed Eng 2018;46:86–96. https://doi.org/10.1007/s10439-017-1942-1.

[37] Stelletta J, Dumas R, Lafon Y. Modeling of the Thigh: A 3D Deformable Approach Considering Muscle Interactions. Biomech. Living Organs Hyperelastic Const. Laws Finite Elem. Model., 2017, p. 497–521. https://doi.org/10.1016/B978-0-12-804009-6.00023-7.

[38] Blemker SS, Pinsky PM, Delp SL. A 3D model of muscle reveals the cause of nonuniform strains in the biceps brachii. J Biomech Award 2005;38:657–65. https://doi.org/10.1016/j.jbiomech.2004.04.009.

[39] Siebert T, Till O, Stutzig N, Günther M, Blickhan R. Muscle force depends on the amount of transversal muscle loading. J Biomech 2014;47:1822–8. https://doi.org/10.1016/j.jbiomech.2014.03.029.

[40] Shu L, Yamamoto K, Yao J, Saraswat P, Liu Y, Mitsuishi M, et al. A subject-specific finite element musculoskeletal framework for mechanics analysis of a total knee replacement. J Biomech 2018;77:146–54. https://doi.org/10.1016/j.jbiomech.2018.07.008.

[41] Navacchia A, Hume DR, Rullkoetter PJ, Shelburne KB. A computationally efficient strategy to estimate muscle forces in a finite element musculoskeletal model of the lower limb. J Biomech 2019;84:94–102. https://doi.org/10.1016/j.jbiomech.2018.12.020.

[42] Liu X, Zhang M. Redistribution of knee stress using laterally wedged insole intervention: Finite element analysis of knee-ankle-foot complex. Clin Biomech 2013;28:61–7. https://doi.org/10.1016/j.clinbiomech.2012.10.004.

[43] Hume DR, Navacchia A, Ali AA, Shelburne KB. The interaction of muscle moment arm, knee laxity, and torque in a multi-scale musculoskeletal model of the lower limb. J Biomech 2018;76:173–80. https://doi.org/10.1016/j.jbiomech.2018.05.030.

[44] Tawhai M, Bischoff J, Einstein D, Erdemir A, Guess T, Reinbolt J. Multiscale modeling in computational biomechanics. IEEE Eng Med Biol Mag 2009;28:41–9. https://doi.org/10.1109/MEMB.2009.932489.

[45] Ezquerro F, Simón A, Prado M, Pérez A. Combination of finite element modeling and optimization for the study of lumbar spine biomechanics considering the 3D thorax-pelvis orientation. Med Eng Phys 2004;26:11–22. https://doi.org/10.1016/S1350-4533(03)00128-0.

[46] Halloran JP, Ackermann M, Erdemir A, van den Bogert AJ. Concurrent musculoskeletal dynamics and finite element analysis predicts altered gait patterns to reduce foot tissue loading. J Biomech 2010;43:2810–5. https://doi.org/10.1016/j.jbiomech.2010.05.036.

[47] Fitzpatrick CK, Baldwin MA, Clary CW, Maletsky LP, Rullkoetter PJ. Evaluating knee replacement mechanics during ADL with PID-controlled dynamic finite element analysis. Comput Methods Biomech Biomed Engin 2014;17:360–9. https://doi.org/10.1080/10255842.2012.684242.

[48] Geraldes DM, Modenese L, Phillips ATM. Consideration of multiple load cases is critical in modelling orthotropic bone adaptation in the femur. Biomech Model Mechanobiol 2016;15:1029–42. https://doi.org/10.1007/s10237-015-0740-7.

[49] Navacchia A, Rullkoetter PJ, Schütz P, List RB, Fitzpatrick CK, Shelburne KB. Subject-specific modeling of muscle force and knee contact in total knee arthroplasty. J Orthop Res 2016;34:1576–87. https://doi.org/10.1002/jor.23171.

[50] Shelburne KB, Torry MR, Pandy MG. Muscle, Ligament, and Joint-Contact Forces at the Knee during Walking. Med Sci Sport Exerc 2005;37:1948–56. https://doi.org/10.1249/01.mss.0000180404.86078.ff.

[51] Halonen KS, Dzialo CM, Mannisi M, Venäläinen MS, De Zee M, Andersen MS. Workflow assessing the effect of gait alterations on stresses in the medial tibial cartilage - Combined musculoskeletal modelling and finite element analysis. Sci Rep 2017;7:1–14. https://doi.org/10.1038/s41598-017-17228-x.

[52] Liukkonen MK, Mononen ME, Vartiainen P, Kaukinen P, Bragge T, Suomalainen JS, et al. Evaluation of the Effect of Bariatric Surgery-Induced Weight Loss on Knee Gait and Cartilage Degeneration. J Biomech Eng 2018;140. https://doi.org/10.1115/1.4038330.

[53] Esrafilian A, Stenroth L, Mononen ME, Tanska P, Avela J, Korhonen RK. EMG-Assisted Muscle Force Driven Finite Element Model of the Knee Joint with Fibril-Reinforced Poroelastic Cartilages and Menisci. Sci Rep 2020;10:1–16. https://doi.org/10.1038/s41598-020-59602-2.

[54] Kłodowski A, Mononen ME, Kulmala JP, Valkeapää A, Korhonen RK, Avela J, et al. Merge of motion analysis, multibody dynamics and finite element method for the subject-specific analysis of cartilage loading patterns during gait: differences between rotation and moment-driven models of human knee joint. Multibody Syst Dyn 2016;37:271–90. https://doi.org/10.1007/s11044-015-9470-y.

[55] Marouane H, Shirazi-Adl A, Adouni M. 3D active-passive response of human knee joint in gait is markedly altered when simulated as a planar 2D joint. Biomech Model Mechanobiol 2017;16:693–703. https://doi.org/10.1007/s10237-016-0846-6.

[56] Lloyd JE, Stavness I, Fels S. ArtiSynth: A Fast Interactive Biomechanical Modeling Toolkit Combining Multibody and Finite Element Simulation. Stud. Mechanobiol. Tissue Eng. Biomater., vol. 11, Springer; 2012, p. 355–94. https://doi.org/10.1007/8415_2012_126.

[57] Lloyd J, Roewer-Despres F, Stavness I. Muscle Path Wrapping on Arbitrary Surfaces. IEEE Trans Biomed Eng 2020:1–1. https://doi.org/10.1109/tbme.2020.3009922.

[58] Lloyd JE, Sánchez A, Widing E, Stavness I, Fels S, Niroomandi S, et al. New techniques for combined FEM-Multibody anatomical simulation. Lect. Notes Comput. Vis. Biomech., vol. 999, Springer Netherlands; 2019, p. 75–92. https://doi.org/10.1007/978-3-030-23073-9_6.

[59] Paley D. Principles of Deformity Correction. Springer Berlin Heidelberg; 2002. https://doi.org/10.1007/978-3-642-59373-4.

[60] Esenkaya I, Unay K, Akan K. Proximal tibial osteotomies for the medial compartment arthrosis of the knee: A historical journey. Strateg Trauma Limb Reconstr 2012;7:13–21. https://doi.org/10.1007/s11751-012-0131-x.

[61] Lee DC, Byun SJ. High Tibial Osteotomy. Knee Surg Relat Res 2012;24:61–9. https://doi.org/10.5792/ksrr.2012.24.2.61.

[62] McNamara I, Birmingham TB, Fowler PJ, Giffin JR. High tibial osteotomy: evolution of research and clinical applications—a Canadian experience. Knee Surgery, Sport Traumatol Arthrosc 2013;21:23–31.

[63] Song IH, Song EK, Seo HY, Lee KB, Yim JH, Seon JK. Patellofemoral alignment and anterior knee pain after closing- and opening-wedge valgus high tibial osteotomy. Arthrosc - J Arthrosc Relat Surg 2012;28:1087–93. https://doi.org/10.1016/j.arthro.2012.02.002.

[64] Coventry MB. Osteotomy about the Knee for Degenerative and Rheumatoid Arthritis : INDICATIONS , OPERATIVE TECHNIQUE , AND RESULTS Knee Arthritis. JournalsLwwCom 2010.

[65] Sun H, Zhou L, Li F, Duan J. Comparison between Closing-Wedge and Opening-Wedge High Tibial Osteotomy in Patients with Medial Knee Osteoarthritis: A Systematic Review and Meta-analysis. J Knee Surg 2017;30:158–65. https://doi.org/10.1055/s-0036-1584189.

[66] Wolcott M, Traub S, Efird C. High tibial osteotomies in the young active patient. Int Orthop 2010;34:161–6. https://doi.org/10.1007/s00264-009-0944-5.

[67] Sterett WI, Steadman JR, Huang MJ, Matheny LM, Briggs KK. Chondral Resurfacing and High Tibial Osteotomy in the Varus Knee. Am J Sports Med 2010;38:1420–4. https://doi.org/10.1177/0363546509360403.

[68] Saragaglia D, Mercier N, Colle PE. Computer-assisted osteotomies for genu varum deformity: Which osteotomy for which varus? Int Orthop 2010;34:185–90. https://doi.org/10.1007/s00264-009-0757-6.

[69] Bode G, von Heyden J, Pestka J, Schmal H, Salzmann G, Südkamp N, et al. Prospective 5-year survival rate data following open-wedge valgus high tibial osteotomy. Knee Surgery, Sport Traumatol Arthrosc 2015;23:1949–55. https://doi.org/10.1007/s00167-013-2762-y.

[70] Devgan A, Marya K, … ZK-MJ of, 2003 undefined. Medial opening wedge high tibial osteotomy for osteoarthritis of knee: long term results in 50 knees. ResearchgateNet n.d.

[71] Puddu G, Franco V. Femoral antivalgus opening wedge osteotomy. Oper Tech Sports Med 2000;8:56–60. https://doi.org/10.1016/S1060-1872(00)80026-X.

[72] Hinterwimmer S, Beitzel K, Paul J, Kirchhoff C, Sauerschnig M, Von Eisenhart-Rothe R, et al. Control of posterior tibial slope and patellar height in open-wedge valgus high tibial osteotomy. Am J Sports Med 2011;39:851–6. https://doi.org/10.1177/0363546510388929.

[73] Hopwood S, Khan W, Agarwal S. The biplanar open wedge high tibial osteotomy preserving the tibial tubercle. J Orthop Sci 2016;21:786–90. https://doi.org/10.1016/j.jos.2016.07.006.

[74] Nie Y, Ma J, Huang ZY, Xu B, Tang S, Shen B, et al. Upper partial fibulectomy improves knee biomechanics and function and decreases knee pain of osteoarthritis: A pilot and biomechanical study. J Biomech 2018;71:22–9. https://doi.org/10.1016/j.jbiomech.2017.12.004.

[75] Shimizu T, Fujioka F, Gomyo H, Isobe K, Takaoka K. Three-dimensional starch model for simulation of corrective osteotomy for a complex bone deformity: A case report. Foot Ankle Int 2003;24:364–7. https://doi.org/10.1177/107110070302400411.

[76] Victor J, Premanathan A. Virtual 3D planning and patient specific surgical guides for osteotomies around the knee: a feasibility and proof-of-concept study. Bone Joint J 2013;95 B:153–8. https://doi.org/10.1302/0301-620X.95B11.32950.

[77] Agarwala S, Sobti A, Naik S, Chaudhari S. Comparison of closing-wedge and opening-wedge high tibial osteotomies for medial compartment osteoarthritis of knee in Asian population: Mid-term follow-up. J Clin Orthop Trauma 2016;7:272–5. https://doi.org/10.1016/j.jcot.2016.06.012.

[78] Duivenvoorden T, Brouwer RW, Baan A, Bos PK, Reijman M, Bierma-Zeinstra SMA, et al. Comparison of closing-wedge and opening-wedge high tibial osteotomy for medial compartment osteoarthritis of the knee: A randomized controlled trial with a six-year follow-up. J Bone Jt Surg - Am Vol 2014;96:1425–32. https://doi.org/10.2106/JBJS.M.00786.

[79] Loia MC, Vanni S, Rosso F, Bonasia DE, Bruzzone M, Dettoni F, et al. High tibial osteotomy in varus knees: Indications and limits. Joints 2016;4:98–110. https://doi.org/10.11138/jts/2016.4.2.098.

[80] Noyes FR, Mayfield W, Barber-Westin SD, Albright JC, Heckmann TP. Opening wedge high tibial osteotomy: An operative technique and rehabilitation program to decrease complications and promote early union and function. Am J Sports Med 2006;34:1262–73. https://doi.org/10.1177/0363546505286144.

[81] Hernigou P, Medevielle D, Debeyre J, Goutallier D. Proximal tibial osteotomy for osteoarthritis with varus deformity. A ten to thirteen-year follow-up study. J Bone Jt Surg - Ser A 1987;69:332–54. https://doi.org/10.2106/00004623-198769030-00005.

[82] Dugdale TW, Noyes FR, Styer D. Preoperative Planning for High Tibial Osteotomy: The Effect of Lateral Tibiofemoral Separation and Tibiofemoral Length. Clin Orthop Relat Res 1992:248–64. https://doi.org/10.1053/j.oto.2006.09.007.

[83] Fujisawa Y, Masuhara K, Shiomi S. The Effect of High Tibial Osteotomy on Osteoarthritis of the Knee: An Arthroscopic Study of 54 Knee Joints. Orthop Clin North Am 1979;10:585–608. https://doi.org/10.1007/BF00266324.

[84] Hernigou P, Ovadia H, Goutallier D. Mathematical modelling of open-wedge tibial osteotomy and correction tables. Rev Chir Orthop Reparatrice Appar Mot 1992;78:258–63.

[85] d'Entremont AG, McCormack RG, Horlick SGD, Stone TB, Manzary MM, Wilson DR. Effect of opening-wedge high tibial osteotomy on the three-dimensional kinematics of the knee. Bone Joint J 2014;96-B:1214–21. https://doi.org/10.1302/0301-620X.96B9.32522.

[86] Insall JN, Joseph DM, Msika C. High tibial osteotomy for varus gonarthrosis. A long-term follow-up study. J Bone Joint Surg Am 1984;66:1040–8.

[87] DeMeo PJ, Johnson EM, Chiang PP, Flamm AM, Miller MC. Midterm Follow-up of Opening-Wedge High Tibial Osteotomy. Am J Sports Med 2010;38:2077–84. https://doi.org/10.1177/0363546510371371.

[88] Sprenger TR, Doerzbacher JF. Tibial osteotomy for the treatment of varus gonarthrosis. Survival and failure analysis to twenty-two years. J Bone Joint Surg Am 2003;85-A:469–74.

[89] Benzakour T, Hefti A, Lemseffer M, Ahmadi JD El, Bouyarmane H, Benzakour A. High tibial osteotomy for medial osteoarthritis of the knee: 15 years follow-up. Int Orthop 2010;34:209. https://doi.org/10.1007/S00264-009-0937-4.

[90] Mina C, Garrett WE, Pietrobon R, Glisson R, Higgins L. High Tibial Osteotomy for Unloading Osteochondral Defects in the Medial Compartment of the Knee. Am J Sports Med 2008;36:949–55. https://doi.org/10.1177/0363546508315471.

[91] Briem K, Ramsey DK, Newcomb W, Rudolph KS, Snyder-Mackler L. Effects of the Amount of Valgus Correction for Medial Compartment Knee Osteoarthritis on Clinical Outcome, Knee Kinetics and Muscle Co-Contraction after Opening Wedge High Tibial Osteotomy. J Orthop Res 2007;25:311. https://doi.org/10.1002/JOR.20326.

[92] Miniaci A, Ballmer FT, Ballmer PM, Jakob RP. Proximal Tibial Osteotomy. A New Fixation Device. Clin Orthop Relat Res 1989:250–9. https://doi.org/10.1097/00003086-198909000-00035.

[93] Martin R, Birmingham TB, Willits K, Litchfield R, Lebel ME, Giffin JR. Adverse event rates and classifications in medial opening wedge high tibial osteotomy. Am J Sports Med 2014;42:1118–26. https://doi.org/10.1177/0363546514525929.

[94] Seitz AM, Nelitz M, Ignatius A, Dürselen L. Release of the medial collateral ligament is

mandatory in medial open-wedge high tibial osteotomy. Knee Surgery, Sport Traumatol Arthrosc 2018. https://doi.org/10.1007/s00167-018-5167-0.

[95] Moher D, Liberati A, Tetzlaff J, Altman DG, Altman D, Antes G, et al. Preferred reporting items for systematic reviews and meta-analyses: The PRISMA statement. PLoS Med 2009;6. https://doi.org/10.1371/journal.pmed.1000097.

[96] Pape D, Duchow J, Rupp S, Seil R, Kohn D. Partial release of the superficial medial collateral ligament for open-wedge high tibial osteotomy. Knee Surgery, Sport Traumatol Arthrosc 2006;14:141–8. https://doi.org/10.1007/s00167-005-0649-2.

[97] Seo S-S, Kim C-W, Seo J-H, Kim D-H, Lee C-R. Does Superficial Medial Collateral Ligament Release in Open-Wedge High Tibial Osteotomy for Varus Osteoarthritic Knees Increase Valgus Laxity? Am J Sports Med 2016;44:908–15. https://doi.org/10.1177/0363546515624925.

[98] van Egmond N, Hannink G, Janssen D, Vrancken AC, Verdonschot N, van Kampen A. Relaxation of the MCL after an Open-Wedge High Tibial Osteotomy results in decreasing contact pressures of the knee over time. Knee Surgery, Sport Traumatol Arthrosc 2017;25:800–7. https://doi.org/10.1007/s00167-017-4438-5.

[99] Agneskirchner JD, Hurschler C, Wrann CD, Lobenhoffer P. The Effects of Valgus Medial Opening Wedge High Tibial Osteotomy on Articular Cartilage Pressure of the Knee: A Biomechanical Study. Arthrosc - J Arthrosc Relat Surg 2007;23:852–61. https://doi.org/10.1016/j.arthro.2007.05.018.

[100] Suero EM, Sabbagh Y, Westphal R, Hawi N, Citak M, Wahl FM, et al. Effect of medial opening wedge high tibial osteotomy on intraarticular knee and ankle contact pressures. J Orthop Res 2015;33:598–604. https://doi.org/10.1002/jor.22793.

[101] Martineau PA, Fening SD, Miniaci A. Anterior opening wedge high tibial osteotomy: the effect of increasing posterior tibial slope on ligament strain. Can J Surg 2010;53:261–7.

[102] Ozel O, Yucel B, Mutlu S, Orman O, Mutlu H. Changes in posterior tibial slope angle in patients undergoing open-wedge high tibial osteotomy for varus gonarthrosis. Knee Surgery, Sport Traumatol Arthrosc 2017;25:314–8. https://doi.org/10.1007/s00167-015-3571-2.

[103] Sterett W, Miller B, Joseph T, Rich V, Bain E. Posterior Tibial Slope After Medial Opening Wedge High Tibial Osteotomy of the Varus Degenerative Knee. J Knee Surg 2009;22:13–6. https://doi.org/10.1055/s-0030-1247720.

[104] Lee D-H, Han S-B, Oh K-J, Lee JS, Kwon J-H, Kim J-I, et al. The weight-bearing scanogram technique provides better coronal limb alignment than the navigation technique in open high tibial osteotomy. Knee 2014;21:451–5. https://doi.org/10.1016/j.knee.2012.09.003.

[105] Nerhus TK, Ekeland A, Solberg G, Sivertsen EA, Madsen JE, Heir S. Radiological

outcomes in a randomized trial comparing opening wedge and closing wedge techniques of high tibial osteotomy. Knee Surgery, Sport Traumatol Arthrosc 2017;25:910–7. https://doi.org/10.1007/s00167-015-3817-z.

[106] Elmali N, Esenkaya I, Can M, Karakaplan M. Monoplanar versus biplanar medial open-wedge proximal tibial osteotomy for varus gonarthrosis: A comparison of clinical and radiological outcomes. Knee Surgery, Sport Traumatol Arthrosc 2013;21:2689–95. https://doi.org/10.1007/s00167-012-2040-4.

[107] Birmingham TB, Giffin JR, Chesworth BM, Bryant DM, Litchfield RB, Willits K, et al. Medial opening wedge high tibial osteotomy: A prospective cohort study of gait, radiographic, and patient-reported outcomes. Arthritis Care Res 2009;61:648–57. https://doi.org/10.1002/art.24466.

[108] Chang J, Scallon G, Beckert M, Zavala J, Bollier M, Wolf B, et al. Comparing the accuracy of high tibial osteotomies between computer navigation and conventional methods. Comput Assist Surg 2017;22:1–8. https://doi.org/10.1080/24699322.2016.1271909.

[109] Na Y, Lee B, Hwang D, Choi E, Knee JS-T, 2018 undefined. Can osteoarthritic patients with mild varus deformity be indicated for high tibial osteotomy? Elsevier n.d.

[110] van Egmond N, van Grinsven S, van Loon CJM, Gaasbeek RD, van Kampen A. Better clinical results after closed- compared to open-wedge high tibial osteotomy in patients with medial knee osteoarthritis and varus leg alignment. Knee Surgery, Sport Traumatol Arthrosc 2016;24:34–41. https://doi.org/10.1007/s00167-014-3303-z.

[111] Nha K-W, Kim H-J, Ahn H-S, Lee D-H. Change in Posterior Tibial Slope After Open-Wedge and Closed-Wedge High Tibial Osteotomy. Am J Sports Med 2016;44:3006–13. https://doi.org/10.1177/0363546515626172.

[112] Yan J, Musahl V, Kay J, Khan M, Simunovic N, Ayeni OR. Outcome reporting following navigated high tibial osteotomy of the knee: a systematic review. Knee Surgery, Sport Traumatol Arthrosc 2016;24:3529–55. https://doi.org/10.1007/s00167-016-4327-3.

[113] Wu L, Lin J, Jin Z, Cai X, Gao W. Comparison of clinical and radiological outcomes between opening-wedge and closing-wedge high tibial osteotomy: A comprehensive meta-analysis 2017. https://doi.org/10.1371/journal.pone.0171700.

[114] Park H, Kim HW, Kam JH, Lee DH. Open Wedge High Tibial Osteotomy with Distal Tubercle Osteotomy Lessens Change in Patellar Position. Biomed Res Int 2017;2017. https://doi.org/10.1155/2017/4636809.

[115] Hanada M, Takahashi M, Koyama H, Matsuyama Y. Comparison of the change in patellar height between opening and closed wedge high tibial osteotomy: Measurement with a new method. Eur J Orthop Surg Traumatol 2014;24:567–70. https://doi.org/10.1007/s00590-013-1226-x.

[116] Longino PD, Birmingham TB, Schultz WJ, Moyer RF, Giffin JR. Combined tibial tubercle

osteotomy with medial opening wedge high tibial osteotomy minimizes changes in patellar height: A prospective cohort study with historical controls. Am J Sports Med 2013;41:2849–57. https://doi.org/10.1177/0363546513505077.

[117] Tanaka T, Matsushita T, Miyaji N, Ibaraki K, Nishida K, Oka S, et al. Deterioration of patellofemoral cartilage status after medial open-wedge high tibial osteotomy. Knee Surgery, Sport Traumatol Arthrosc 2019;27:1347–54. https://doi.org/10.1007/s00167-018-5128-7.

[118] Fan JCH. Open wedge high tibial osteotomy: Cause of patellar descent. J Orthop Surg Res 2012;7. https://doi.org/10.1186/1749-799X-7-3.

[119] Bito H, Takeuchi R, Kumagai K, Aratake M, Saito I, Hayashi R, et al. Opening wedge high tibial osteotomy affects both the lateral patellar tilt and patellar height. Knee Surgery, Sport Traumatol Arthrosc 2010;18:955–60. https://doi.org/10.1007/s00167-010-1077-5.

[120] Lee YS, Lee SB, Oh WS, Kwon YE, Lee BK. Changes in patellofemoral alignment do not cause clinical impact after open-wedge high tibial osteotomy. Knee Surgery, Sport Traumatol Arthrosc 2016;24:129–33. https://doi.org/10.1007/s00167-014-3349-y.

[121] Birmingham TB, Giffin JR, Chesworth BM, Bryant DM, Litchfield RB, Willits K, et al. Medial opening wedge high tibial osteotomy: A prospective cohort study of gait, radiographic, and patient-reported outcomes. Arthritis Care Res 2009;61:648–57. https://doi.org/10.1002/art.24466.

[122] Peña E, Calvo B, Martínez MA, Palanca D, Doblaré M. Finite element analysis of the effect of meniscal tears and meniscectomies on human knee biomechanics. Clin Biomech 2005;20:498–507. https://doi.org/10.1016/j.clinbiomech.2005.01.009.

[123] Donahue TLH, Hull ML, Rashid MM, Jacobs CR. A finite element model of the human knee joint for the study of tibio-femoral contact. J Biomech Eng 2002;124:273–80. https://doi.org/10.1115/1.1470171.

[124] Ogden S, Mukherjee DP, Keating ME, Ogden AL, Albright JA, McCall RE. Changes in Load Distribution in the Knee After Opening-Wedge or Closing-Wedge High Tibial Osteotomy. J Arthroplasty 2009;24:101–9. https://doi.org/10.1016/j.arth.2008.01.303.

[125] Zheng K, Scholes CJ, Chen J, Parker D, Li Q. Multiobjective optimization of cartilage stress for non-invasive, patient-specific recommendations of high tibial osteotomy correction angle – a novel method to investigate alignment correction. Med Eng Phys 2017;42:26–34. https://doi.org/10.1016/J.MEDENGPHY.2016.11.013.

[126] Trad Z, Barkaoui A, Chafra M, Tavares JMR. Finite element analysis of the effect of high tibial osteotomy correction angle on articular cartilage loading. Proc Inst Mech Eng Part H J Eng Med 2018;232:553–64. https://doi.org/10.1177/0954411918770706.

[127] Martay JL, Palmer AJ, Bangerter NK, Clare S, Monk AP, Brown CP, et al. A preliminary modeling investigation into the safe correction zone for high tibial osteotomy. Knee

2018;25:286–95. https://doi.org/10.1016/j.knee.2017.12.006.

[128] Purevsuren T, Khuyagbaatar B, Kim K, Kim YH. Effects of medial collateral ligament release, limb correction, and soft tissue laxity on knee joint contact force distribution after medial opening wedge high tibial osteotomy: a computational study. Comput Methods Biomech Biomed Engin 2019;22:243–50. https://doi.org/10.1080/10255842.2018.1549658.

[129] Kuriyama S, Watanabe M, Nakamura S, Nishitani K, Sekiguchi K, Tanaka Y, et al. Classical target coronal alignment in high tibial osteotomy demonstrates validity in terms of knee kinematics and kinetics in a computer model. Knee Surgery, Sport Traumatol Arthrosc 2019. https://doi.org/10.1007/s00167-019-05575-3.

[130] Noyes FR, Goebel SX, West J. Opening wedge tibial osteotomy: The 3-triangle method to correct axial alignment and tibial slope. Am J Sports Med 2005;33:378–87. https://doi.org/10.1177/0363546504269034.

[131] Brazier J, Migaud H, Gougeon F, Cotten A, Fontaine C, Duquennoy A. [Evaluation of methods for radiographic measurement of the tibial slope. A study of 83 healthy knees]. Rev Chir Orthop Reparatrice Appar Mot 1996;82:195–200.

[132] Giffin JR, Vogrin TM, Zantop T, Woo SL-Y, Harner CD. Effects of Increasing Tibial Slope on the Biomechanics of the Knee. Am J Sports Med 2004;32:376–82. https://doi.org/10.1177/0363546503258880.

[133] Lee YS, Park SJ, Shin VI, Lee JH, Kim YH, Song EK. Achievement of targeted posterior slope in the medial opening wedge high tibial osteotomy: A mathematical approach. Ann. Biomed. Eng., vol. 38, Springer; 2010, p. 583–93. https://doi.org/10.1007/s10439-009-9860-5.

[134] Sariali E, Catonne Y. Modification of tibial slope after medial opening wedge high tibial osteotomy: Clinical study and mathematical modelling. Knee Surgery, Sport Traumatol Arthrosc 2009;17:1172–7. https://doi.org/10.1007/s00167-008-0717-5.

[135] Nha K-W, Kim H-J, Ahn H-S, Lee D-H. Change in Posterior Tibial Slope After Open-Wedge and Closed-Wedge High Tibial Osteotomy. Am J Sports Med 2016;44:3006–13. https://doi.org/10.1177/0363546515626172.

[136] Leardini A, Benedetti MG, Berti L, Bettinelli D, Nativo R, Giannini S. Rear-foot, mid-foot and fore-foot motion during the stance phase of gait. Gait Posture 2007;25:453–62. https://doi.org/10.1016/j.gaitpost.2006.05.017.

[137] Leardini A, Sawacha Z, Paolini G, Ingrosso S, Nativo R, Benedetti MG. A new anatomically based protocol for gait analysis in children. Gait Posture 2007;26:560–71. https://doi.org/10.1016/j.gaitpost.2006.12.018.

[138] Grood ES, Suntay WJ. A joint coordinate system for the clinical description of three-dimensional motions: Application to the knee. J Biomech Eng 1983;105:136–44.

https://doi.org/10.1115/1.3138397.

[139] Powers CM, Chen YJ, Farrokhi S, Lee TQ. Role of peripatellar retinaculum in transmission of forces within the extensor mechanism. J Bone Jt Surg - Ser A 2006;88:2042–8. https://doi.org/10.2106/JBJS.E.00929.

[140] Blankevoort L, Huiskes R. Ligament-bone interaction in a three-dimensional model of the knee. J Biomech Eng 1991;113:263–9. https://doi.org/10.1115/1.2894883.

[141] Pandy MG, Sasaki K, Kim S. A three-dimensional musculoskeletal model of the human knee joint. Part 1: Theoretical construction. Comput Methods Biomech Biomed Engin 1997;1:87–108. https://doi.org/10.1080/01495739708936697.

[142] Xu H, Bloswick D, Merryweather A. An improved OpenSim gait model with multiple degrees of freedom knee joint and knee ligaments. Comput Methods Biomech Biomed Engin 2015;18:1217–24. https://doi.org/10.1080/10255842.2014.889689.

[143] Yanke A, Bell R, Lee A, Shewman EF, Wang V, Bach BR. Regional mechanical properties of human patellar tendon allografts. Knee Surgery, Sport Traumatol Arthrosc 2015;23:961–7. https://doi.org/10.1007/s00167-013-2768-5.

[144] Merican AM, Sanghavi S, Iranpour F, Amis AA. The structural properties of the lateral retinaculum and capsular complex of the knee. J Biomech 2009;42:2323–9. https://doi.org/10.1016/j.jbiomech.2009.06.049.

[145] LaPrade MD, Kallenbach SL, Aman ZS, Moatshe G, Storaci HW, Turnbull TL, et al. Biomechanical Evaluation of the Medial Stabilizers of the Patella. Am J Sports Med 2018;46:1575–82. https://doi.org/10.1177/0363546518758654.

[146] Zajac FE. Muscle and tendon: properties, models, scaling, and application to biomechanics and motor control. Crit Rev Biomed Eng 1989;17:359–411.

[147] Millard M, Uchida T, … AS-J of, 2013 undefined. Flexing computational muscle: modeling and simulation of musculotendon dynamics. AsmedigitalcollectionAsmeOrg n.d.

[148] Arnold EM, Ward SR, Lieber RL, Delp SL. A model of the lower limb for analysis of human movement. Ann Biomed Eng 2010;38:269–79. https://doi.org/10.1007/s10439-009-9852-5.

[149] Ward SR, Eng CM, Smallwood LH, Lieber RL. Are current measurements of lower extremity muscle architecture accurate? Clin Orthop Relat Res 2009;467:1074–82. https://doi.org/10.1007/s11999-008-0594-8.

[150] Race A, Amis AA. The mechanical properties of the two bundles of the human posterior cruciate ligament. J Biomech 1994;27:13–24. https://doi.org/10.1016/0021-9290(94)90028-0.

[151] Robinson JR, Bull AMJ, Amis AA. Structural properties of the medial collateral ligament

complex of the human knee. J Biomech 2005;38:1067–74. https://doi.org/10.1016/j.jbiomech.2004.05.034.

[152] Carbone V, van der Krogt MM, Koopman HFJM, Verdonschot N. Sensitivity of subject-specific models to Hill muscle-tendon model parameters in simulations of gait. J Biomech 2016;49:1953–60. https://doi.org/10.1016/j.jbiomech.2016.04.008.

[153] Johansson T, Meier P, Blickhan R. A Finite-Element Model for the mechanical analysis of Skeletal Muscles. J Theor Biol 2000;206:131–49. https://doi.org/10.1006/jtbi.2000.2109\rS0022-5193(00)92109-X [pii].

[154] Blemker SS, Pinsky PM, Delp SL. A 3D model of muscle reveals the causes of nonuniform strains in the biceps brachii. J Biomech 2005;38:657–65. https://doi.org/10.1016/j.jbiomech.2004.04.009.

[155] Affagard JS, Feissel P, Bensamoun SF. Identification of hyperelastic properties of passive thigh muscle under compression with an inverse method from a displacement field measurement. J Biomech 2015;48:4081–6. https://doi.org/10.1016/j.jbiomech.2015.10.007.

[156] Nesme M, Kry PG, Jeřábková L, Faure F. Preserving topology and elasticity for embedded deformable models, Association for Computing Machinery (ACM); 2009, p. 1. https://doi.org/10.1145/1576246.1531358.

[157] Nakayama H, Schröter S, Yamamoto C, Iseki T, Kanto R, Kurosaka K, et al. Large correction in opening wedge high tibial osteotomy with resultant joint-line obliquity induces excessive shear stress on the articular cartilage. Knee Surgery, Sport Traumatol Arthrosc 2018;26:1873–8. https://doi.org/10.1007/s00167-017-4680-x.

[158] Akamatsu Y, Ohno S, Kobayashi H, Kusayama Y, Kumagai K, Saito T. Coronal subluxation of the proximal tibia relative to the distal femur after opening wedge high tibial osteotomy. Knee 2017;24:70–5. https://doi.org/10.1016/j.knee.2016.09.009.

[159] Kim SJ, Koh YG, Chun YM, Kim YC, Park YS, Sung CH. Medial opening wedge high-tibial osteotomy using a kinematic navigation system versus a conventional method: A 1-year retrospective, comparative study. Knee Surgery, Sport Traumatol Arthrosc 2009;17:128–34. https://doi.org/10.1007/s00167-008-0630-y.

[160] Helito CP, Bonadio MB, Rozas JS, Wey JMP, Pereira CAM, Cardoso TP, et al. Biomechanical study of strength and stiffness of the knee anterolateral ligament. BMC Musculoskelet Disord 2016;17. https://doi.org/10.1186/s12891-016-1052-5.

[161] Tissakht M, Ahmed AM. Tensile stress-strain characteristics of the human meniscal material. J Biomech 1995;28:411–22. https://doi.org/10.1016/0021-9290(94)00081-E.

[162] Villegas DF, Maes JA, Magee SD, Donahue TLH. Failure properties and strain distribution analysis of meniscal attachments. J Biomech 2007;40:2655–62. https://doi.org/10.1016/j.jbiomech.2007.01.015.

[163] Dumas R, Cheze L, Moissenet F. Multibody optimisations: From kinematic constraints to knee contact forces and ligament forces. Springer Tracts Adv. Robot., vol. 124, Springer Verlag; 2019, p. 65–89. https://doi.org/10.1007/978-3-319-93870-7_4.

[164] Bagherifard A, Jabalameli M, Mirzaei A, Khodabandeh A, Abedi M, Yahyazadeh H. Retaining the medial collateral ligament in high tibial medial open-wedge osteotomy mostly results in post-operative intra-articular gap reduction. Knee Surgery, Sport Traumatol Arthrosc 2020;28:1388–93. https://doi.org/10.1007/s00167-019-05473-8.

[165] Weiss JA, Gardiner JC. Computational modeling of ligament mechanics. Crit Rev Biomed Eng 2001;29:303–71. https://doi.org/10.1615/CritRevBiomedEng.v29.i3.20.

[166] Park H, Kim HW, Kam JH, Lee DH. Open Wedge High Tibial Osteotomy with Distal Tubercle Osteotomy Lessens Change in Patellar Position. Biomed Res Int 2017;2017. https://doi.org/10.1155/2017/4636809.

[167] Fan JC. Open wedge high tibial osteotomy: cause of patellar descent. J Orthop Surg Res 2012;7:3. https://doi.org/10.1186/1749-799X-7-3.

[168] MacIntyre NJ, Hill NA, Fellows RA, Ellis RE, Wilson DR. Patellofemoral joint kinematics in individuals with and without patellofemoral pain syndrome. J Bone Jt Surg - Ser A 2006;88:2596–605. https://doi.org/10.2106/JBJS.E.00674.

[169] Adouni M, Shirazi-Adl A. Partitioning of knee joint internal forces in gait is dictated by the knee adduction angle and not by the knee adduction moment. J Biomech 2014;47:1696–703. https://doi.org/10.1016/j.jbiomech.2014.02.028.

[170] Dumas R, Wojtusch J. Estimation of the Body Segment Inertial Parameters for the Rigid Body Biomechanical Models Used in Motion Analysis. In: Müller B., Wolf S. (eds) Handbook of Human Motion. 2018:47–77.

[171] Wu G, Siegler S, Allard P, Kirtley C, Leardini A, Rosenbaum D, et al. ISB recommendation on definitions of joint coordinate system of various joints for the reporting of human joint motion - Part I: Ankle, hip, and spine. J Biomech 2002;35:543–8. https://doi.org/10.1016/S0021-9290(01)00222-6.

[172] Buford J, Ivey J, Malone JD, Patterson RM, Peare GL, Nguyen DK, et al. Muscle balance at the knee - Moment arms for the normal knee and the ACL-minus knee. IEEE Trans Rehabil Eng 1997;5:367–79. https://doi.org/10.1109/86.650292.

[173] Pandy MG. Moment arm of a muscle force. Exerc Sport Sci Rev 1999;27:79–118.

[174] Montefiori E, Modenese L, Di Marco R, Magni-Manzoni S, Malattia C, Petrarca M, et al. An image-based kinematic model of the tibiotalar and subtalar joints and its application to gait analysis in children with Juvenile Idiopathic Arthritis. J Biomech 2019;85:27–36. https://doi.org/10.1016/j.jbiomech.2018.12.041.

[175] Dzialo CM, Pedersen PH, Jensen KK, de Zee M, Andersen MS. Evaluation of predicted

patellofemoral joint kinematics with a moving-axis joint model. Med Eng Phys 2019;73:85–91. https://doi.org/10.1016/j.medengphy.2019.08.001.

[176] Delp SL, Loan JP, Hoy MG, Zajac FE, Topp EL, Rosen JM. An Interactive Graphics-Based Model of the Lower Extremity to Study Orthopaedic Surgical Procedures. IEEE Trans Biomed Eng 1990;37:757–67. https://doi.org/10.1109/10.102791.

[177] Sancisi N, Gasparutto X, Parenti-Castelli V, Dumas R. A multi-body optimization framework with a knee kinematic model including articular contacts and ligaments. Meccanica 2017;52:695–711. https://doi.org/10.1007/s11012-016-0532-x.

[178] Clément J, Dumas R, Hagemeister N, de Guise JA. Soft tissue artifact compensation in knee kinematics by multi-body optimization: Performance of subject-specific knee joint models. J Biomech 2015;48:3796–802. https://doi.org/10.1016/j.jbiomech.2015.09.040.

[179] Gasparutto X, Sancisi N, Jacquelin E, Parenti-Castelli V, Dumas R. Validation of a multi-body optimization with knee kinematic models including ligament constraints. J Biomech 2015;48:1141–6. https://doi.org/10.1016/j.jbiomech.2015.01.010.

[180] Dumas R, Chèze L, Verriest JP. Adjustments to McConville et al. and Young et al. body segment inertial parameters. J Biomech 2007;40:543–53. https://doi.org/10.1016/j.jbiomech.2006.02.013.

[181] Dumas R, Chèze L, Verriest JP. Corrigendum to "Adjustments to McConville et al. and Young et al. body segment inertial parameters" [J. Biomech. (2006) in press] (DOI:10.1016/j.jbiomech.2006.02.013). J Biomech 2007;40:1651–2. https://doi.org/10.1016/j.jbiomech.2006.07.016.

[182] McConville Jý Thomas JT. ANTHROPOMETRIC RELATIONSHIPS OF BODY AND CC BODY SEGMENT MOMENTS OF INERTIA. 1980.

[183] Young JW, Chandler RF, Ret CCS, Robinette KM, Zehner GF. Anthropometric aand Mass Distribution Characteristics of the Adult Female. 1983.

[184] Moissenet F, Chèze L, Dumas R. A 3D lower limb musculoskeletal model for simultaneous estimation of musculo-tendon, joint contact, ligament and bone forces during gait. J Biomech 2014;47:50–8. https://doi.org/10.1016/j.jbiomech.2013.10.015.

[185] Modenese L, Renault JB. Automatic generation of personalised skeletal models of the lower limb from three-dimensional bone geometries. J Biomech 2021;116:110186. https://doi.org/10.1016/j.jbiomech.2020.110186.

[186] Rajendran K. Mechanism of locking at the knee joint. J Anat 1985;143:189–94.